SYNTHESIS AND CHARACTERIZATION OF NANO-STRUCTURE METAL OXIDES AND PEROXIDES PREPARED BY LASER ABLATION IN LIQUIDS

BY

QASEM AHMED QASEM DRMOSH

A Thesis Presented to the

DEANSHIP OF GRADUATE STUDIES

KING FAHD UNIVERSITY OF PETROLEUM & MINERALS

DHAHRAN, SAUDI ARABIA

In Partial Fulfillment of the
Requirements for the Degree of
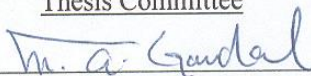
MASTER OF SCIENCE

In

PHYSICS

JUNE, 2010

KING FAHD UNIVERSITY OF PETROLEUM & MINERALS
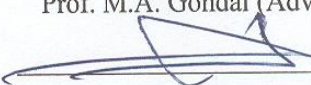## DHAHRAN 31261, SAUDI ARABIA

DEANSHIP OF GRADUATE STUDIES

This thesis, written by **QASEM AHMED QASEM DRMOSH** under the direction of his thesis advisor and approved by his thesis committee, has been presented to and accepted by the Dean of Graduate Studies, in partial fulfillment of the requirements for the degree of **MASTER OF SCIENCE IN PHYSICS**.
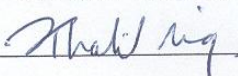
Thesis Committee
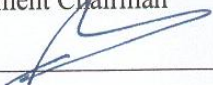
Prof. M.A. Gondal (Advisor)

Dr. Z.H. Yamani (Member)

Prof. K.A. Ziq (Member)

Dr. Abdul-Aziz Al-Jalal
Department Chairman

Dr. Salam Adel Zummo
Dean of Graduate Studies

27/3/10

[Date]

DEDICATED

To my loving parents who give me a wonderful life
and education

To those who are the secrets of my happiness and
joy, my darling kids

ACKNOWLEDGMENT

First, and foremost, all praise and thanks are due to Almighty Allah (S.W.T.) for blessing me good health, courage and patience to carry out this research.

I sincerely and deeply acknowledge with unrestrained appreciation my thesis advisor Prof. Dr. Mohammed Ashraf Gondal for giving me the time and for keeping me focused on my research. I cannot thank him enough for all his patience, encouragement, guidance, support, assistance and constructive feedback. My deepest personal regards are due for him forever.

My deep appreciation goes to my thesis committee members Dr. Zain Yamani, Director of the Center of Excellence in Nanotechnology (CENT), for his constant support. I am most indebted to him for his encouragement, cooperation, comments and constructive criticism and to Prof. Dr. Khalil Ziq for his attention, and keeping the facilities in his laboratory open to me.

I wish to thank the Physics Department, and the chairman Dr. Abdul-Aziz Al-Jalal for extending all the facilities and support to conduct this research work.

I owe a debt of gratitude to my dear parents, the gift of Allah to me. They have always been there for me in my good and difficult times. They have supported me in everything that I have endeavored. Their wisdom and insight have made me into a better person. Words fall short in conveying my gratitude towards them. May Allah (S.W.T.) give them good health and give me ample opportunity to be of service to them

TABLES OF CONTENTS

LIST OF TABLES

LIST OF FIGURES

THESIS ABSTRACT

NAME   QASEM AHMED QASEM DRMOSH

TITLE   SYNTHESIS AND CHARACTERIZATION OF NANO-STRUCTURE METAL OXIDES AND PEROXIDES PREPARED BY LASER ABLATION IN LIQUIDS.

MAJOR FIELD   PHYSICS.

DATE OF DEGREE   June 2010.

Pulsed laser ablation technique was applied for synthesize of ZnO, ZnO_2 and SnO_2 nanostructure using metallic target in different liquids. For this purpose, a laser emitting pulsed UV radiations generated by the third harmonic of Nd:YAG (λ= 355 nm) was applied. For the synthesis of ZnO nanoparticles (NPs), a high-purity metallic plate of Zn was fixed at the bottom of a glass cell in the presence of deionized water and was irradiated at different laser energies (80- 100- 120) mJ per pulse. The average sizes and lattice parameters of ZnO produced by this method were estimated by X-ray diffraction (XRD). The morphology of ZnO was studied by scanning electron microscopy (SEM) which illustrated the change in shape of synthesized structure from nanowires at low energy to spherical at high laser energy. The optical absorbance of the ZnO nanoparticles showed an absorption peak at 350 nm (3.37 eV) which is blue shifted relative to the bulk absorption (at 380 nm). This confirms the property nanostructure of ZnO. The photoluminescence (PL) spectra of ZnO nanoparticles showed two peaks: the first is a strong peak centered at 375 nm which is due to the recombination of electron

from valence band with hole in the conduction band. The second PL peak centering at violet luminescence around 420 nm is due to zinc defects.

ZnO nanoparticles were also produced by ablation of zinc target in the presence of deionized water mixed with two types of surfactants: cetyltrimethyl ammonium bromide (CTAB) and octaethylene glycol monododecyl (OGM). The results showed that the average grain sizes decreased from 38 nm in the case of deionized water to 27 nm and 19 nm in CTAB and OGM respectively. The PL emission in CTAB and OGM showed two peaks: the sharp UV emission at 380 nm and a broad visible peak ranging from 450 nm to 600 nm.

Zinc peroxide (ZnO_2) nanoparticles having grain size less than 5 nm were also synthesized using pulsed laser ablation in aqueous solution in the presence of different surfactants and solid zinc target in 3 % hydrogen peroxide H_2O_2 for the first time. The effect of surfactants on the optical and structure of ZnO_2 was studied by applying different spectroscopic techniques. The presence of the cubic phase of zinc peroxide in all samples was confirmed with XRD, and the grain sizes were 4.7 nm, 3.7 nm, 3.3 nm and 2.8 nm in pure H_2O_2; and H_2O_2 mixed with SDS, CTAB and OGM respectively. For optical characterization, FTIR transmittance spectra of ZnO_2 nanoparticles prepared with and without surfactants showed characteristic peaks of ZnO_2 absorption at 435-445 cm^{-1}. FTIR spectrum also revealed that the adsorbed surfactants on zinc peroxide disappeared in case of CTAB and OGM while it appears in case of SDS. Both FTIR and UV-Vis

spectra showed a red shift in the presence of SDS and blue shift in presence of CTAB and OGM.

The effect of post annealing temperature on dry ZnO_2 nanoparticles prepared by PLA technique of solid zinc target in 3% H_2O_2 was studied by variation of the annealing temperatures from 100 to 600 ℃ for 8 hours under 1 atmospheric pressure. The XRD showed the phase transition from ZnO_2 to ZnO at 200 ℃. Based on XRD data, both the average grain size and lattice parameters of ZnO increased by post annealing of ZnO_2 higher than 200 ℃. In contrast, the band gap of ZnO nanoparticles decreased when the annealing temperature increased. The average sizes were 5, 6, 9, 15 and 19 nm at 200, 300, 400, 500 and 600 ℃ respectively. The PL emission spectra for ZnO showed strong UV emission peaks in all samples. In addition, the UV emission peaks were shifted to longer wavelength (red shifting) as the annealing temperature increase from 200 to 600 ℃. From the above findings, we concluded that the grain size, lattice parameters, PL and band gap were size dependent as predicted by theoretical studies.

Tin dioxide (SnO_2) nanoparticles having size of approximately 3 nm were produced by irradiating a high purity Sn metal using high power Nd:YAG laser in deionized water. Formation of nano crystallites of SnO_2 was confirmed by XRD study. The UV–visible absorption showed a blue shift in the absorption edge which indicates the quantum confinement property of nanoparticles. The band gap of the prepared sample was 4.4 eV compared to 3.7 eV in the bulk. FTIR transmittance spectrum of SnO_2 nanoparticles showed characteristic Sn-O absorption at 400-700 cm^{-1}. The fitting of

peaks from PL spectra showed three emission peaks centered at 391, 427 and 475 nm respectively.

ملخص الرسالة

الاســـــــم : **قاسم أحمد قاسم درموش.**

عنوان الرسالة : **إنتاج وفحص اكاسيد وفوق اكاسيد معادن نانوية البنية بواسطة الإستئصال الليزري في السوائل.**

التخصص : **فيزياء.**

تاريخ التخرج : **يونيو 2010 م.**

تهدف هذة الدراسة الى إنتاج وفحص مواد نانوية البنية من أكسيد وفوق أكسيد الزنك وثنائي اكسيد القصدير بواسطة الإستئصال الليزري في السوائل وذلك بإرسال نبضات ليزرية من الأشعة فوق البنفسجية لليزر النادميوم ياج والذي يعمل عند الطول الموجي 355 نانو متر الى سطح معادن عالية النقاوة. لغرض انتاج اكسيد زنك نانوي البنية تم وضع عينة صلبة ونقية من معدن الزنك داخل انبوبة زجاجية تحتوي على ماء مقطربعد ذلك تم تشعيعها بشعاع ليزري لمدة 40 دقيقة و لغرض دراسة تأثير طاقة الليزر على خصائص المواد المنتجة تم تغيير طاقة نبضات الليزر كما يلي: (40-80-100) مللي جول/ نبضة بعد ذلك تم فحص العينات المنتجة عند هذة الطاقات بإستخدام عدة أجهزة حيث تم إستخدام جهاز حيود الأشعة السينية (XRD) لدراسة حجم حبيبات العينات المنتجة وابعاد خلايا الوحدة المرافقة لها ولقد اظهر أن كلاًّ من حجم الحبيبات وأبعاد خلية الوحدة لم يتغير بتغير طاقة الليزر أما جهاز الماسح الالكتروني(SEM) فقد أظهر جسيمات نانوية مختلفة الشكل حيث تغير شكل الحبيبات من اسلاك نانوية عند الطاقات الواطئة الى جسيمات كروية عند الطاقات العالية. جهاز مطياف الالكترون الضوئي (XPS) تم استخدامة لدراسة مكونات الحبيبات المنتجة والذي بين وجود مركب اكسيد الزنك مع وجود زيادة في نسبة الزنك داخل المركب. أما طيف اللمعان الضوئي فقد أظهر وجود قمتين بارزتين الأولى تقع في منطقة الأشعة فوق البفسجية والتي فسرت على أنها ناتجة من إعادة إلتحام الأكترونات القادمة من منطقة التوصيل مع فجوات منطقة التكافؤ اما القمة الثانية والأضعف مقارنة مع القمة الاولى فقد وجدت في المنطقة البفسجية وفسرت على انها بسبب وجود ذرات الزنك الزائدة في المركب.

xvii

ولغرض دراسة تاثير طبيعة السائل الموجود تم إضافة مواد خافضة للشد السطحي (Surfactants) الى الماء المقطر وتم إرسال النبضات الليزرية لمدة 40 دقيقة ولقد أظهرت نتائج جهاز حيود الأشعة السينية ان جميع المركبات الناتجة هي اوكسيد زنك وان حجم الحبيبات قد تغير من 38 نانو متر في حالة الماء المقطر فقط الى 29 و 17 نانو متر عند استخدام مادتي OGM, CTAB على التوالي. اما طيف اللمعان الضوئي فقد اوضح إختفاء قمة الإنبعاث في منطقة البنفسجية وظهور طيف واسع من الضوء المرئي والذي يمتد من المنطقة الصفراء حتى المنطقة الخضراء.

تم في هذة الدراسة ايضاً ولإول مرة إنتاج مادة بيرواكسيد الزنك بإستخدام طريقة الأستئصال الليزري في سائل يحتوي على 3 % من فوق اكسيد الهيدروجين وبحجم صغير جدا يصل الى 4 نانو متر كما تم ايضاً انتاج هذة المادة ايضا في حالة وجود مواد خافضة للتوتر السطحي CTAB, OGM, SDS . بين جهاز إنحراف الأشعة السينية وجود مركب بيرواكسيد الزنك في جميع العينات المحضرة كما بين ان حجم الحبيبات قد تناقص من 4.7 في حالة الماء المقطر الى 3.7 و 3.3 و 2.8 نانو متر عند استخدام مواد OGM, CTAB, SDS على التوالي. بين كلاً من جهار الإمتصاص الضوئي وجهاز نفاذ الأشعة تحت الحمراء وجود إزاحة في الأطياف نحو الأطوال الموجية الأقل والذي يفسر غالبا على إنة بسبب خاصية النقاط الكمية.

كما ان جهازطيف نفاذ الأشعة تحت الحمراء قد وضح وجود كميات قليلة جدا من المواد الخافضة للشد السطحي مترسبة فوق المادة النانوية المنتجة في حالة استخدام مادتي OGM , CTAB إلا إن هذا الترسب كان كبيراً وواضحاً في حال إستخدام مادة SDS.

هدفت هذة الدراسة ايضا الى التعرف على مدى تأثير درجة الحرارة على مادة بيرواكسيد الزنك المنتجة بإستخدام الإستصال الليزري حيث تم وضع 5 عينات من المادة في فرن كهربائي لمدة 8 ساعات وتم تغيير درجات الحرارة من 100 درجة مئوية الى 600 درجة مئوية. ولقد أظهرت النتائج ان مادة بيرواكسيد الزنك تحولت الى مادة اكسيد الزنك عند درجة حرارة 200 درجة مئوية من جهة اخرى وجد إنة بزيادة الحرارة من 200 الى 600 درجة مئوية فإن بعض الخصائص الفيزيائية مثل ابعاد خلية الوحدة وطاقة الفجوة وحجم الحبيبات والخصائص الضوئية تتغير

بتغير درجات الحرارة المطبقة على المادة فحجم الحبيبة مثلا تغير من 5 نانو متر الى 6, 9, 15, 19 نانو متر عند إستخدام درجات الحرارة 200, 300, 400, 500, 600 درجة مئوية على التوالي, اما قمم الانبعاث الضوئي فقد أزيحت بإتجاة الأطوال الموجية الأكبر بزيادة درجة الحرارة ولقد خلصنا الى ان سبب التغير في كل هذة الخواص الفيزيائية يعود الى التغير في ابعاد الحبيبة عندما تكون هذة الحبيبة في أبعاد النانو متر.

هدفت هذة الدراسة ايضا ○َ الى إنتاج ثنائي اكسيد القصدير بإستخدام نبضات عالية الطاقة 190 مللي جول /نبضة من ليزر النادميوم ياج على معدن القصدير النقي المغموس داخل طبقة رقيقة من الماء ولقد أوضحت نتائج جهاز إنحراف الاشعة السينية (XRD) ان متوسط حجم الحبيبات المنتجة هو 3 نانو متر كما درست بقية الخصائص الضوئية بإستخدام اللمعان الضوئي (PL) وجهاز نفاذ الاشعة تحت الحمراء(FTIR).

CHAPTER 1

INTRODUCTION

1.1. LASER ABLATION PROCESS OVERVIEW

Laser is an acronym for "Light Amplification by Stimulated Emission of Radiation". Laser has proven to be an effective tool in numerous applications. Basically, a typical laser consists of a gain medium (gas, liquid, solid) inside an optical cavity, with a source to supply energy to the gain medium. In its simplest form, the cavity consists of two mirrors arranged such that light bounces back and forth, each time passing through the gain medium. Pumping is the process of supplying the energy required for the amplification. The energy is typically supplied as an electrical current or as light by a flash lamp or another laser. The output of a laser may be a continuous constant-amplitude output (known as continuous wave or CW), or pulsed, by using techniques like Q-switching, mode locking, or gain switching. Applications take advantage of the unique properties of laser light which include:

- Monochromatic: laser light consists of essentially one wavelength; this property is because the emission line width is much narrower than normal light.

- Coherent: the emitted light waves are in phase in time (temporal coherent) and space (special coherence).

- Highly directional: laser light is emitted as a narrow beam and in a specific direction. This property is referred to as directionality.

- Huge peak power.

The wide ranges of laser properties are applied in different technologies such as spectroscopy, communication, data storage, material processing, welding, induced oxidation, and ablation.

The term "Laser ablation" refers to the surface process that is applied for removal of material from a solid surface by irradiating the surfaces with high energy laser radiation. Laser ablation process is widely used for different applications such as: thin film deposition, microelectronic device, surface cleaning, nanomaterials fabrication and elemental analysis using laser induced breakdown spectrometry [1-4]. The basic idea of laser ablation is summarized in the following section.

When the laser pulse energy interacts with a solid target, it is partially reflected back by the surface of the target. This partial reflection depends on the wavelength of incident laser radiations and the target material. The remaining laser energy is absorbed by the target and heats its surface. The surface temperature rises sharply. Due to the sudden rise (in nano second) in surface temperature, melting, vaporization and ionization of ablated material takes place which leads to plasma generation. In addition, this sudden rise in temperature creates a shockwave which propagates into the solid material. The shock wave due to incoming laser radiation is responsible for generation of nanoparticles [5]. The amount of the removed (ablated) material depends on factors such

as: the laser energy, pulse duration, the wavelength of the laser, the solid target properties and the surrounding environment that could be liquid or gas [6,7].

The first report on laser ablation was presented, in 1962, by F. Breech and L. Cross [8]. They used ruby laser to vaporize and excite atoms from solid surface and the plasma emission was used to characterize the elemental composition of the sample. This work began the field of laser micro probe emission which was one of the first real applications of laser ablation. W.I. Linlor in the same year at the American Physics Society (APS) reported on laser plasma interaction [9]. The first laser ablation deposition started in 1965 by Smith and Turner [10]. They used a ruby laser to grow thin films with different materials. S.B. Ogale et al, synthesized metastable compound phase using pulsed laser induced at the interface between a liquid and a solid. They also observed the diamond phase from small particles synthesized by pulsed ruby laser irradiation of a graphite target immersed in benzene liquid [11,12]. In the 1990's, lasers with high repetition rate and short pulse durations were developed which made pulsed laser ablation deposition PALD a competitive tool for the growth of thin films and fabrication of nanostructured materials.

Laser ablation is a powerful technology for many applications such as: micromachining, direct sample chemical analysis, and nano structure materials fabrication either films or nanoparticles. Today, one of the most important aspects of laser ablation is the formation of nano structured materials. A detailed understanding of these materials is presented in the following sections.

1.2. NANOSCALE MATERIALS: INTRODUCTION

The term "nano" is derived from the Greek word nanos, which means dwarf or extremely small: in science, nano means a billionth (1×10^{-9}). Nanotechnology deals with different structures of matter that has sizes of the order of 10^{-9} of a meter. A nanometer is about ten times the size of small atoms, such as hydrogen and carbon. Nanomaterials are particles having a size ranging from 1 nm to 100 nm and thus represent a bridge between quantum mechanics and real world (micro and macro). To put a nanometer in context: DNA molecules are about 2.5 nm wide, a red blood cell is 7,000 nm, a human hair is 80,000 nm wide and an ant is millions of nanometers across.

Material in nano scale exhibit physical properties distinctively different from that of bulk due to the number of surface atoms. The surface area to volume ratio (S/V) and the specific surface area (m^2g^{-1}) of a system are inversely proportional to particle size and both increase drastically for particles less than 100 nm in diameter (see figure 1-1).
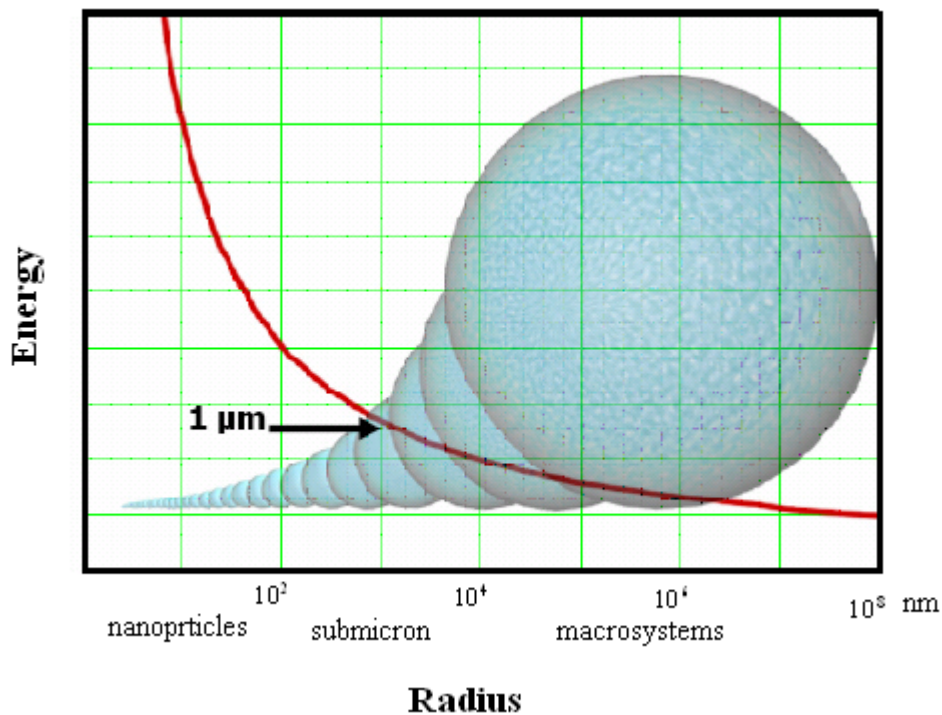
Figure 1-1 The dependence of surface free energy on radius of particles for constant volume.

The increase in surface area with decreasing particle size leads to changes in inters atomic spacing. Nanomaterials can be classified, according to the dimensionality, into one dimension (thin film), two dimension (nano wires, nano rods, nano tubes) and three dimension (nanoparticles).

The physical attributes (shape, size, surface properties) of nanomaterials change from those observed in the bulk. For example, the hardness of silicon nanoparticles (20-50) nm is four times greater than in bulk silicon [13-14]. Other properties such as optical, magnetic and electrical are also change with change in size.

Nanometer-size material like nano particles or nanowires can be produced by different methods. In general there are two approaches to fabricate nanomaterials: top-down and bottom-up. Nanoparticles etching of smaller structures from larger ones, laser ablation and milling are typical top-down methods. On the other hand, bottom-up approach refers to the build-up of a material from the bottom: atom-by-atom, molecule-by-molecule, or cluster-by-cluster. Sol-gel and crystal growth are examples for bottom-up approach where growth species, either atoms, ions or molecules, orderly assemble into desired crystal structure on the growth surface [15].

Historically Romans, in the fourth century A.D, were making glass containing nanometals. The Lycurgus cup present at the British Museum is an example. This cup is made from glass containing nanoparticles (silver and gold). The idea behind this cup is that when a light is placed inside the cup, the color of this cup changes from green to deep red. Gustay Mie (in 1908) was the first to provide an explanation of the dependence of the color of   glasses on metal size and its kind [16]. In 1959, Richard Feynman published "There's plenty of room at the bottom". He predicated to fabricate materials and devices at the atomic or molecular scale [17]. G.K. Binning and H. Roher in 1986 developed the scanning tunneling microscopic (STM). This technique and others like atomic force microscope (AFM), transmission electron microscope (TEM), and scanning electron microscope (SEM) plays a vital role for observation and characterization of nanostructures. In the last 18 years, several excellent studies of nanoscale materials have been carried out in fabrications, synthesis and applications of nano structured materials.

1.3. SYNTHESIS OF NANOMATERIALS

There are numerous of methods for production of nanomaterials. Essentially these falls into four categories: wet chemical process, mechanical process, gas phase synthesis and   vacuum deposition processes.

1.3.1. Wet chemical process

In this process, chemical reactions are applied to produce nanomaterials. The most common types of wet chemical method synthesis are: sol-gels, reduction method, electrochemical, hydrolysis and other precipitation processes.

Sol-gel processing is a wet chemical route for the synthesis of colloidal dispersions of inorganic and organic-inorganic hybrid materials, particularly oxides and oxide-based hybrids. This process involves the transition from very finely divided solid particles dispersed in a liquid (sol) to a gel (a dispersion of a liquid throughout a solid matrix). This method is often used to produce metal-oxide nanomaterials such as ZnO, TiO_2, SnO_2, Al_2O_3 and Fe_2O_3 [18-19]. The advantages of the process are perceived to be (i) low processing temperatures (ii) high purity of products (iii) low cost [20].

Nanosized particles (oxides, mixed oxide, semiconductors, etc) can also be fabricated using reverse micelles. This technique is based on a mixture of oil, water and surfactants. Surfactants (short for surface-active-agent) are organic compounds which stabilize mixtures of oil and water by reducing the surface tension at the interface

between the oil and water molecules or in other words increase the contact of two materials. Surfactants consist of two ends hydrophilic "heads" and hydrophobic "tails". According to the presence of formally charged groups in its head, it can be divided into four groups: nonionic (e.g. octaethylene glycol monododecyl ether OGM), anionic (e.g. sodium dodecyl sulfate SDS), cationic (cetyltrimethylammonium bromide CTAB), amphoteric (e.g. lauryl dimethylaminoacetic acid betaine LDA). When the concentration of surfactants is above a certain or critical concentration, it will aggregate with their hydrophobic or hydrophilic groups to form micelles which have the hydrophilic portion of the surfactant on the outside of the aggregate, or to form inverse micelles that have the hydrophobic portion on the outside.

The advantages of this technique are that a narrow particle size distribution can be obtained. and the particle size can be controlled.

1.3.2. Mechanical process

In this processes powders can be transferred mechanically into smaller and smaller particle sizes. Here grinding, milling, and mechanical alloying techniques are applied.

Ball milling technique is a good example of mechanical process. It is used to break bulk materials down to small size. Materials in the form of powders are crushed mechanically in rotating drums by hard steel or tungsten carbide balls. This repeated deformation can cause large reductions in grain size via the formation and organization of grain boundaries within the powder particles. Oxidation and other unwanted reactions

can be prevented by controlling the atmospheric conditions. ZnO and SnO_2 can be produced by means of this method [21-22].

1.3.3. Vacuum deposition processes

Physical vapor deposition (PVD), chemical vapor deposition (CVD) and spray coating are examples of the vacuum deposition processes. PVD processes are atomistic deposition processes in which material is vaporized usually from a solid source in the form of atoms or molecules, transported in the form of a vapor through a vacuum or low pressure environment to the substrate where it condenses. The thickness of the deposits can vary from a few nanometers to thousands of nanometers. PVD can be divided into two groups: evaporation and sputtering. In evaporation, the system consists of an evaporation source that vaporizes the desired material while a substrate is located at an appropriate distance facing the evaporation source. Both the source and the substrate are located in a vacuum chamber. To make a uniform film the substrate can be rotated during deposition. The substrate temperature, the desired vapor pressure, the source temperature and the flux of the gas play an important role for the features of the film growth [23]. In sputtering, atoms or molecules are dislodged from solid target through impact of gaseous ions (plasma). In general, the sputtering technique can have two modes: direct current DC and radio frequency RF. Sputtering in DC mode consists of a vacuum chamber, an anode (substrate), and a cathode (a metal target). In order to make sputtering happen, the system has to be in vacuum, then refilled with low-pressure inert gas, usually argon. When the potential between the anode and cathode exceeds a certain

value, the glow discharge occurs and the inert gas becomes ionized. The glow discharge plasma consists of different ionized gas species, which undergo various recombination processes. Under the applied electric field the ionized species accelerate. The positive ions then bombard the negatively charged target and kick some atoms off the target atoms upon collision. Some sputtered atoms deposit onto the substrate to form a layer of film. ZnO thin films can be produced by different modes of sputtering using DC & RF technique [24].

Chemical Vapor Deposition (CVD) is a chemical reaction which transforms gaseous molecules into a solid material in the form of thin film or powder on a substrate. Compared PVD, CVD has the advantage that it can be used in a continuous process for depositing, narrow size distributions, homogeneous coatings on large areas at faster deposition rates [25].

1.3.4. Gas phase synthesis

Gas phase synthesis process includes electro-explosion, laser ablation, and plasma synthesis techniques. The basic idea of electro explosion technique can be summarized as following: When a short (microsecond) high-current, high voltage electric power impulse is applied to a high purity metal wire inside a vacuum chamber filled with gas such as oxygen or argon, it causes the conducting wire to explode. The disadvantages of this method are: the complex design, high vacuum environment and high power consumption. P. Sen and coworkers used a novel process to produce metal nanoparticles

under water using two electrodes (one in the form of wire and another in the form of plate). In their work, 36 V DC was applied between two electrodes. When the wire was brought into a sudden contact with the plate, it exploded into nanoscale particles [26].

Pulsed laser ablation (PLA) is a surface process that is used to remove   materials from a solid surface by irradiating the surfaces with intense laser beam. Laser ablation has many applications. Synthesis of nano structure materials is one of these applications.

1.4. SYNTHESIS OF NANOSCALE MATERIALS BY PULESD LASE ABLATION

Basically, there are two popular methods to prepare nanostructured materials based on PLA. One is pulsed laser ablation deposition PLAD for synthesis of thin films either in vacuum or in the presence of gas. The second is pulsed laser ablation to fabricate nanoparticles in liquids.

1.4.1. Pulsed laser ablation deposition (PLAD)

In PLAD technique, a high power pulsed laser beam is focused onto a target inside a vacuum chamber (figure1-2).
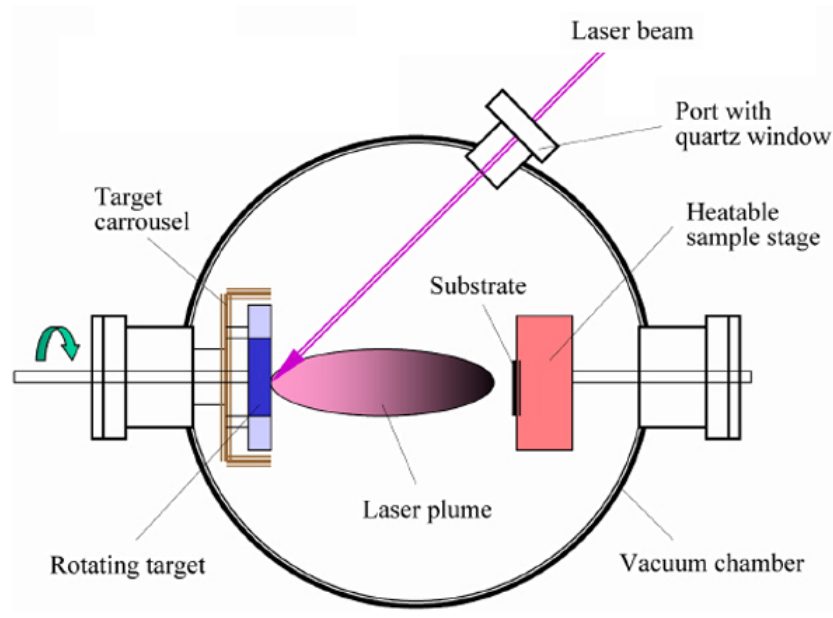
Figure 1-2. Set up for synthesis of thin films by PLAD in vacuum.

During the incident pulse of the laser, photons of laser can couple with vibration and electronic modes of the target material leading to raise in the electron temperature. Due to sudden rise (in nano seconds) in surface temperature, melting, vaporization and ionization of ablated material takes place which leads to plasma (generation) and (expansion). We called this "laser induced plasma". Then plasma plume is ejected (or transformation) from the surface of the target towards the substrate due to Coulomb repulsion and recoil effect. Finally, the plasma plume that contain species interact with the background gas and condense onto the substrate to make thin film. Figure (1-3) depicts the three steps of plasma plume (generation, expansion and transformation) to fabricate thin film [27-28].
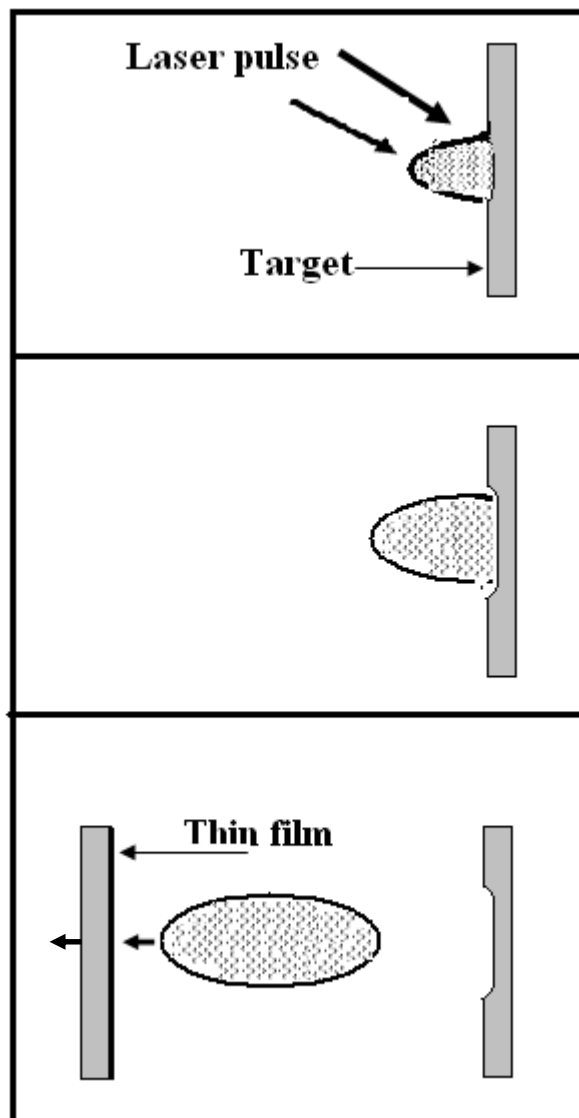
Figure 1-3. The schematic illustration of the plasma plume to fabricate thin films.

PLAD method has advantages over other methods such as chemical vapor deposition (CVD), physical vapor deposition (PVD) and molecular beam epitaxy (MBE). The important advantage can be summarizing as follows [29]:

1. Since the laser beam comes from the outsides of the vacuum chamber, broad rang of ambient gas pressure is possible during film growth.

2. The film produced by PLAD is not contaminated because the laser beam ablates the target alone.

3. High speed film formation is possible compared with other methods.

4. Changing the laser repetition rate, pulse energy and the distance between the substrate and the target offers the possibility to control the properties of the thin film.

1.4.2. Pulsed Laser Ablation in Liquid

A recent application of laser ablation is the fabrication of nanoscale materials like nanoparticles, nanowires and nanotubes by PLA in liquids. In this method a solid target is immersed in liquid medium and the laser beem is focused through the liquid onto the surface of the target. The mechanism of the laser ablation in liquid is complicated. However, ref [30] suggests the following mechanism responsible for PLA in liquids.
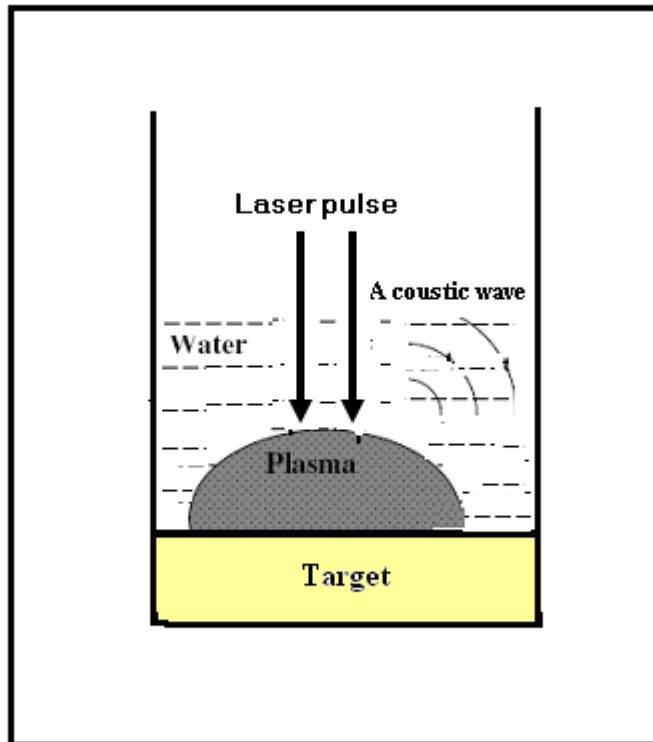
Figure 1-4. Schematic illustration of PLA in water.

When the front part of laser pulse reaches to the surface of target, plasma will develop which we call "laser induced plasma". The laser induced plasma adiabatically expands to create a shock wave under the confinement of liquid. This shock wave induces an extra pressure in the laser induced plasma.

Due to the confined effect of the liquid and laser induced plasma, there are four kinds of chemical reactions taking place [31-32].
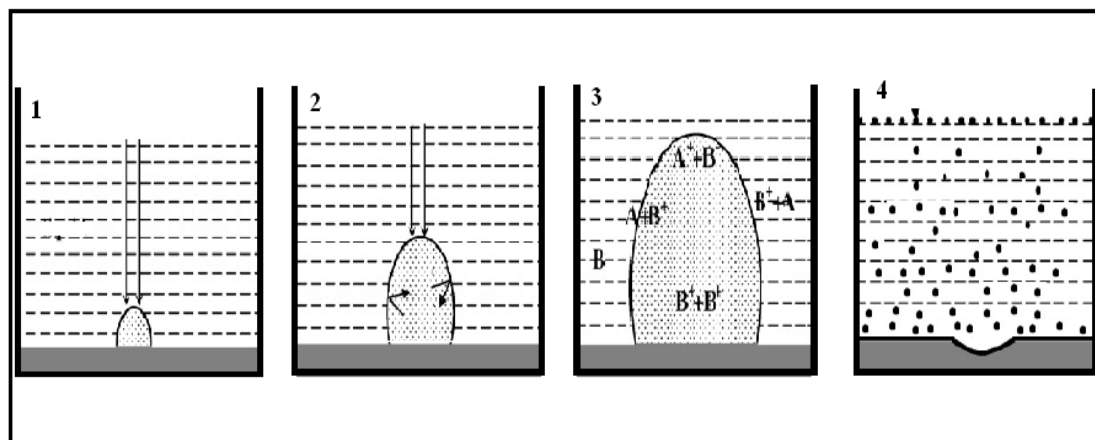
Figure 1-5. The shadowgraph images of the kinds of chemical reaction to prepare nanoparticles in liquid.

The first occurs inside the laser induced plasma. This kind of reaction increases the temperature and the pressure of the target surface. The second kind of chemical reaction occurs at the interface between the laser induced plasma and the liquid. This reaction excites and evaporates the liquid molecules to create the new plasma "plasma induced plasma". The third kind of chemical reaction also occur at the interface between the laser induced plasma and the liquid. This reaction provides a good opportunity for high temperature chemical reactions between the ablated species from the target and the molecules of the liquid. The last kind of chemical reaction occurs inside the liquid between the liquid molecules and ablated species. The amount of species in the fourth step depends on many conditions such as amount of water, laser energy, and pulse

duration [33-34]. Zhu and his group [35] used a 248 nm KrF excimer laser to study the effect of the thickness of the water layer above the Si target on the amount of products. They found that the optimal water thickness above the Si was 1.1 mm. Above this value, the water layer will absorb the laser energy and the water laser ablation becomes weaker due to low laser intensity. On the other hand, when the water layer is less than optimal thickness, the shockwaves, that decay into the target will decay into the acoustic wave. In our Lab, we found that the optimal water thickness for the ablation of Zn target in water ranges between 1 and 2 mm.

Synthesis of nanoparticles by PLA in liquid has many advantages over other methods. The important unique features of this technique can be summarized in the following points:

- The production system does not require costly chambers and high vacuum pumps.

- Pure nano-particles could be produced without the formation of by-products.

- Chemicals such as surfactants can be added to liquids to control the size and aggregation state of NPs by changing the surface charge of the nuclei.

- The entire product could be collected in solution, and the obtained colloid solution is very easy to handle.

- Preparation of well crystallized nanoparticles which could easily be obtained in one-step procedure without subsequent heat-treatments.

1.5. OBJECTIVES

The main objective of this thesis is to design and fabricate a set up for the synthesis of nanoparticles using pulsed laser ablation technique.

The specific objectives of this research are the following:

1. To design and develop a set up for laser ablation process.

2. To prepare nano size materials by pulsed laser ablation in liquids.

3. To control the size of nano particles using different surfactants/ temperature and liquids.

4. To characterize the synthesized nanoparticles using different analytical techniques.

CHAPTER 2

LITERATURE SURVEY

Lasers have been applied to ablate materials in laser based materials processing with the progress of advanced pulsed laser sources since the discovery of the ruby laser in the early 1960s. Since that date, there are two popular methods developed in materials preparation: PLAD to prepare thin films and PLA to produce nanoparticles, nanorods and nanotubes. This chapter will survey PLA to produce nanoparticles in liquids.

The introduction of pulsed laser ablation at the solid-liquid interface was first reported by Patil and co-workers in 1987 [11]. They used a ruby laser to ablate a pure iron target in water to prepare iron oxides with metastable phases. Following their work, Ogale [12] extended the potential of this method for the surface modification of metals, such as metallic oxidation, nitriding, and carbiding. This pioneering work opened new routes for materials processing based on the PLA of solids in various liquids. Since then, the PLA method has been applied to produce a wide range of novel materials, such as metallic alloys and metal oxides nanoparticles.

It was reported by Simakin and coworkers in (2000) that gold and silver nanoparticles can be formed by PLA in water at low and high laser fluence [36]. After laser ablation, gold nanoparticles with diameter ranging between 10-20 nm stuck in ensembles in high fluence (32 J/cm^2) whereas at low fluence separated nanodisks of gold

lie between 12-20 nm were formed. In contrast, the silver products do not seem to depend on the laser fluence.

The effect of the nature of the liquid on the properties of nanoparticles prepared by PLA was investigated by Dolgaev et al. [37]. In their study, a Cu vapor laser beam with energy density of the order of 1-4 J/cm^2 was focused on the surface of titanium and silicon which was kept in the bottom of different media namely: water, ethanol and dichloroethane. For silicon, the liquid nature does not seem to have a significant influence on the size of silicon nanoparticles. The dependence of the composition of nanoparticles on the nature of the liquid was found for ablation of titanium in various liquids. In this regards, Ti, TiC and TiO$_x$ (x=1.04) with the grain size 35 nm were fabricated in ethanol, dichloromethane and water respectively.

Compagnini et al. [38] investigated the effect of the alkane chain length on the optical properties of gold sols produced by PLA using the second harmonic of Nd: YAG laser (wavelength 532 nm, pulse duration of 5 ns, a repetition rate of 10H z and fluence between 1-200 J/cm^2) in different alkane environments. X-Ray photoelectron spectroscopy (XPS) showed that gold nanoparticles only were produced which means there is no chemical interaction between the alkanes and the ablated species.

Changhao et al. [39] reported that ablation at solid- liquid interface of zinc in water with different concentration of SDS (0.01M and 0.001M) could produce zinc hydroxide/ dodecyl sulfate nanocomposite .

It was reported by Wang et al. [40] that carbon nanotubes (CNTs) can be formed by laser ablation of a graphite sample immersed in different solutions such as water, benzene, n-hexane, and carbon tetrachloride. In their work, they revealed the dependence of CNT production on the structure of the target and concluded that more perfect the layer structure of the graphite target, the easier the production of the CNTs.

Magnesium hydroxide nanostructures synthesized using laser ablation technique in water and an aqueous solution of SDS (different concentrations) were also reported [41]. The study demonstrated the formation of ultrafine Magnesium hydroxide nanoparticles with crystallite size 1-2 nm when the liquid used was distilled water while nanofibers with uniform diameter of 4-6 nm and lengths of several hundreds were observed at the concentration of 0.001 M SDS; with the increase of SDS concentrations from 0.1 to 0.5M, nanorods were produced having diameter of 10-30 nm and nanoplatelets from several tens to hundreds of nanometers. When the concentration of SDS in the solution exceeded 0.5M, the amount of nanorods decreased and the amount of nanoparticles increased.

Under the same laser conditions in reference [41], C.H. Liang et al. [42] produced ultrafine titanium oxide using PLA method in distilled water and an aqueous solution of SDS. Ultrafine TiO_2 around 3 nm size was produced at 0.01 M SDS whereas XRD showed amorphous spectra at distilled water with low concentration of SDS (0.001M).

Takeshi Tsuja et al. [43] prepared CoO and Co_3O_4 nanoparticles in water and hexane using Nd:YAG laser light with 355 nm and intensity of 30 mJ/ pulse.

Synthesis of zinc nanoparticles in liquid environment by PLA were also reported by S.C. Singh and R .Gopal [44]. In their work, they placed a zinc rod in the bottom of a glass vessel containing 10 ml 0.05 mM aqueous solution of SDS. Then the surface was irradiated for 60 minutes by second harmonic of Nd:YAG laser operating at 100 mJ energy at repetition rate of 10 Hz. XRD patterns confirmed the presence of all Zn peaks and the high intensity peak occured at $2\theta = 20.4°$ which is the characteristic of a zinc phase. UV-visible plasmon absorption spectrum showed a sharp peak at 232.4 nm that related to Zn and another peak at 370 nm in which confirm the presence of ZnO in the solution.

A.V. Kabashin and M. Meunier [45] reported laser ablation of noble metals in pure water to synthesize colloidal nanoparticles. A femtosecond Ti/ Sapphire laser having wavelength = 800 nm was focused onto a rod of silver and gold placed at the bottom of a 2 mL glass of water. The depth of the target immersed into the liquid was 10 mm. They found that after ablation the color of solutions changed to green and red in the case of silver and gold respectively which indicate the formation of Ag and Au nanoparticles.

It was reported by J.H. Ryu that Calcium tungstate ($CaWo_4$) and calcium molybdate ($CaMoO_4$) colloidal nanoparticles can be prepared by PLA of ceramic samples [46]. They used a fourth harmonic (266 nm) Nd:YAG laser and pulse width of 8 ns possess for 6 hour at room temperature onto sample. The typical sizes of the synthesized nanoparticles were 14 and 25 nm in $CaWo_4$ and $CaMoO_4$ respectively.

Tran X. Phuoc et al. [47] studied the ablation of magnesium in deionized water, SDS, acetone and 2-propanol. They used Nd:YAG laser with wavelength 1064 nm, pulse duration of 5.5 ns and 10 Hz repetition rate to ablate magnesium plate ($25 \times 25 mm^2$ and 1mm thick). After 60 minutes ablation, the color of the media changed depending on the liquid media. When deionized water and deionized water- SDS were used, the color change to became turbid with a milky appearance while the color change to gray and yellow in acetone and in 2-propanol respectively. The presenence of $Mg(OH)_2$ was observed by XRD in the case of deionized water and 0.8 SDS with water whereas both Mg and MgO were observed in the case of acetone and 2-propanol. In additional, TEM showed that the ablation in DW yielded fiber-like nanoparticles having a diameter of about 5–10 nm and length as long as 150 nm whereas materials produced in acetone and 2- propanol had irregular shapes: Spherical, rod-like and triangular and their sizes ranged from 15 to 20nm up to 50 to 100 nm.

Silver, nickel, nickel oxide and silver-nickel alloys were synthesized using CO_2 and Nd-YAG lasers [48]. The silver particles size, that was prepared dissolving nitrate precursors of silver, depends upon the laser processing conditions such as laser energy, and wavelength. In addition, highly porous dual phase nickel-nickel oxide and silver-nickel alloys composite powders were synthesized by PLA process at laser power densities of $37.5 kW/cm^2$, $50.0 kW/cm^2$ and $87.5 kW/cm^2$ respectively.

Zinc Oxide nanoparticles are prepared by PLA of zinc in water- surfactants media (sodium dodecyl sulfate SDS, lauryldimethylaminoacetic acidic betaine LDA,

cetyltrimethylammonium bromide CTAB, octaethylene glycol monododecyl OGM) [49]. According to this reference, not only the surfactant molecules in the solution have an effect on the particle size but also there is an effect of the concentration of the surfactant itself. They found that the average particle size of ZnO nanoparticles decrease with the increase of OGM and LDA concentrations. To explain these results, they suggested that the smaller particles of LDA and OGM may occur due to the electric attractive force between positive electric charge of ZnO and the negative charge at the end of LDA hydrophilic surfactant ($CH_3(CH_2)_{11}N(CH_2COO^-)$) or a weak negative charge at the oxygen atom in the OGM ($C_{12}H_{25}(O^{\delta-}CH_2CH_2)OH$). As a result of this force, LDA and OGM molecules surrounding ZnO nanoparticles probably lead to prevent more growth of ZnO. Moreover, the decrease in nanoparticles size at high concentration of LDA and OGM could occur when the concentration of LDA and OGM exceeded the critical micelles concentration (CMC), the concentration above which surfactants form micelles in the solution.

Yoshie Ishikawa et al [50] studied the effect of liquid media temperature on the ZnO nanoparticles produced by PLA in liquid environment. In their experiment, an aluminum block prepared with dry hot bath was used to make the liquid temperature at 40, 60, 80 ºC during 40 minutes laser ablation. The third harmonic 355 nm of Nd:YAG laser was focused onto 10 cm^3 of deionized water in presence of LDA and CTAB surfactants. When the solution was only deionized water, the shape and the size of ZnO nanoparticles ablated at 40ºC were similar to those prepared at room temperature whereas nanorods around 200 nm long and nanorods like flower with 500-600 nm length

and 200 nm wide were observed at 60 and 80ºC respectively. In surfactant aqueous solution, nanorods, like in deionized water, were observed in LDA and CTAB.

R.K. Thareja [51] synthesized zinc oxide nanoparticles by PLA technique in water, isopropanol and acetone media. The Nd:YAG laser beam was focused onto a Zn target for 3-4 hours at room temperature. XRD diffraction in all liquids showed the same peaks with the standard diffraction pattern of ZnO. Spherical nanoparticles in the range of 14-20 nm yielded in deionized water and isopropanol whereas in acetone there were two types of particles: spherical nanoparticles ($\approx$ 100 nm) and platelets ($\approx$1000 nm).

Chun He et al [52] studied the effect of pH of the liquid media on the size distribution of ZnO nanoparticles prepared by PLA in deionized water and aqueous solutions. In their work, a focused Nd:YAG laser with a third harmonic (λ=355 nm) and laser intensity of 100 mJ/pulse was applied for 60 min onto a Zn plate placed in different liquid media namely: HCL (PH=5.36), NaCl (PH=7.15), deionized water (PH=7.51) and. NaOH (PH=11.98). The results showed that the average sizes of ZnO nanoparticles produced in HCL and NaOH were 15 nm and 20 nm respectively whereas in deionized water and NaCl the average sizes were 23 nm and 26 nm respectively. They concluded that smaller nanoparticles of ZnO were found in low and high values of pH which indicates the effect of OH^- and H^+ radicals on the growth of ZnO.

Chun He et al. [53] investigated the aging effects of ZnO nanoparticles prepared by PLA in CTAB media on the morphology and optical properties. They found spindle like

nanoparticles with 2.2 μm length and 300 nm width in CTAB solution after aging for 3 days. It was found also that the average size of these spindle increases with aging time.

S.C. Singh and R. Gopal demonstrated a new method to fabricate ZnO nanoparticles by ablation of Zn metal placed in distilled water in the presence of SDS. Oxygen gas was introduced using special set up to the center of ablation [54]. XRD patterns showed ZnO peaks and two extra peaks at $2\theta = 33.5º$ and $59.5º$ that could be an indication of fabrication of zinc oxyhydroxide (ZnOOH). The average size of the particles calculated from TEM images was around 13.7 nm. UV–visible absorption spectra of colloidal solution showed two peaks at 365.5 nm indicating formation of ZnO nanoparticles, and at 487.7 nm which may be due to the formation of zinc oxyhydroxide (ZnOOH) nanoparticles. The authors also found SDS-coated ZnO and oxyhydroxide nanoparticles by Fourier transform infrared (FTIR) spectroscopy in mid and far IR regions.

CHAPTER 3

EXPERIMENTAL WORK AND CHARACTERIZATION

TECHNIQUES

This chapter describes the experimental set up and the basic principle of the various physical techniques used to synthesize and study the properties of the nanoparticles using PLA method in liquid environment. The analytical techniques include: X-Ray Diffraction (XRD), atomic force microscopy (AFM), scanning electron microscopy (SEM) ultraviolet and visible (UV-Vis) photspectroscopy, X-ray photoelectron spectroscopy (XPS), photoluminescence spectroscopy and Fourier transform infrared (FTIR).

3.1. SYNTHESIS EXPERIMENTAL SET UP

A schematic diagram of the laser based setup for synthesis of nanoparticles using PLA in liquid is depicted in Fig. 3-1. A Q-switched Nd-YAG laser (Spectra physics Model GCR 100) operating at 355 nm wavelength using third harmonic generator was employed as an excitation source. It can deliver maximum pulse energy of 300 mJ with a pulse width of 8 ns, and operates at a 10 Hz pulse repetition rate. The collimated beam at 355 nm is tightly focused on the target sample using a convex lens to create a spark or

breakdown in the sample. The laser energy was measured with a calibrated energy meter (Ophir model 300) for the study of dependence of nano particle yield on incident laser energy. In this experiment, we placed a 2 mm diameter aperture inside the path of laser beam in order to get a uniform beam shape.
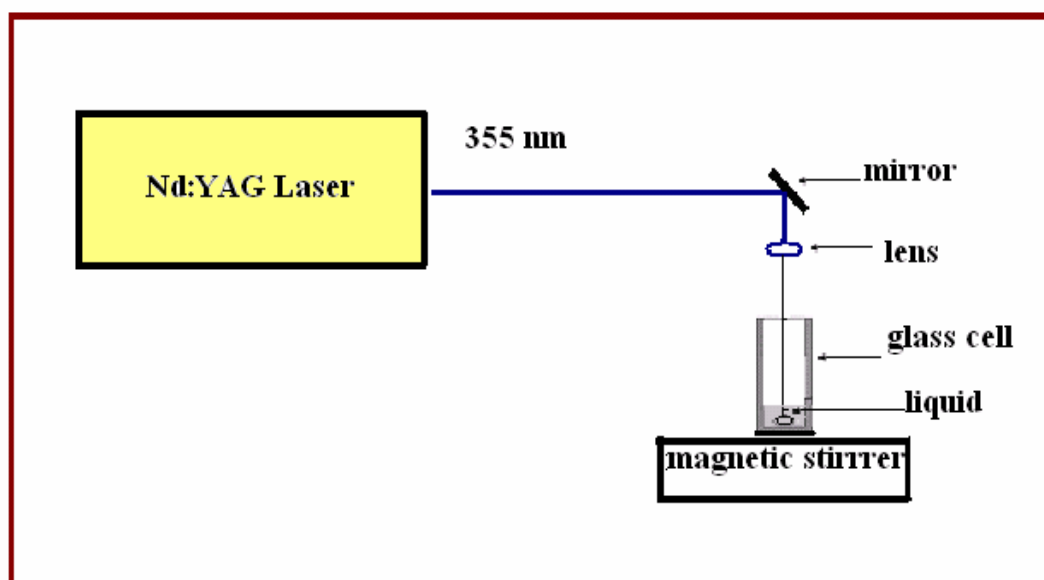
Figure 3-1. Schematic diagram of experimental setup for synthesis of nanoparticles by PLA in liquids.

For the synthesis of nanoparticles, a high-purity metallic plate of zinc or tin is fixed at the bottom of a glass cell as the target, and is rotated using a home made magnetic stirrer to avoid a deep ablation traces or crusts. Typical laser pulse energy for PLA process was between 40-130 millijoules per pulse. The laser beam was focused by a lens with a focal length of 250 mm in order to get sufficient laser fluence for the ablation.

The typical diameter of the laser spot on a bulk target was ~ 0.08 mm and the typical

liquid volume was 10 ml. Some chemicals such as surfactants were added to the solution

to control the size and aggregation of the products size and aggregation of the products.

After laser irradiation for certain time period, colloidal solutions of nanoparticles were

obtained. The colloidal suspension was separated from water after laser irradiation using

a centrifuge.
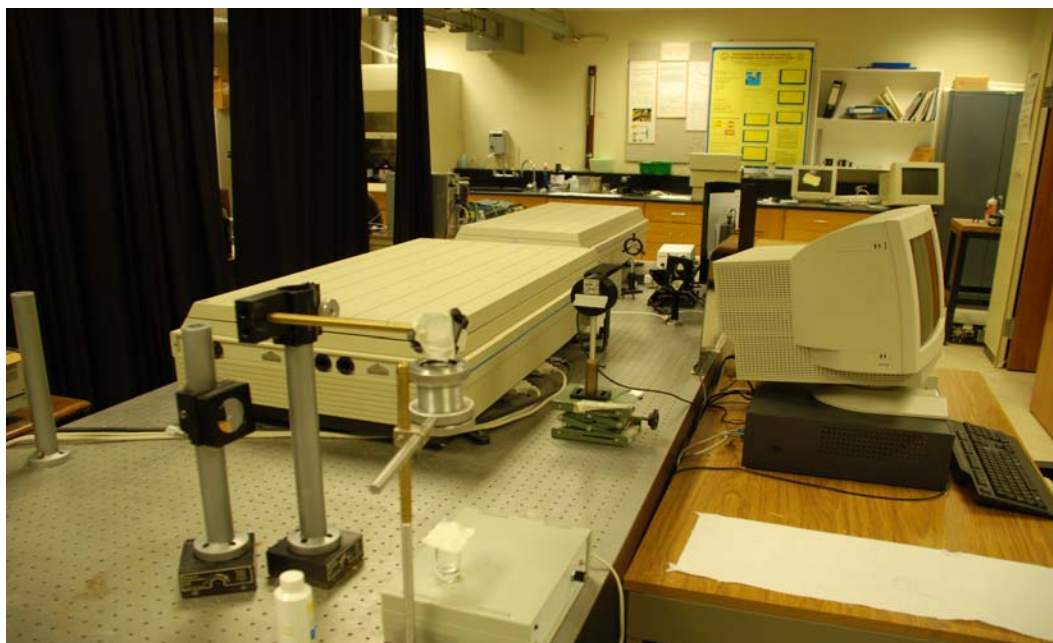
Figure 3-2. Photograph of experimental PLA set up in laser research laboratory of KFUPM.

The first objective of this work was to design a set up to produce nanoparticles of

specific size by pulsed laser ablation in liquid media. For this purpose we optimized the

following components of the set up:

- Magnetic stirrer.
- Glass cell.
- Sample holder.
- Focal length of the focusing lens

Figure 3-2 shows photograph of the home made parts and laser set up applied for synthesis of nanoparticles using PLA technique.

3.2. CHARACTERIZATION TECHNIQUES

In order to study the properties of nanoscale materials prepared by PLA in liquids, a variety of analysis techniques were applied for the characterization of products. Morphological observation by (SEM), structure and grain sizes by (XRD) and Atomic Force Microscope (AFM) , composition by XPS and optical properties by FTIR, UV-Vis and spectroflurometer were conducted.

3.2.1. X- ray diffraction (XRD)

X-Ray Diffraction (XRD) is a powerful technique used for the determination of crystalline, crystal structures, identification of unknown materials and lattice constants of nanoparticles, nanowires and thin films. Historically, the diffraction of X-Ray from the crystal materials solved for the first time by Bragg in 1913 who regarded a crystal as made out of parallel planes of atoms which spaced with a distance "d". (Fig 3-1). XRD

is based on constructive interference of monochromatic X-rays by a crystalline sample. The condition of the constructive diffraction is given by the Bragg equation

$$n\lambda = 2d\sin\theta$$

Where the integer n is the order of the diffracted beam, d is the distance between the atomic planes in the crystal, θ is the angle of constructive diffraction from the plane, and λ is the x-ray wavelength. Bragg equation tells us that, if the wavelength and the angle of the incident X-Ray are known, the distance between planes of the atoms can be calculated.
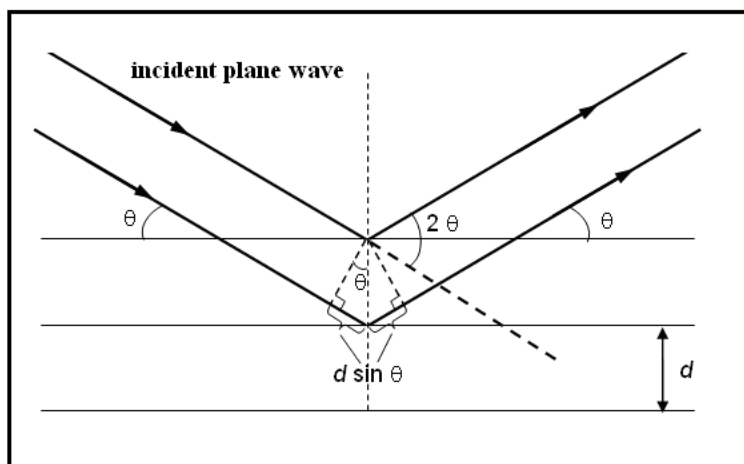
Figure 3-3. Bragg diffraction schematic.

In a typical XRD, X-rays are generated within a sealed tube that is under vacuum. A current is applied that heats a filament within the tube, the higher the current the greater the number of electrons emitted from the filament. This generation of electrons is

analogous to the production of electrons in a television picture tube. A high voltage, typically 15-60 kilovolts, is applied within the tube. This high voltage accelerates the electrons, which then hit a target, usually made of copper. When these electrons hit the target, X-rays are produced [55-56].

When a collimated beam of X-Ray hits a sample and is diffracted, the distances between the atomic planes of the sample can be measured by applying Bragg's Law. The intensity of the diffracted X-rays is measured as a function of the diffraction angle 2θ. A series of peaks occur where each peak corresponds to x-ray diffracted from a specific set of planes in the specimen. Peak broadening in XRD peaks, or in other words increase in full width at half maximum (FWHM), can be caused due to three reasons: the average nano crystalline size, Instrumental effects and lattice strains.

The broadening due the average nano crystalline size is given by Scherrer equation that is obtained from the derivative of Bragg's law keeping the wavelength constant and allowing the diffraction angle and the Bragg spacing to vary. Therefore the full width at half maximum (FWHM) of diffraction peak $B_{crystallite}$ is given by:

$$B_{crystallite} = \frac{k\lambda}{L\,\cos\theta}$$

Where λ is the X-ray wavelength, L is the crystallite size measured in a direction perpendicular to the surface of the specimen, θ is the diffraction angle, and k is the Scherrer's constant of the order of unity ($\approx$1) for usual crystal.

The broadening of the peak due to the presence of lattice strain (variation due to different crystals in the samples) is given by [57]:

$$B_{strain} = \frac{2\varepsilon}{\cot\theta}$$

where ϵ is the elastic strain.

To estimate the instrument effect on the peak broadening, the broadening of a well-annealed powder can be calculated, where the grain size is very large as compared to Scherrer effect and the lattice strain.

The data of XRD in the present thesis were recorded on a Shimadzu XRD- 6000 X-ray diffractometer under the following operation condition:

- Copper K X-ray radiation (λ=1.5406 A) from a broad focus tube at 40 KV and 30mA

- Scanning speed for data collection was 2 degree /min.

- Angle scanned was 20-80 degree (2θ) for most samples.

- Aluminum and glass were used as a substrate.

3.2.2. Atomic force microscopy (AFM)

Atomic Force Microscopy (AFM) is one of the family of scanning probe microscopy (SPM) that depend on a moving probe (tip) that rasters the surface, and it provides nanometer-scale information of the test sample. The laboratory setup for an AFM (Fig.3-4) includes: a tip (typically made from silicon or silicon nitride), cantilever, laser, photodiode, electronics feedback and piezoelectric.

Depending on the application of the AFM, it can be operated in a number of modes. In general, there are three modes: contact modes (A tip is scanned across the surface while a feedback loop maintains a constant cantilever deflection (force). In non-contact modes the tip does not touch the surface. Instead, it oscillates above the sample. In tapping modes the cantilever with attached tip is oscillated at its resonant frequency and scanned across the sample surface.
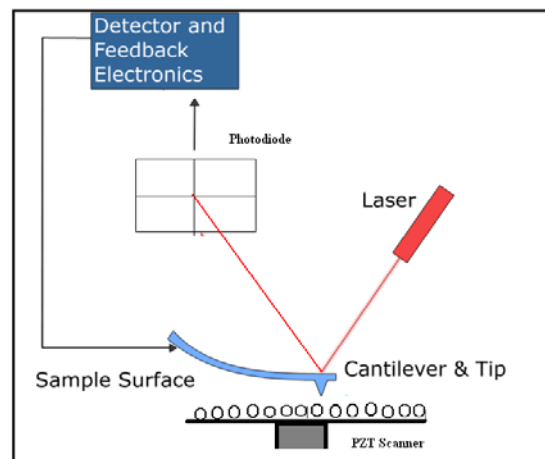
Figure 3-4. Basic principle of AFM technique.

The basic principle of AFM depends on the van der Waals force (interatomic force between a tip and surface). Van der Waals force between the tip and the surface of the sample contain two distance regimes attractive force (contact mode) or repulsive forces (noncontact mode). As the tip (either in attractive regime or repulsive regime) scans the surface of the sample, moving up and down, the force between the tip and sample causes the cantilever to twist. A laser beam, which focuses onto the back of the reflective cantilever, reflects off the cantilever surface to a split photodiode. The photodiodes is position-sensitive and can discern, from the reflected laser beam up-and-down motion, the topographic sample variations. A feedback circuit is used to adjust the tip-to-sample distance to maintain a constant force between the tip and the sample.

3.2.3. Scanning electron microscopy (SEM)

Scanning electron microscope (SEM), first obtained by Max Knoll in 1935, is an electron microscopy technique that is used for the examination and analysis of the microstructure morphology and chemical composition characterizations.

In this technique, a source of electrons having a fine spot size is focused into a fine probe by one or two condenser lenses in a high-vacuum environment. These electrons are scanned over the sample by deflection coils. As the electrons strike and penetrate the surface, a number of interactions occur that result in the emission of secondary electrons and electromagnetic radiation from the sample. The secondary electrons, which are ejected from a core orbital of the specimen atoms of the inelastic scattering by incident

electron beam, can be detected by scintillator system, which emits light when electrons hit it, the light is converted into a pulse of electrons which results in images with a well-defined [58-60].

3.2.4. UV-Visible spectroscopy

UV-Vis spectroscopy is a characterization technique to measure optical or electronic properties of different solid and liquid materials by the transmission, absorption and reflection in the visible and UV region. UV-Vis spectrometer consists of: source of light such as a incandescent lamp for the visible or deuterium lamp for the ultraviolet region, sample holder, reference cell (in double beam) and detector such as photodiode by using monochromatic to filter the light. UV-Vis spectrometer has either single beam or double beam. In single beam the intensity of light pass through the sample cell. Light that strikes the sample could be absorbed, reflected or transmitted. When the sample is a solution in a cell, the intensity of light before it passes through the sample "I_o" and "I" represent the intensity of light after through the sample, the transmittance "T" is defined as the ratio I / I_o and the absorbance "A" is given by Beer Lambert's law:

$$A = -\log_{10}(I / I_0) = \varepsilon.c.L$$

Where ε is a constant known as the molar absorptivity, c is the concentration of the absorbing species into the solution. L is absorption path length.

In the present work, a double beam scanning spectrometer (Model JASCO V-570) with wavelength range 200 nm to 800 nm was used.

3.2.5. Fluorescence spectroscopy

Photoluminescence, abbreviated **PL,** is the optical radiation emitted by a semiconducting crystal after excitation with light source**.**

If a light particle (photon) has energy greater than the band gap energy, then it can be absorbed and thereby raise an electron from the valence band up to the conduction band across the energy gap (band gap). In this process of photoexcitation, the electron generally has excess energy which it loses before coming to rest at the lowest energy level in the conduction band. The electron eventually falls back down to the valence band. As it falls down, the energy it loses is converted back into a luminescent photon which is emitted from the material. Thus the energy of the emitted photon is a direct measure of the band gap energy, E_g. The process of photon excitation followed by photon emission is called photoluminescence. In this work, specroflurometer (Model Shimadzu RF-5301 PC) equipped with 150-W Xe lamp as the excitation source was used at different wavelength excitions.

3.2.6. X-ray photoelectron spectroscopy

X-Ray Photoelectron Spectroscopy (XPS) is an analytical technique that provides the elemental composition, empirical formula, chemical state and electronic state of the elements that exist within all elements except H and He. The basic requirements for an XPS system are: a monochromatic x-ray source, an electron energy analyzer (which can disperse the emitted electrons according to their speeds, and thereby measure the flux of emitted electrons of a particular energy), and an ultra high vacuum environment. In a standard XPS experiment an x-ray photon strikes and ejects a core electron from the atom. The ejected electrons are dispersed by the energy analyzer according to their kinetic energies. The basic XPS spectrometer is illustrated schematically in figure 3-6.
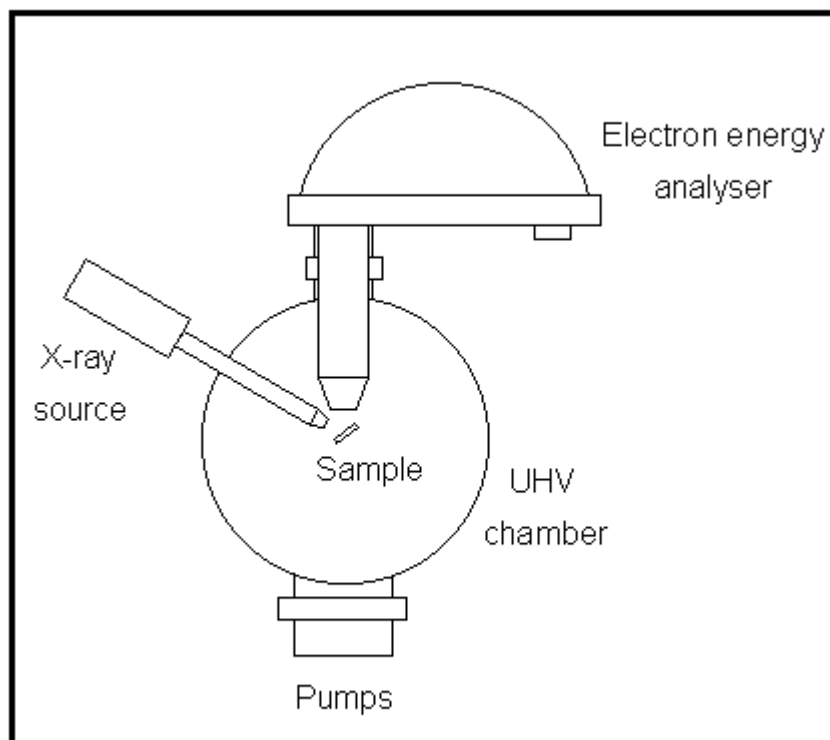
Figure 3-5. The schematic illustration of XPS main components.

The basic physics of XPS technique can be described by the Einstein equation:

$$E_B = h\nu - E_K - E_R - \Phi - \delta E$$

Where E_B is the binding energy of the electron in the atom which vary with the type of atom and all binding energy for all elements in various chemical environments have been measured and recorded in reference tables and handbooks. *KE* is the kinetic energy of the emitted electron that is measured by XPS spectrometer. *hv* is the energy of the photons in X-ray source. E_R is the recoil energy which is very small and usually can be neglected, Φ is the work function, and *δE* is the charge shift.
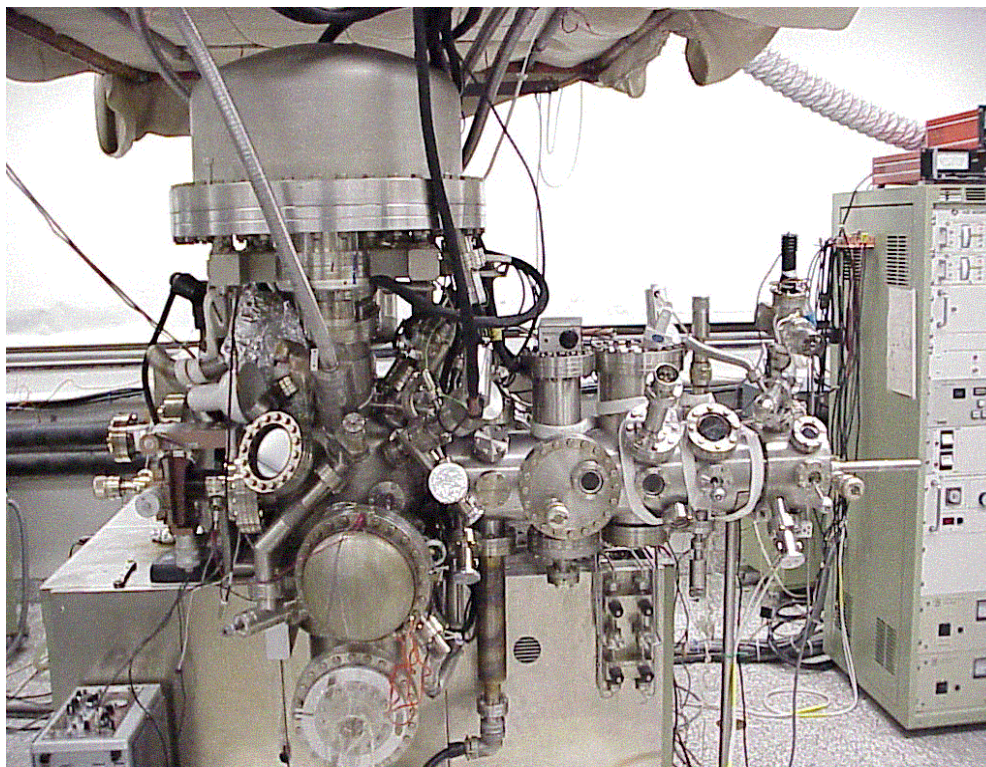
Figure 3-6. XPS Surface Science Laboratory, Physics Department, KFUPM.

3.2.7. Fourier Transform Infrared spectroscopy (FTIR)

Fourier Transform Infrared (FTIR) spectroscopy is a spectroscopic technique that provides information about the chemical bonding or molecular structure of materials. Basically, IR spectra are obtained by detecting changes in transmittance (or absorption) intensity as a function of frequency. FTIR technique works based on the fact that bonds and groups of bonds vibrate at characteristic frequencies. A typical FTIR consists of a beam splitter, a fixed mirror and a scanning mirror. As shown in Fig.3-8, light from the source is separated into two parts and then recombines at the beam splitter after

reflection by the two mirrors. Interference takes place due to the path difference between the two beams. The output beam from the interferometer is recorded as a function of path difference, and is called the interferogram. The IR spectrum can be obtained by calculating the Fourier transform of the interferogram.
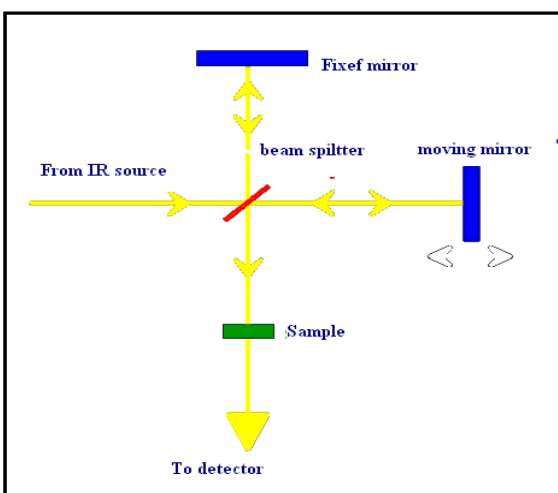
Figure 3-7. Schematic diagram of an FTIR.

CHAPTER 4

RESULTS AND DISCUUISIONS

4.1. SYNTHESIS AND CHARACTERIZATION OF ZINC OXIDE NANOPARTICLES

Zinc oxide (ZnO) is an n type semiconductor with a wide band gap of 3.1-3.3 eV corresponding wavelength ranging from 375.7 to 400 nm. ZnO has high exciton binding energy (60 meV) and has been studied as an optoelectronic, transparent, conducting, and piezoelectric material. It has a wurtzite crystal structure and lattice parameters: a=3.249 Å and c=5.205 Å in the ratio of c/a ~ 1.602. Figure (4-1) shows how the close-packed wurtzite lattice of ZnO can be constructed from individual Zn and O atoms. Table 4-1summarizes the important physical properties of ZnO [61]. References [62] give comprehensive information on ZnO properties.

● O   ● Zn
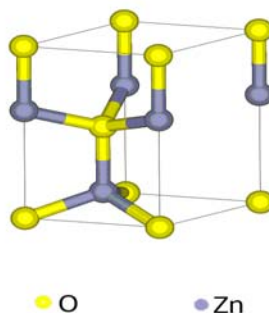
Figure 4-1. Wurtzite crystal structure of ZnO.

Table 4-1. The physical properties of ZnO.

Properties	Value
Lattice constants (T = 300 K)	
a_0	0.32469 nm
c_0	0.52069 nm
Density	5.606 g/cm^3
Melting point	2248 K
Relative dielectric constant	8.66
Gap Energy	3.4 eV, direct
Intrinsic carrier concentration	$< 10^6$ cm^{-3}
Exciton binding Energy	60 meV
Electron effective mass	0.24
Electron mobility (T = 300 K)	200 cm^2/V s
Hole effective mass	0.59
Hole mobility (T = 300 K)	5-50 cm^2/V s

Optical properties of bulk ZnO show that ZnO nanoparticles have a wide band gap of 3.4 eV. In order to explain the different luminescences of ZnO, researchers concluded that the UV/violet luminescence of the ZnO nanoparticles is due to the recombination of free electrons in the conduction band and holes in the valence band. The visible luminescence of ZnO can also be due to certain defects in the ZnO matrix which can trap electrons and radiate photons [63]. Vanheusden et al. [64] found that oxygen vacancies are responsible for the blue/green luminescence in the ZnO. Figure 4-2 shows the energy levels created by different native defects. Those energy levels can have different effects on the optical properties of ZnO. From the diagram 4.2, visible photoluminescence in regions of orange, green, blue, and violet is caused by radiative transition emission from deep donor levels of neutral zinc interstitials (Zn_i) to acceptor

levels of singly ionized oxygen interstitials (O_i-), singly ionized zinc vacancies (V_{Zn}-), neutral zinc vacancies (V_{Zn}), and valence band, respectively [62].
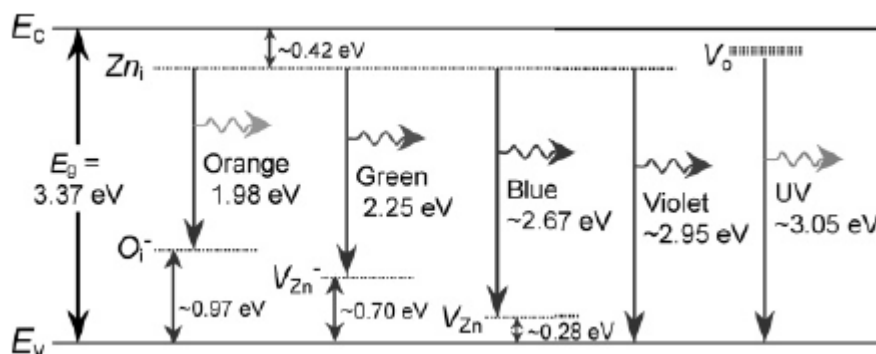
Figure 4-2. Energy level diagram of intrinsic defects in ZnO nanoparticles.

Different chemical methods of preparation have been reported for nanosized ZnO, like the sol–gel method [65], precipitation in alcoholic medium [66], Polyol synthesis <mark>[10] D. Jezequel, J. Guenot, N. Jouini and N.F. Fievet, *J. Mater. Res.* **10** (1995), p. 77. **Full Text** via CrossRef | View Record in Scopus | Cited By in Scopus (68)</mark>[67], etc. in addition to above mentioned chemical methods, other methods have been applied to synthesis of ZnO nanostructures such as: sputtering [68], molecular beam epitaxy [69], hydrothermal [70], electrodepostion [71]. However, most of these techniques are costly and complex in order to synthesis and control the particle size and its uniform in size. Laser ablation is one of the emerging techniques for the synthesis of nano structure ZnO.

In the next sections, the synthesis of nano structure ZnO nanoparticles by (PLA) in different solutions and the structural and optical properties of ZnO will be discussed in details.

For the synthesis of nano structure ZnO nanoparticles by (PLA) in water, a laser based setup was designed and fabricated locally which is depicted in Fig. 4-1. For synthesis of ZnO nanoparticles of these particles, a high-purity metallic Zinc foil, 1 mm thick of purity 99.99% (Sigma Aldrich Company) was fixed at the bottom of a glass cell as the target, and was rotated by a home made magnetic stirrer to avoid deep ablation crusts. Typical laser pulse energy for PLA process was between 40-130 milli joules per pulse. The laser beam was focused by a lens with a focal length of 250 mm to get sufficient laser fluence for the ablation. The typical diameter of the laser spot on a bulk target was ~ 0.08 mm and the typical liquid volume was 10 ml.

After laser irradiation time of 40 min, a colloidal solution of ZnO based nano materials was obtained. The colloidal suspension was separated from the water using centrifuge machine.

A variety of analysis techniques were applied for the characterization of ZnO products prepared by PLA in water. Morphological was characterization by scanning-electron microscopy (SEM). The structure and grain size were obtained using X Ray Diffraction (XRD). The composition of the products was studied by means of (XPS). Optical properties of products were studied using UV-Visible spectrometer and fluorescence spectroscopy

The X ray diffraction study of ZnO nanoparticles prepared by PLA in water was carried out on dry film obtained by coating nanoparticles suspension on glass substrate. Figure 4-3 shows the XRD spectra of the bulk Zn target and ZnO nanoparticles

synthesized using PLA in deionized water. The diffraction spectrum and interplane spacing of the products was in agreement with the standard diffraction pattern of wurtzite ZnO, confirming the formation of wurtzite ZnO nanocrystals implying that ablated Zn species were oxidized in the presence of water. The main dominant peaks of ZnO were identified at $2\theta = 31.3^o$, 34.8^o, 36.4^o, 48.2^o, 57.0^o, 63.2^o and 68.3^o. The average size "d" of ZnO nanoparticles calculated using Scherrer formula at angle 36.4^o is 38 nm.
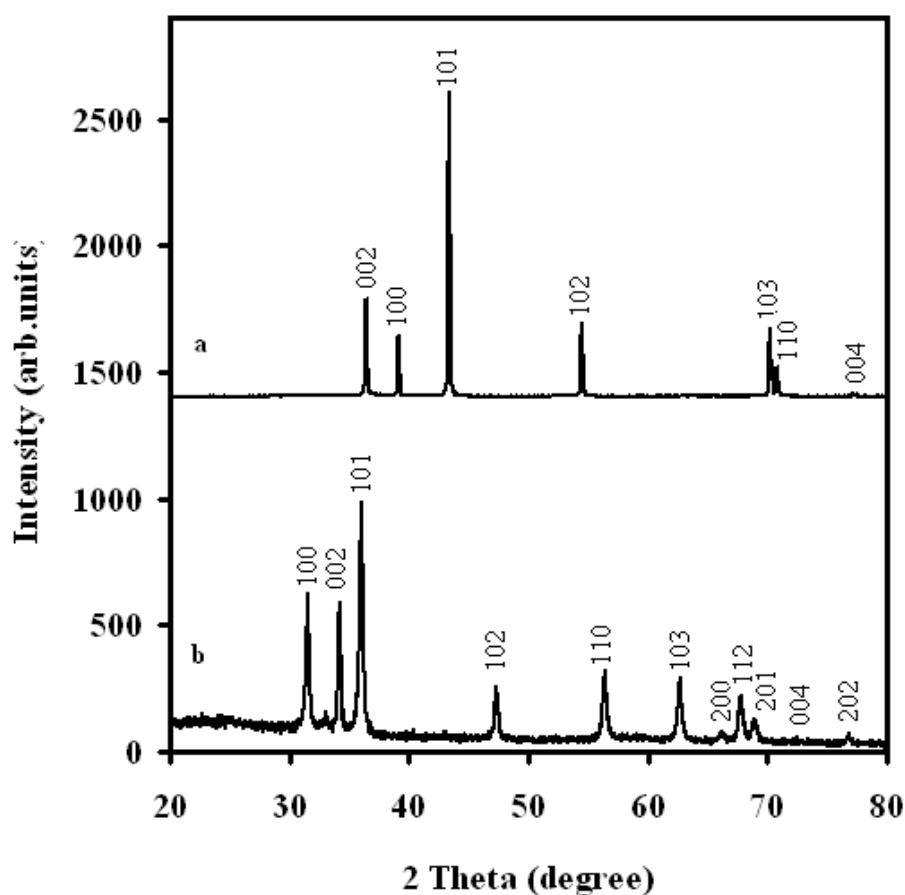
Figure 4-3. X-ray diffraction patterns of a) bulk Zn and b) ZnO nanoparticles prepared by PLA in water.

As mentioned earlier, ZnO has a hexagonal structure with two lattice parameters a and c. From the XRD data, one can calculate the lattice parameters a and c [72]:

the plane spacing that given in the hexagonal structure is

$$1/d^2 = (4/3\ a^2)\ (h^2 + hk + k^2) + l^2/c^2 \ \dots\dots\dots\dots\dots\dots\dots..\dots\dots\dots\dots\dots\dots\dots.1$$

Where hkl are the miller indices

Combining equation (1) and Bragg law

$$sin^2\theta = A\ (h^2 + hk + K^2) + C\ l^2 \ \dots\dots\dots\dots\dots\dots\dots\dots\dots\dots\dots\dots\dots\dots.2$$

Where $A = (\lambda^2/3a^2)$ and $C = (\lambda^2/4c^2)$

From the structure factor equation for a hexagonal structure, the selection rule is given

$$h^2 + hk + k^2 = 0,\ 1,\ 3,4,7,9 \ \dots\dots\dots\dots\dots\dots\dots\dots\dots\dots\dots.\dots\dots\dots.3$$

To calculate the lattice parameter a, from the XRD peaks, we can find 2θ and then θ for all peaks. Calculate $sin^2\theta$ for all miller indices and then divided sin2θ values by integers 1, 3, 4, 7, 9. The common value will appear when $l = 0$ this value represent A in equation 2.

$$\text{Lattice parameter}\ a = \frac{\lambda}{\sqrt{3A}}\ .$$

To calculate the lattice parameter c, we rewrite equation 3 as

$C \, l^2 = sin^2\theta - A \, (h^2 + hk + k^2)$. The common value, that appear when l=2, represent the value C. From C, we can find the lattice parameter c as

$$c = \frac{\lambda}{2\sqrt{C}}$$

Tables 4-2 and 4-3 represents show the data obtaining from XRD and its analysis to calculate the lattices parameter a and c.

Table 4-2. Calculation of lattice parameter (*a*).

Peak#	2θ	Sinθ	Sin²θ	Sin²θ/3	Sin²θ/5	Sin²θ/7	Sin²θ/9	hkl
1	31.62	0.272455	**0.074232**	0.024744	0.018558	0.010605	0.008248	100
2	34.38	0.295623	0.087393	0.029131	0.021848	0.012485	0.00971	2
3	36.00	0.309043	0.095507	0.031836	0.023877	0.013644	0.010612	101
4	47.41	0.402056	0.161649	0.053883	0.040412	0.023093	0.017961	102
5	56.56	0.473812	0.224497	**0.074832**	0.056124	0.032071	0.024944	110
6	62.06	0.515487	0.265727	0.088576	0.066432	0.037961	0.029525	103
7	66.26	0.546559	0.298727	0.099576	**0.074682**	0.042675	0.033192	200
8	67.73	0.557256	0.310534	0.103511	0.025878	0.044362	0.034504	112
9	69.28	0.568418	0.323099	0.1077	0.026925	0.046157	0.0359	201

From Table (4.2) the value of A is equal 0.074582. Hence, the lattice parameter a will be 3.256 A.

Table 4-3. Calculation of lattice parameter (*c*)

Peak#	2θ	Sinθ	Sin²θ	Sin²θ - A	Sin²θ -3A	hkl
1	31.62	0.272455	0.074232	-9.8E-05	-0.14876	100
2	34.38	0.295623	**0.087393**	0.013063	-0.1356	002
3	36.00	0.309043	0.095507	0.021177	-0.12748	101
4	47.41	0.402056	0.161649	**0.087319**	-0.06134	102
5	56.36	0.472274	0.223043	0.148713	5.26E-05	110
6	62.06	0.515487	0.265727	0.191397	0.042737	103
7	66.26	0.546559	0.298727	0.224397	0.075737	200
8	67.73	0.557256	0.310534	0.236204	**0.087544**	112
9	69.28	0.568418	0.323099	0.248769	0.100109	201

From Table (4.3) $4C = 0.087393$ *A* and the lattice parameter $c = 5.210$ A. The values of

the lattice parameters *a* and *c* of zinc oxide produced by means of PLA of zinc plate in

water are consistent with values of lattice parameters of bulk ZnO.

In order to confirm the result of XRD, typical SEM images of ZnO produced by PLA at different laser energies (80-100-120) mJ were carried out and depicted in figures (4-4, 4-5 and 4-6). From the figures, it is clear that the morphology of products was different at various laser energy. The morphology at low energy was like nanorods and at high energy the morphology changes to spherical shape. Changing of the morphology of ZnO products could be due to the change of the intensity, temperature and pressure of plasma which could lead to change in the growth of products.
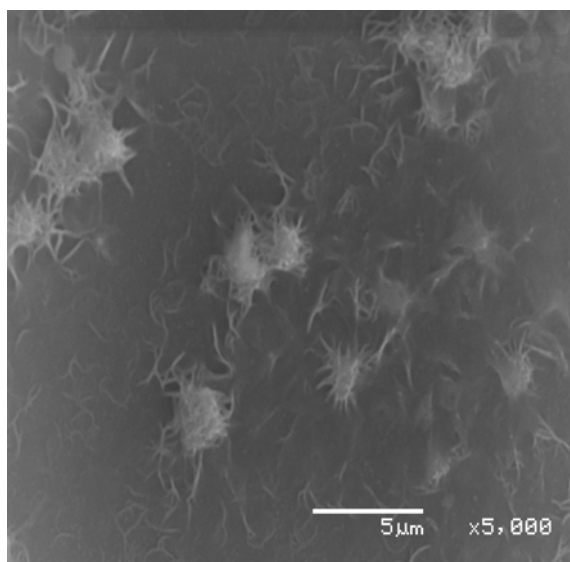
Figure 4-4. A typical SEM image of ZnO nanostructure prepared by pulsed laser ablation in water at 80 mJ.
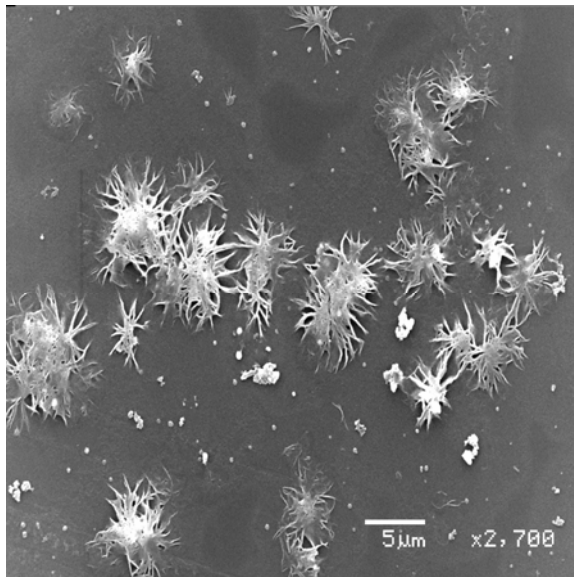
Figure 4-5. A typical SEM image of ZnO nanoparticles prepared by pulsed laser ablation in water at 100 mJ.
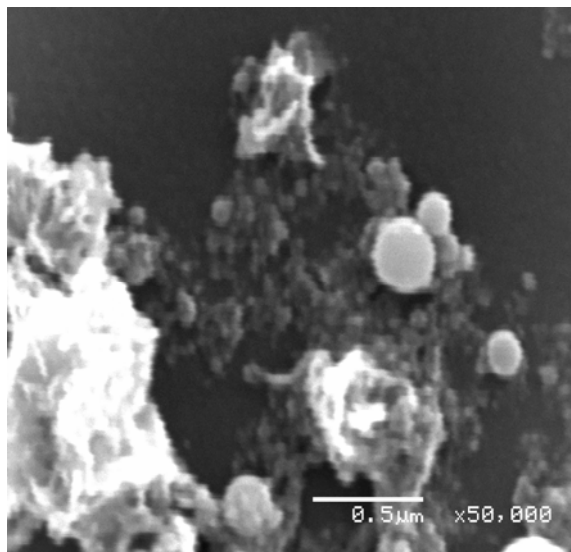
Figure 4-6. A typical SEM image of ZnO nanoparticles prepared by pulsed laser ablation in water at 120 mJ.

X-ray photoelectron spectroscopy (XPS) is surface analysis technique used to measures the elemental composition and chemical state of the surface of the elements that exists within a material (top 1−10 nm usually). In order to study the elemental compositions and purity of the products, X-ray photoelectron spectroscopic studies were performed in the binding energy range ~0-600 eV. The XPS spectrum showed that all peaks are of carbon, oxygen and zinc (see figure 4-7) and no other impurities were found. Due to the charge shift onto the surface of the sample, all the binding energy positions were corrected with reference to C1s binding energy position at 284.8 eV. The XPS scan confirms the purity of the nanoparticle products.
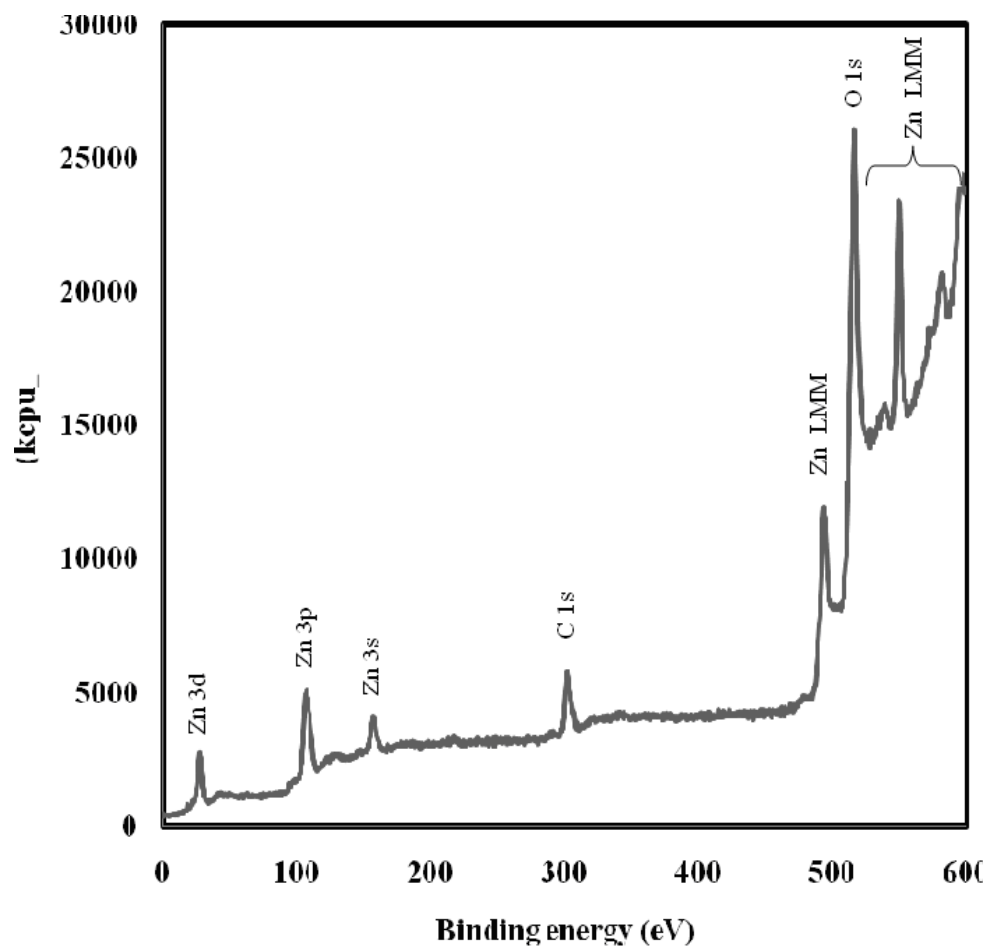
Figure 4-7. XPS spectrum of the ZnO nanoparticles prepared by PLA in water.

A resolved spectrum in the energy range 525-535 eV showed a broad peak at about 530 eV corresponding to O1s and the fitting of this peak (figure 4-8) shows two Gaussian peaks: one at 530.04 ± 0.2 eV corresponding to the O-Zn bonding [73], and one at 531.74 ± 0.2 eV which can be attributed due to either ZnOH or/and moisture on the surface [74].
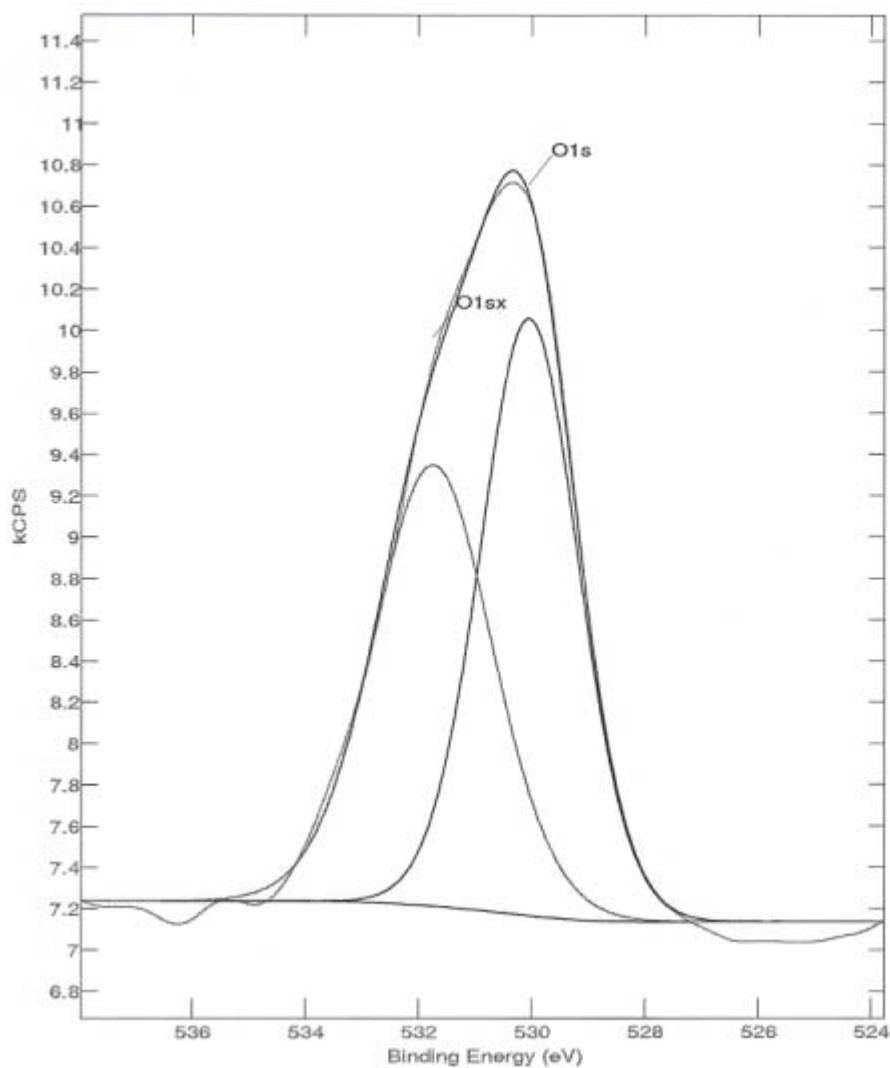
Figure 4-8. The XPS of the fitting O1s spectrum.

A resolved spectrum in the energy range 1015-1030 eV (Fig. 4-9) shows a symmetric peak centered at 1021.29 ± 0.2 eV corresponding to Zn $2p_{2/3}$. This value has a shift to lower binding energy which is 1021.8 eV in standard ZnO. This shift in the peak position toward lower enegy was caused by the increase in the number of zinc atoms in the ZnO nanocrystals [74]. Similarr phenomena have been reported in [75].
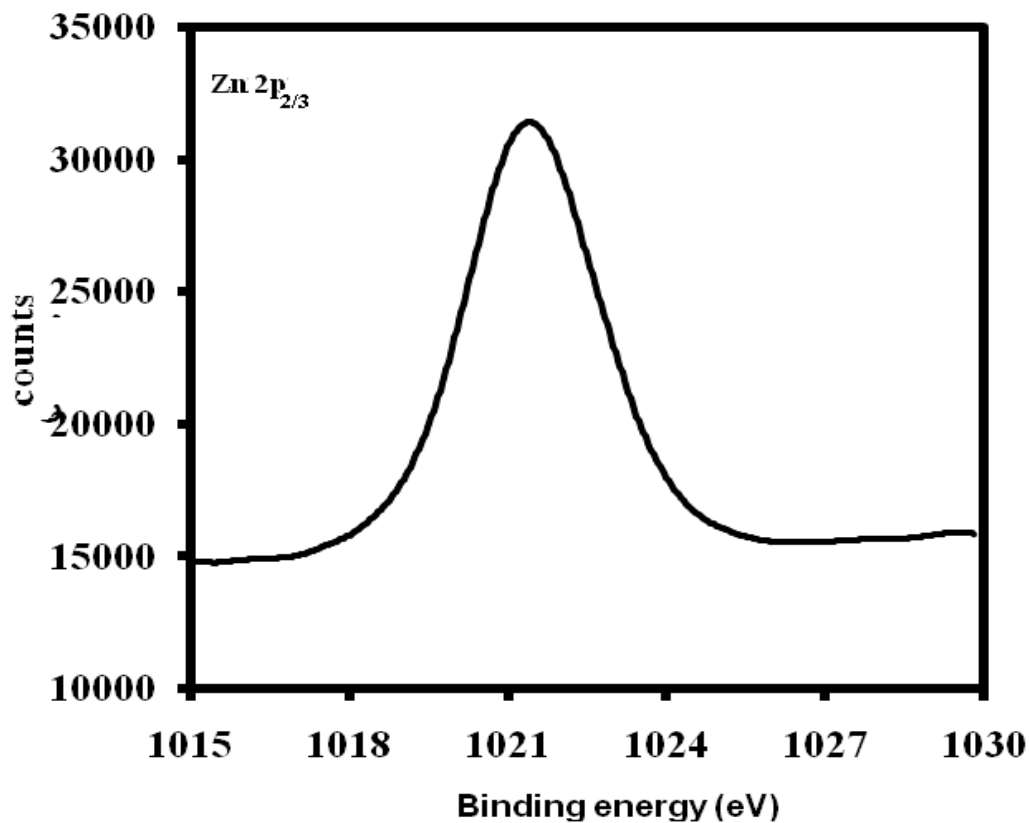
Figure 4-9. The XPS spectrum of Zn2p$_{2/3}$ for ZnO nanoparticles prepared by PLA method.

The optical absorbance of the deionized water solution containing ZnO nanoparticles was measured in the wavelength between 200 nm to 700 nm at room temperature using spectrophotometer (Model a JASCOV–570). In order to record UV spectrum, two quartz cells with 1 cm path length were filled with 3 ml deionized water and base line correction was carried out. One of the cells was kept as a reference and the deionized water solution containing ZnO nanoparticles was kept in the other cell. Fig. (4-10) shows UV-visible spectrum of colloidal solution obtained by pulsed laser ablation

of zinc in deionized water. The ZnO absorption peak at 350 nm (3.37 eV) is blue shifted

relative to the bulk exciton absorption (at 380 nm) for nano ZnO. This blue shift

indicates the quantum confinement property of nanoparticles. In the quantum

confinement rang, the band gap of the particle increases resulting in the shift of

absorption edge to lower wavelength as the particle size decreases. This shift is firmly

verified by the theory of quantum confinement that can be described with the Brus

formula [76]:

$$E_r = E_g^{bulk} + \frac{\hbar^2 \pi^2}{2r^2}\left(\frac{1}{m_e}+\frac{1}{m_h}\right) - \frac{1.8}{4\pi\varepsilon\varepsilon_0 r}e^2 - \frac{\hbar^2\pi^2}{\hbar^2(4\pi\varepsilon\varepsilon_0 r)^2}\left(\frac{1}{m_e}+\frac{1}{m_h}\right)^{-1} \qquad (3)$$

where $E_g{}^{bulk}$ is the bulk semiconductor band gap energy, E_g is the absorption band

gap of nano-semiconductor particles, r is the particle radius, m_e is the effective mass of

the electrons = 0.24 m_0, m_h is the effective mass of the holes = 0.45 m_0, ε is the relative

permittivity = 3.7, ε_0 is the permittivity of free space, h is Planck's constant, and e is the

magnitude of the charge of the electron.
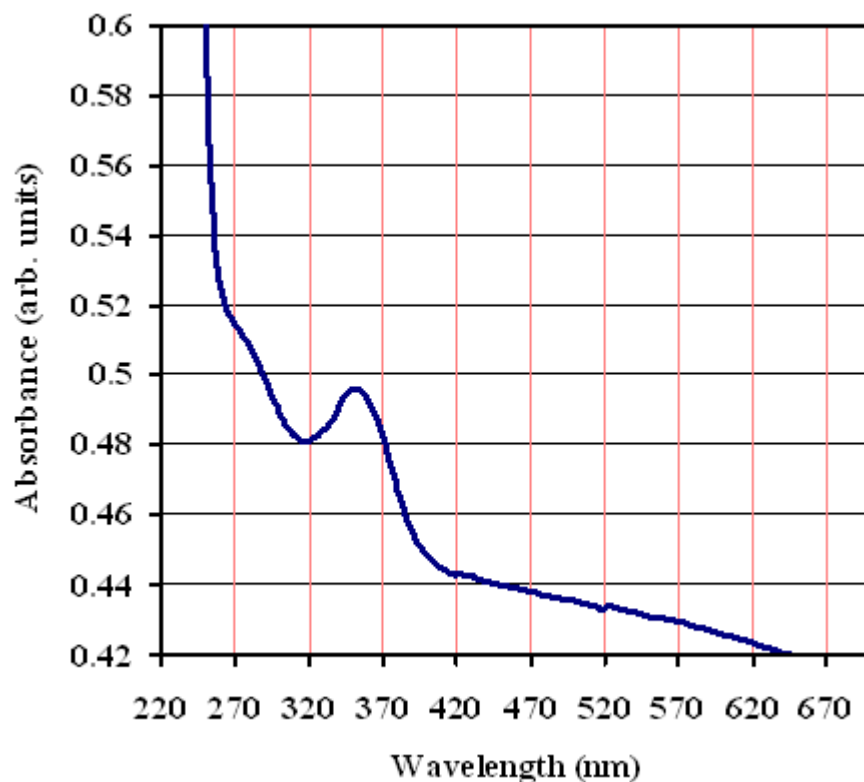
Figure 4-10. UV-Visible absorption spectrum of ZnO nanoparticles colloidal solution obtained by PLA of zinc in deionized water.

The Fluorescence spectra of suspended ZnO nanoparticles prepared by PLA of zinc in deionized water were measured in the wavelength ranging from 200-800 nm. The typical PL spectrum excited at 330 nm wavelength for ZnO nanoparticles prepared by PLA is illustrated in Fig. 4-11. There are two bands of luminescent peaks in the spectra. One band, ranging from 355 to 395 nm and centering at 375nm (3.31 eV), is located in the range of UV and violet light and interpretation due to the recombination of electron hole in semiconductors. A weak band in violet luminescence spectrum is centered at 420 nm (2.95 eV) which is due to the effect of Zn defects [78]. It is worth mentioning that

Violet photoluminescence band at 425 nm (2.92 eV) has been also observed by Zeng et al. [79] from Zn/ZnO core shell nano particles and these bands were sensitive to the shell thickness and annealing conditions. Based on the electron paramagnetic resonance measurements, the violet emission was attributed to the electronic transition from a defect level, corresponding to high concentration of zinc interstitials to the valence band. However Wang et al. observed violet PL at 402 nm from ZnO films deposited by RF magenetron sputtering and attributed it to the electronic transition from conduction band tail states to valence band tail states [80]. There is no visible luminescence emission peaks located in blue, green and yellow region which indicates that purity of ZnO is high.
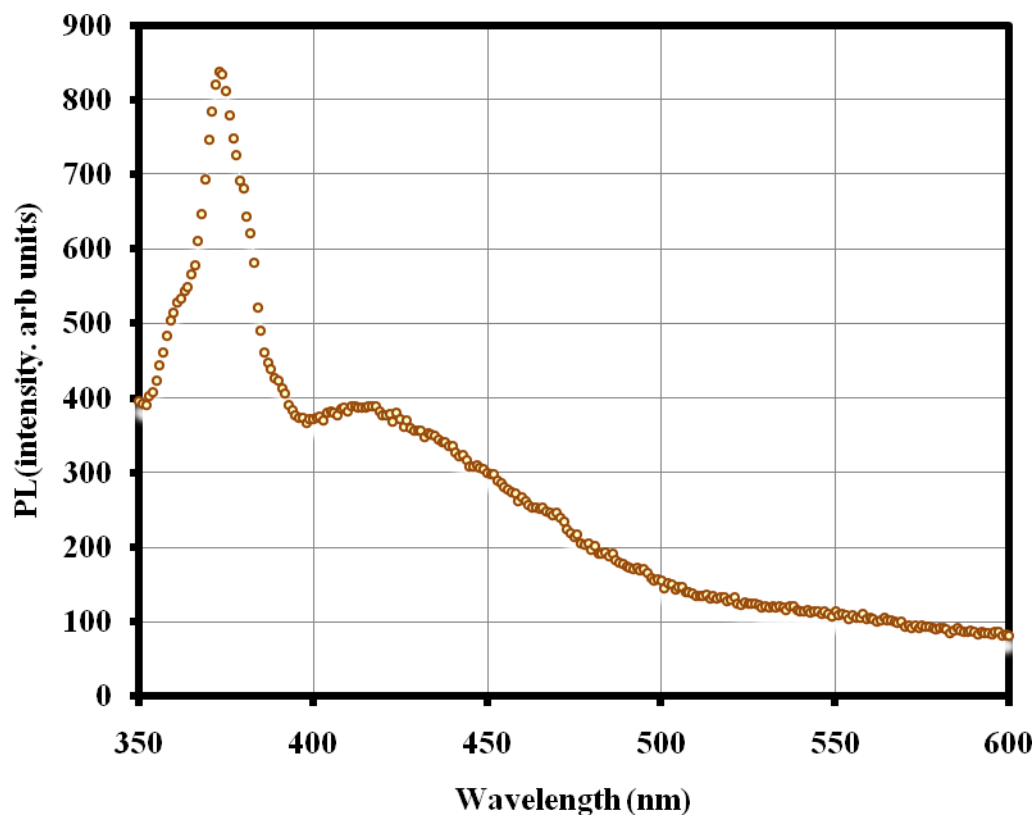
Figure 4-11. Flourescence emission spectra for ZnO nanoparticles synthesized by PLA in water.

In order to confirm selected excitation wavelength which is equal 330 nm, the emission was fixed at 375 nm and then excition spectrum was recorded. Figure 4-12 shows an excitation peak at 330 nm. This means that exciting ZnO nanoparticles at this wavelength should give rise to the emission at 375 nm which agrees well with our fluorescence emission spectrum.
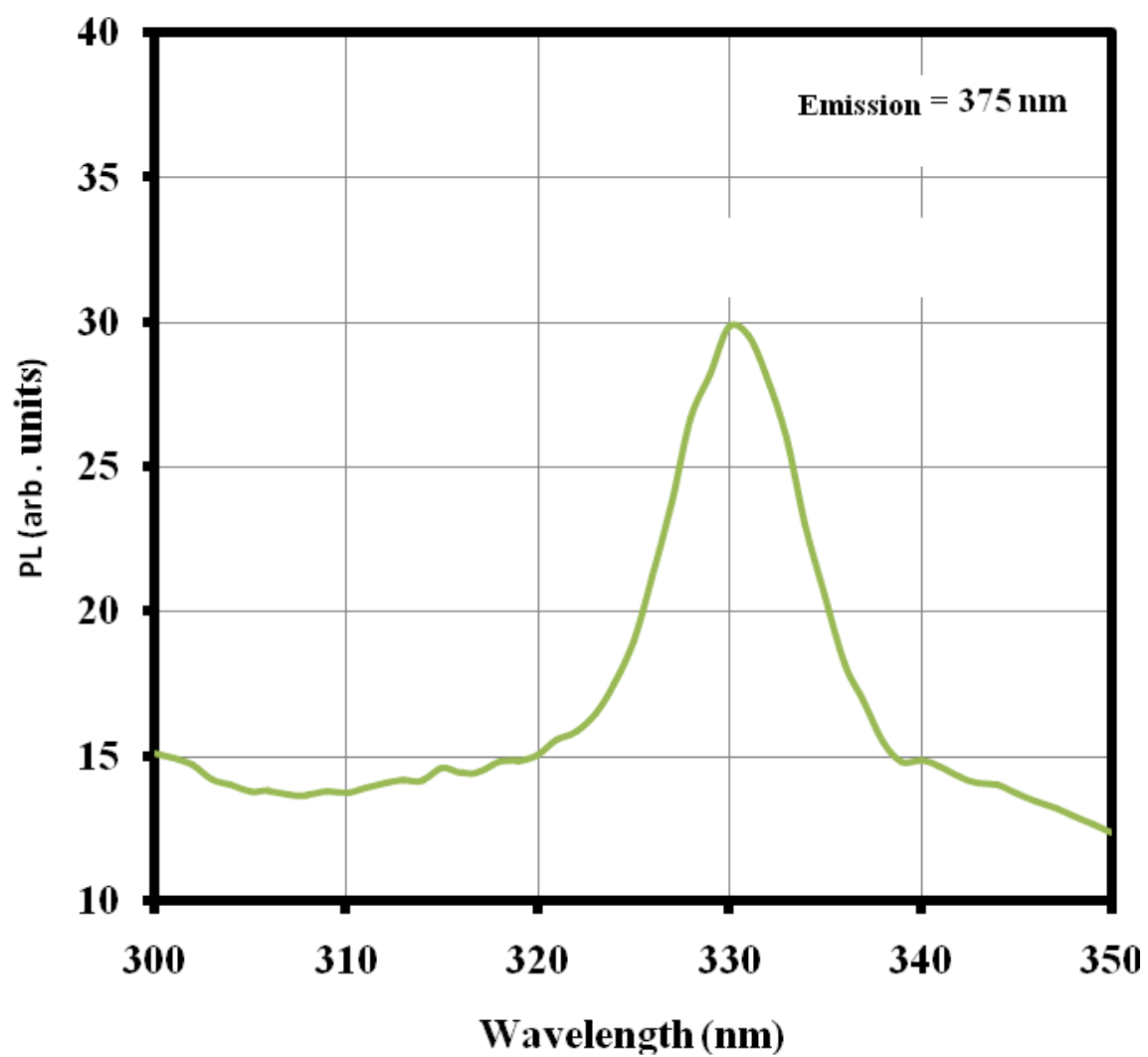
Figure 4-12. Fluorescence excition spectra for ZnO nanoparticles synthesized by PLA in water.

4.2. EFFECT OF SURFACTANTS ON THE PROPERTIES OF ZnO NANOPARTICLES

Surfactants (surface acting agent) are wetting agents that lower the surface tension of a liquid, allowing easier spreading, and lower the interfacial tension between two liquids by adsorbing at the liquid-gas interface. Many surfactants can also assemble in the bulk solution into aggregates. Examples of such aggregates are vesicles and micelles. Figure (4-12) shows typical XRD spectra of ZnO formed in presence of two different surfactants namely: CTAB and OGM with concentration close to their critical micelles concentration (CMC) which corresponds 9.1×10^{-4} and 1.2×10^{-3} M in CTAB and OGM respectively. As is clear from figure 4-13, all peaks are assigned to the typical pattern of wurtzite hexagonal structure ZnO in the case of CTAB and OGM implying that the products are pure ZnO. Hiroyuki et al. [81] reported that the ablation of zinc in deionized water with the presence of SDS will form layered ZnDS nanoparticles which indicate that there is an interaction between zinc oxide and SDS under laser beam radiation. The grain size and the lattice parameters of the products were calculated and are listed in the table (4-4).
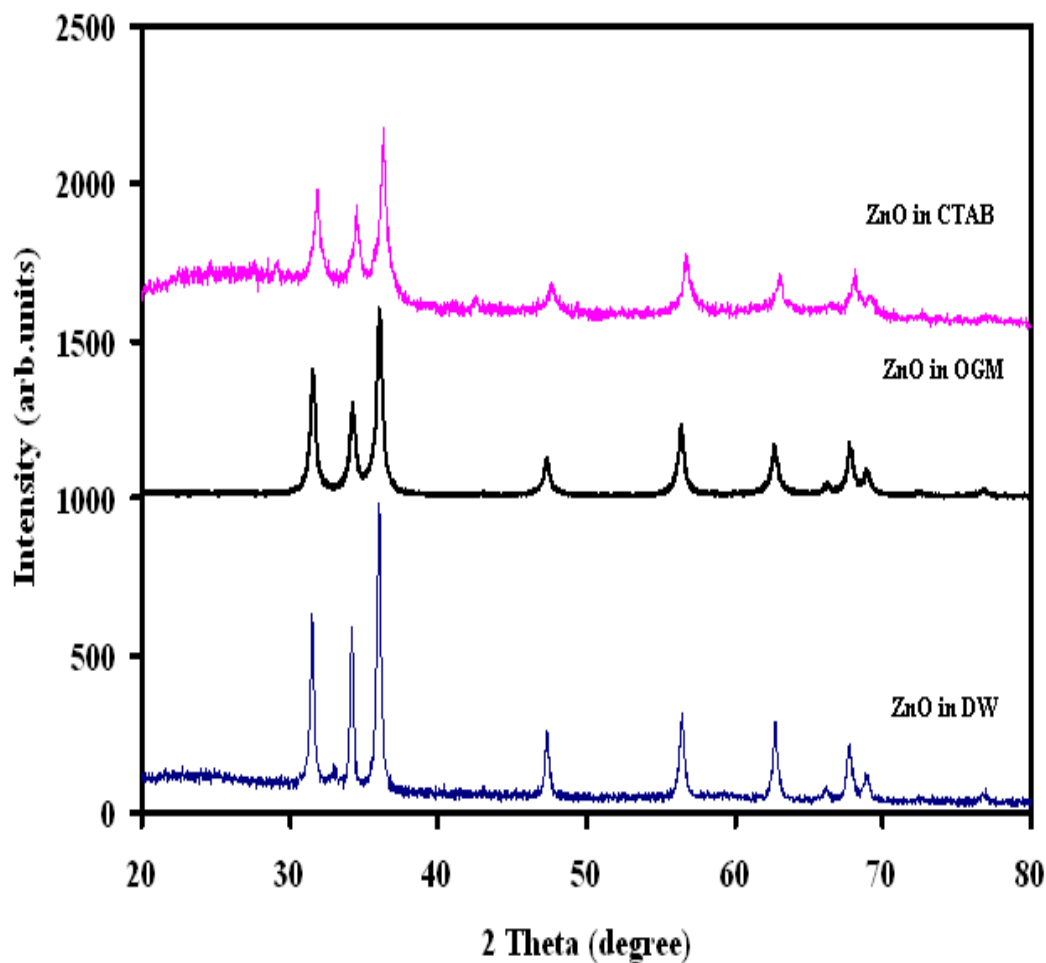
Figure 4-13. XRD patterns of the ZnO nanoparticles obtained by PLA in pure water, CTAB and OGM solutions.

According to the XRD spectra and table (4.4), the average diameter of ZnO nanoparticles decreases with the change of the nature of surfactants. The grain size was 38 nm in pure deionized water then decrees to 27 and 19 nm in the case of CTAB and OGM respectively. The polar head of the surfactant plays a vital role to understand the physical processes in decreases of the grain size, as it was mention in chapter 1

surfactants have two heads: polar and non-polar and at a certain concentration called "critical micelles concentration" (CMC) surfactants start to form micelles. These micelles will surround ZnO as shown in figure (4-14). The electric attractive force between ZnO nanoparticles and the polar head of the micelles molecules, and the formation of micelles is assumed to prevent the aggregation and growth of ZnO nanoparticles. ZnO nanoparticles possibly have a positive electric charge in the solutions because the isoelectric point of ZnO is 9.5 in aqueous solutions [82].

OGM has a local weak negative charge at the oxygen atom, $C1_2H_{25}(O^{\sigma-}CH_2CH_2)_8OH$, and ZnO has a positive charge. Therefore, the OGM molecules surround ZnO nanoparticles due to the electric attractive force between ZnO nanoparticles and the molecules, and the formation of micelles is supposed to prevent the aggregation and growth of ZnO nanoparticles. This probably leads to smaller nanoparticle sizes in the case of OGM solutions.
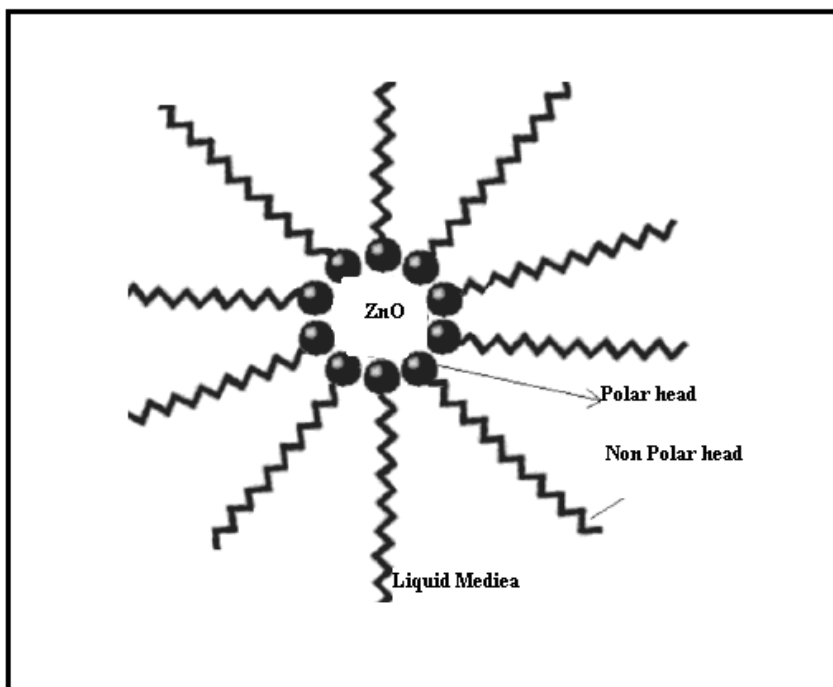
Figure 4-14. Scheme of capping of surfactants (CTAB and OGM) on the surface of ZnO nanoparticles.

Table 4-4 Lattice parameters and grain sizes of ZnO nanoparticles prepared by PLA in surfactants.

DW +	Concentration of surfactants (M)	Grain size (nm)	Lattice parameter a (°A)	Lattice parameter c (°A)
0	0	38	3.257	5.210
CTAB	9×10^{-4}	27	3.212	5.253
OGM	8.1×10^{-3}	19	3.291	5.251

PL is a sensitive technique for examining the purity of ZnO. Figure (4-15) depicts typical PL spectra of ZnO colloidal suspension obtained at room temperature in deionized water, CTAB and OGM. As seen, the sharp UV emission peaks at 372 nm in the case of pure water whereas these peaks shift to longer wavelength in other surfactants (almost 380 nm). In addition, there is a broad peak in the visible range (450-600) nm in the case of CTAB and OGM which possibly due to impurities surfactants.
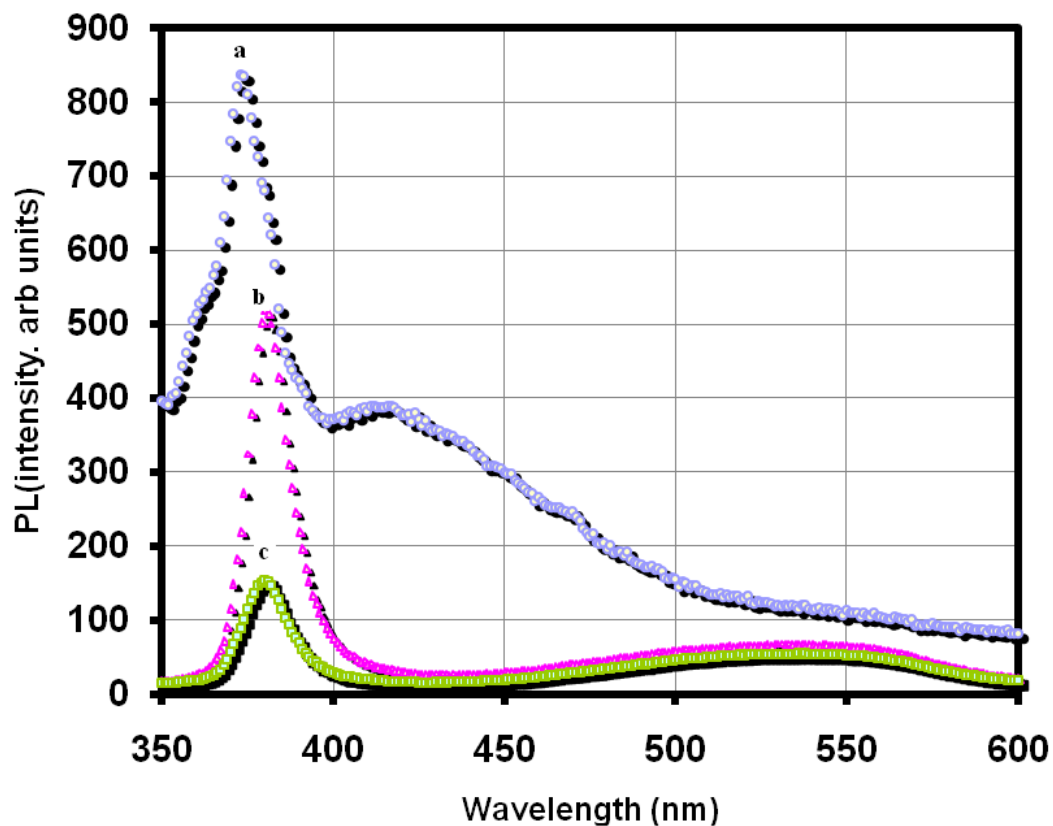
Figure 4-15. PL emission spectra of nanoparticles ZnO obtained at   a) pure deionized water b) CTAB and c) OGM surfactants (at excitation 320 nm).

4.3. SYNTHESIS AND CHARACTERIZATION OF ZnO_2 NANOPARTICLES

Zinc peroxide ZnO_2 is an n semiconductor material with band gap energy 3.8 eV. It has cubic crystalline structure with the lattice parameter a= 4.817 °A [83]. ZnO_2 has many applications such as: Photocatalysis [84], rubber technology [85], therapeutic and to prepare ZnO [86,87].

In fact, there are not many studies for synthesis of ZnO_2. In this work, ZnO_2 nanoparticles were prepared by laser ablation of pure Zn in presence of 3% H_2O_2 for the first time. It has been reported that the formation of ZnO_2 results from the photochemical reaction of H_2O_2 in high concentration (30%) and $Zn(CH_3COO_2)_2$, and the corresponding process is considered as following [89]:

$Zn (CH_3COO_2)_2 + H_2O_2$ ------- $ZnO + 2HCH_3COO_2$
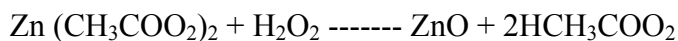
While in our case we do not need any precursor like $Zn (CH_3COO_2)_2$ and the formation of ZnO_2 by laser ablation of pure Zn in presence of relatively low concentration H_2O_2 (3%) has been achieved.

To synthesis ZnO_2 nanoparticles by PLA in liquid, a schematic diagram of the laser based setup for synthesis of nano particles is depicted in Fig. 4-1. A Q-switched Nd-YAG laser (Spectra physics Model GCR 100) operating at 355 nm wavelength using third harmonic generator was employed as an excitation source. It can deliver maximum

pulse energy of 300 mJ with a pulse width of 8 ns and operates at a 10 Hz pulse repetition rate. The collimated beam at 355 nm is tightly focused on the target sample using a convex lens to create a spark or breakdown in the sample. In this experiment, we placed a 2 mm diameter aperture inside the path of laser beam in order to get a uniform beam shape. For the synthesis of nano particles of these particles, a high-purity metallic plate of Zn (99.99 % Aldrich Company) is fixed at the bottom of a glass cell as the target, and is rotated to avoid a deep ablation traces or crusts. Typical laser pulse energy for PLA process was 130 mJ per pulse. The laser beam was focused by a lens with a focal length of 250 mm in order to get sufficient laser fluence for the ablation. The typical diameter of the laser spot on a bulk target was ~ 0.08 mm and the typical 3 % H_2O_2 volume was 10 ml. After laser irradiation for 60 min, a milky colloidal solution of peroxide-based nano materials was obtained. The colloidal suspension was separated from the solution using centrifuge and, in the case of surfactants was washed several times with deionized water. The precipitate was collected and then dried in an oven at 90 ºC for 1 hour.

A variety of analytical techniques were applied for the characterization of products. (XRD) were employed to determine crystalline phases and average crystalline size. Photoluminescence spectra were studied to measure the optical properties of the products while UV-Vis Spectroscopy was used to record the UV-Vis absorption spectra.

To explain the change of the material from ZnO to ZnO_2, the following chemical reactions are suggested for the fabrication of ZnO and ZnO_2 during the laser irradiation process.

$H_2O + h\nu$ (laser at 355 nm) $\rightarrow H^+ + OH^-$

$OH^- + h\nu$ (laser at 355 nm) $\rightarrow O* + H*$

$Zn + O \rightarrow ZnO$

By addition of H_2O_2

$Zn + H_2O_2 \rightarrow Zn\,(OH)_2$

$Zn\,(OH)_2 \rightarrow ZnO + H_2O$
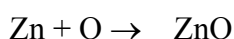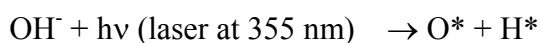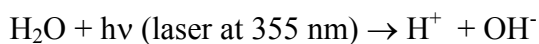
$ZnO + O \rightarrow ZnO_2$
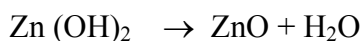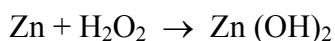
Since H_2O_2 is a strong oxidizing agent so it generates more oxygen and thus triggers the process of conversion of ZnO into ZnO_2. It is worth mentioning that ZnO_2 generation has been achieved for the first time using laser ablation process.

In order to investigate the crystal structure of the ZnO_2 nanoparticles, XRD was carried out from 20° to 80° (Fig 4-16). The XRD spectrum of ZnO_2 prepared by PLA in 3 % H_2O_2 clearly shows the ZnO_2 crystalline structure of the nanoparticles and various peaks of zinc peroxide (ZnO2). The main dominant peaks for ZnO_2 were identified at 2θ = 31.6^o, 36.8^o, 53.14^o and 63.2^o respectively which correspond indexes (111), (200), (220) and (311). Figure (4-16) shows the structure of products prepared in deionized water and 3% H_2O_2. It is clear from the position of the peaks in both cases that the phase

of the material is changed from hexagonal structure to face center cube (fcc). The lattice

parameter a of the ZnO_2 was estimated from the formula of the cubic structure [12]:

$$a = \frac{\lambda}{2\sin\theta}\sqrt{h^2 + k^2 + l^2}$$

Where λ is the wavelength of the X-ray, hkl are miller indices and θ is the

diffraction angle.
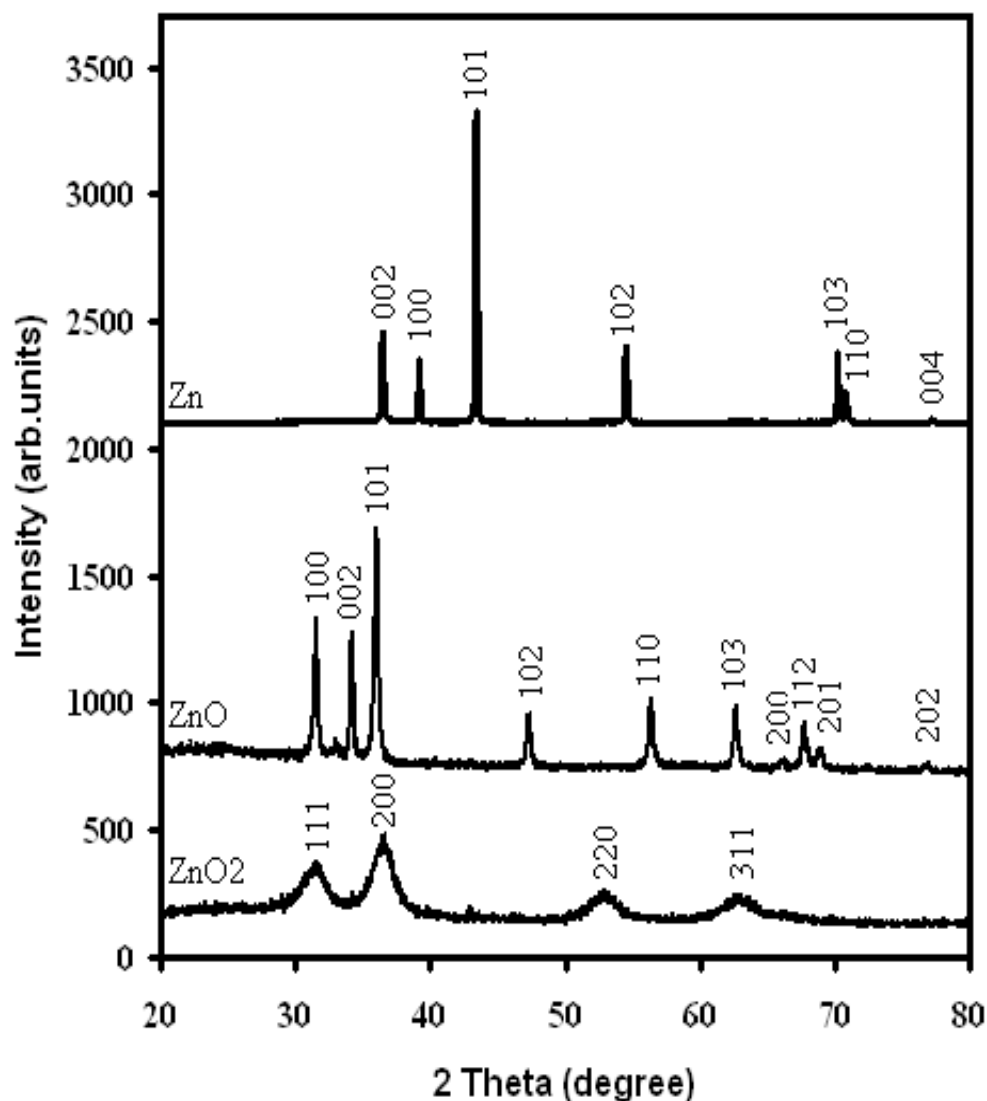
Figure 4-16. XRD for Zn (bulk); ZnO and ZnO₂ nanoparticles obtained by PLA method at deionized water and 3% H₂O₂ respectively.

The average size of ZnO_2 nanoparticles calculated at angle 36.4 $^{\circ}$ is 4 nm. The lattice parameter is 4.8820 $^{\circ}$A and this value of lattice parameter is greater than the values reported in [89-90] which is 4.817 $^{\circ}$A. This increase can be attributed to the decrease in the grain size. This lattice expansion dependence on the size has also been

reported for different materials such as: MgO, ZrO_2 and Pd [91-93]. Many scientists have suggested that this expansion of the lattice parameters can be attributed to the special atomistic structure and number of grain boundaries [94]. The average size of these particles was also confirmed using the standard method such as AFM. The grain size distribution, measured by AFM image is depicted in Figure 4-18. This is clear indication that laser ablation process is an efficient method for production of nano structured ZnO_2.
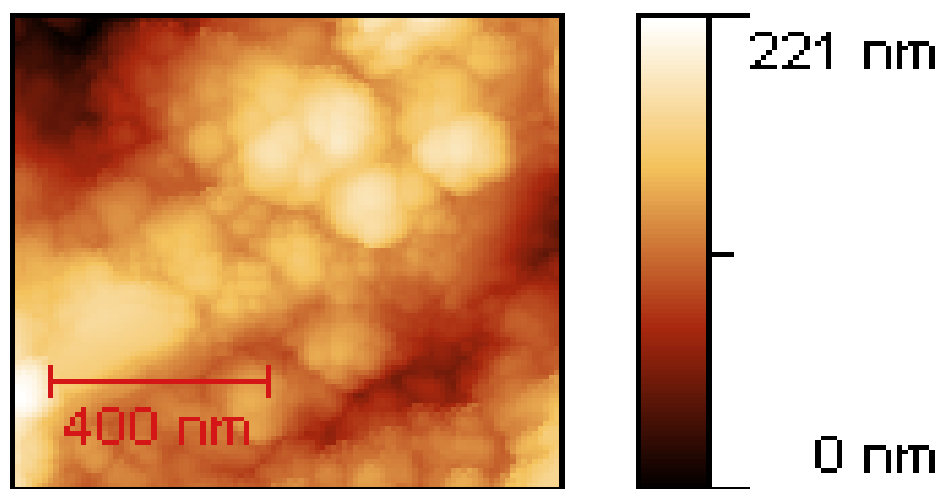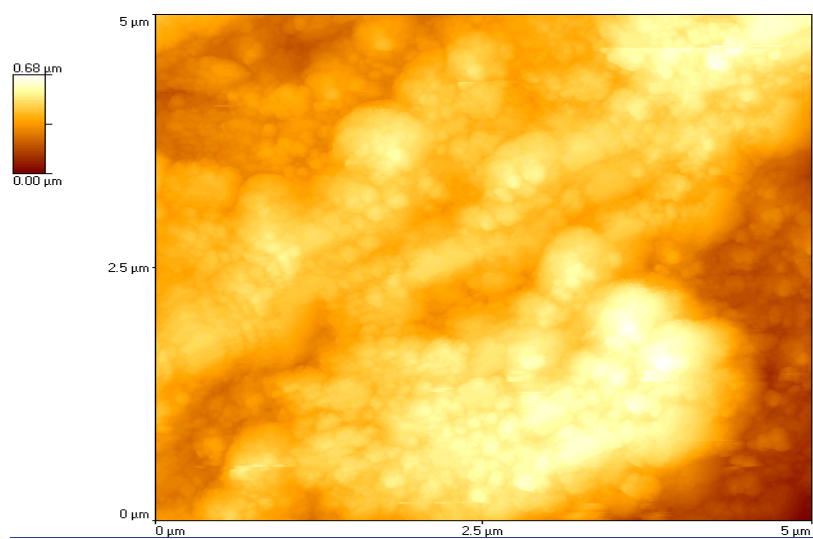
Figure 4-17. A typical AFM images of ZnO$_2$ nanoparticles.
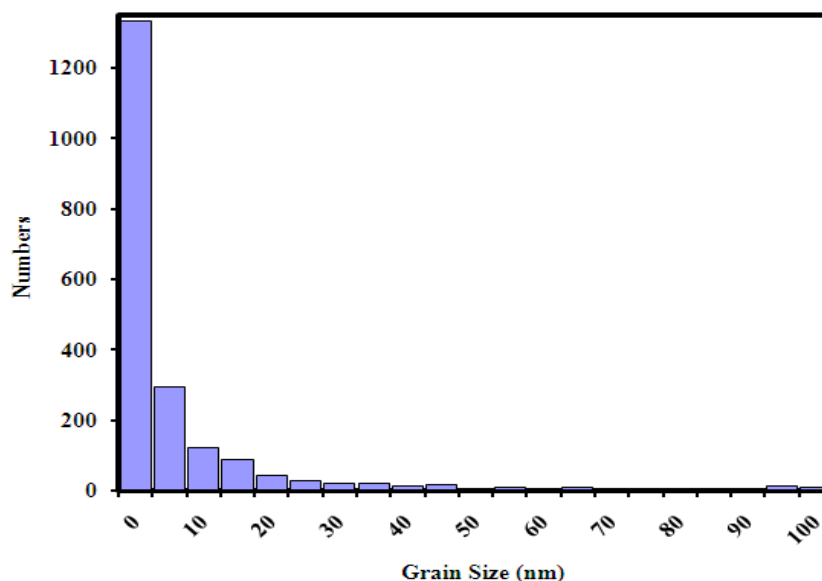
Figure 4-18. Size distribution plot for Zinc peroxide prepared with 6% H_2O_2 in 25 μ^2 area estimated from AFM analysis.

In order to investigate the quality and purity of products, the fluorescence spectrum of suspended ZnO_2 nanoparticles prepared by PLA of zinc in 3 % H_2O_2 was measured in the wavelength ranging from 200-800 nm. The typical PL spectrum excited by 250 nm for ZnO_2 nanoparticles is illustrated in Figure (4-19). To the best of our knowledge there are no PL studies of pure ZnO_2 available. The fitting of the peaks shows four peaks centering at 456, 369, 352 and 334 nm and the strongest emission peak occurs at 369 nm (3.35 eV) which is probably due to radiative recombination of the surface of ZnO_2 particles. Abroad blue light (456 nm) emission can be attributed to oxygen vacancies and other week peaks might occur due to other defects.
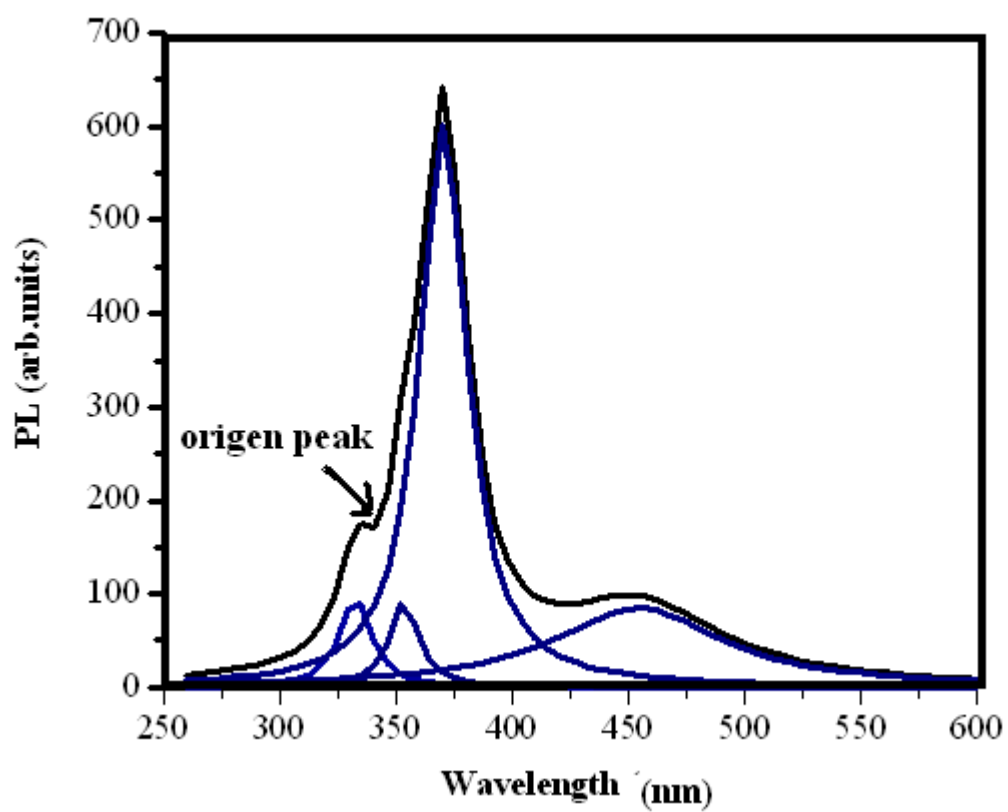
Figure 4-19. Photoluminescence emission spectra fitting of ZnO$_2$ nanoparticles prepared by means of PLA.

4.4. EFFECT OF LASER POWER ON PRODUCTION YIELD

The dependence of ZnO/ ZnO$_2$ nanoparticles production yield on incident laser energy is depicted in Fig. (4-20). In order to investigate the effect of laser energy on production, the laser irradiation energy was fixed at 100 mJ (λ= 355 nm). The laser energy was measured with a calibrated energy meter (Ophir model 300) while laser irradiation time was kept constant at 40 minutes. The rise in production yield could be explained as follows.

With rise in laser energy, the number of incident photon increases and thus the amount of ablated material also increases which could contribute to enhancement of ZnO and ZnO$_2$ yield.
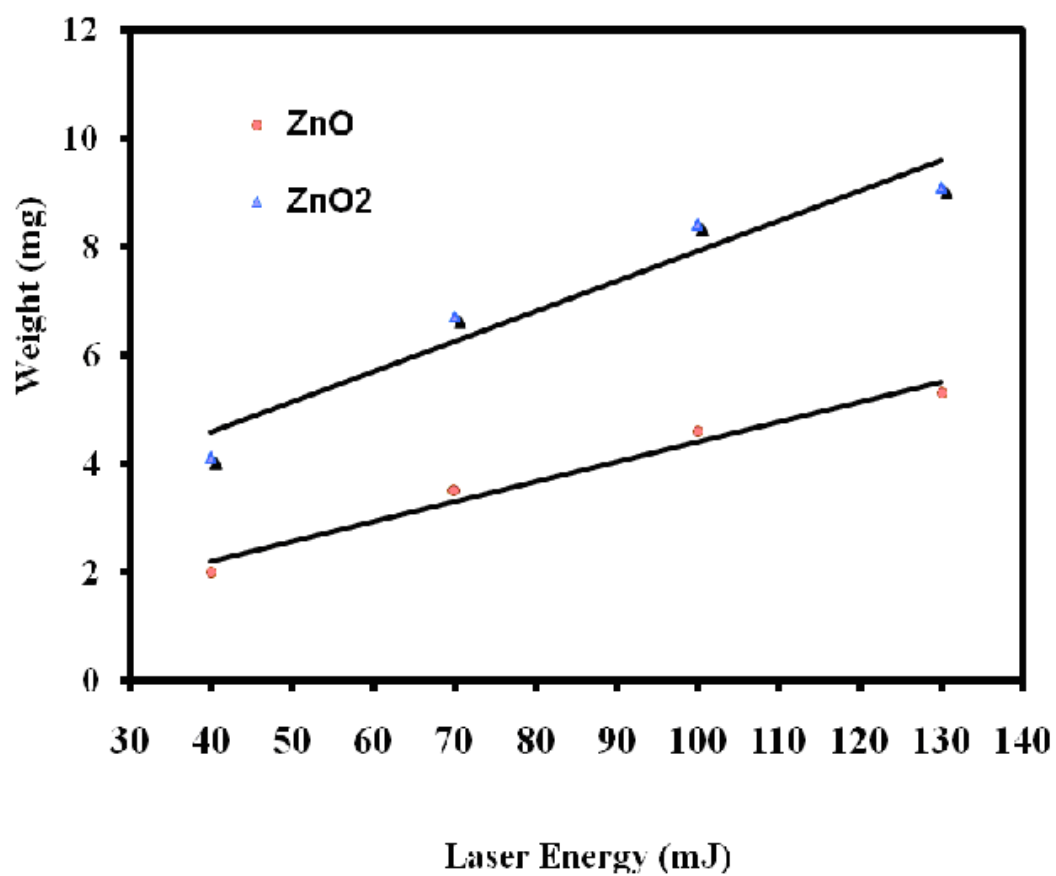
Figure 4-20. Dependence of mass of the synthesized ZnO₂ and ZnO on incident laser energy for a duration of 40 minutes.

4.5. EFFECT OF SURFACTANTS ON THE PROPERTIES

OF ZnO$_2$

In order to investigate the effect of surfactants on the structure, grain size and other properties, SDS, CTAB and OGM surfactants were prepared at critical micelles concentration (CMC) and then were used as ablation media. After 60 minutes irradiation, products were collected by centrifuge. XRD, FTIR, UV-Vis absorption and PL were carried out to characterize the product.

Figure 4-21 shows the XRD spectra of the ZnO$_2$ nanoparticles synthesized in 3 % H$_2$O$_2$, SDS, CTAB and OGM surfactants using the PLA method. Here the laser energy was kept at 100 mJ and the laser irradiation time was 45 minutes. The XRD spectrum as presented in Figure 4-20 clearly shows the crystalline structure of the nanoparticles and various peaks of zinc peroxide (ZnO$_2$). From the XRD spectra, it clear that there are no extra peaks; one can also infer that there is no effect of surfactants on the composition and the structure of the products.

Table (4.6) summarize the grain size and the lattice parameter of ZnO$_2$ prepared by pulsed laser ablation in 3 % H$_2$O$_2$ and different surfactants. As seen in the table, the grain sizes were: 4.7, 3.7, and 3.5 nm in 3% H$_2$O$_2$, SDS, OGM and CTAB respectively. One interpretation of the surfactants role in the synthesis of zinc peroxide nanoparticles is that surfactants control the growth of nanoparticles by preventing their agglomeration. This interpretation is supported by the coating ability of surfactants on the particle

surface forming stable micelles and preventing nanoparticles to get aggregated via columbic repulsion or steric hindrance. On the other hand, the lattice parameter were 4.8820, 4.8549, 4.8781 °A . All these values of lattice parameter of zinc peroxide prepared by PLA in different media were greater then the values reported in [89-90] which was 4.817A.
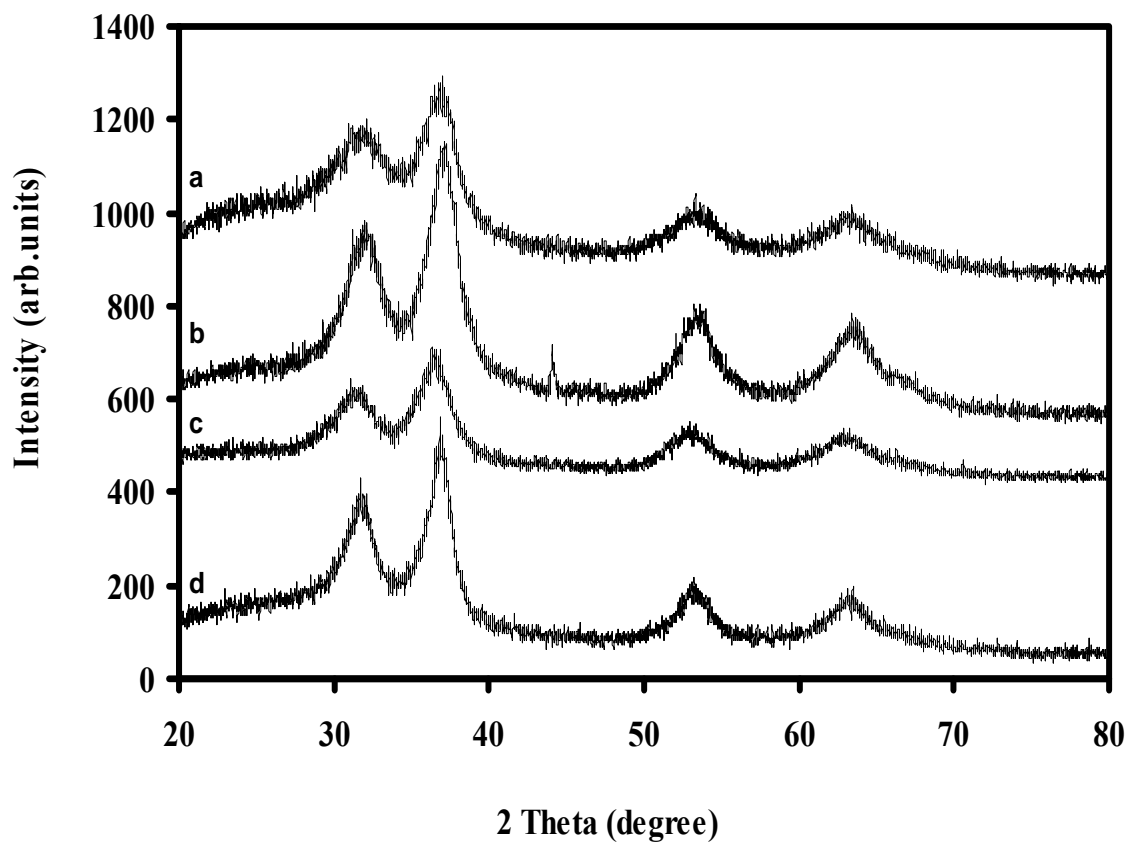
Figure 4-21. XRD spectra of ZnO$_2$ nanoparticles prepared in a) OGM, b) without surfactants c) CTAB and d) SDS for a duration of 40 minutes.

Table 4-5. Grain size and lattice parameter dependence on media ablation.

Solution 3% H_2O_2 +	CMC of surfactants (M)	Grain Size (nm)	Lattice Parameter a (A)	Absorption edge (nm)
SDS	8.1×10^{-3}	4.7	4.8549	314
0	0	3.7	4.882	292
CTAB	9.1×10^{-4}	3.3	4.874	276
OGM	1.1×10^{-4}	2.8	4.8781	259

Figure (4-22) shows PL spectra of ZnO_2 prepared at the same conditions in only hydrogen peroxide and hydrogen peroxide with surfactants, namely SDS and OGM. CTAB, SDS and OGM clearly exhibit shift to higher wavelength centered at 380 nm.
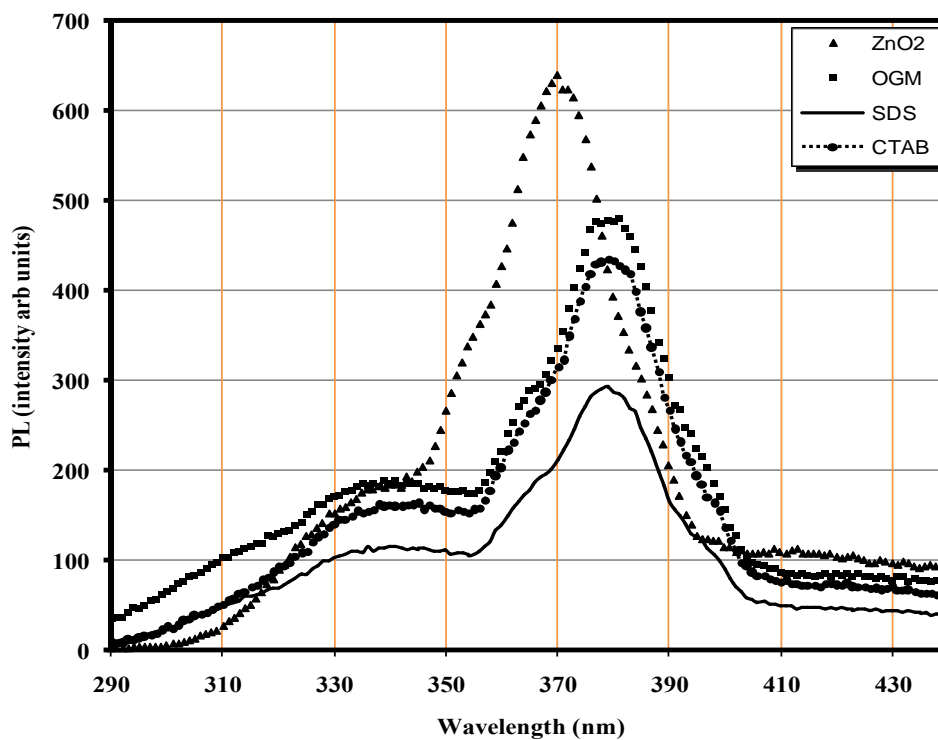
Figure 4-22. Photoluminescence emission spectra of ZnO$_2$ nanoparticles prepared using PLA at different surfactants.

FTIR was used to measure (IR) absorption. In order to study the surfactants effect on synthesis of ZnO$_2$ nanoparticles prepared by pulsed laser ablation in different media, FTIR spectra were measured at room temperature with FTIR spectrometer using the KBr Pellet technique. Samples were lyophilized, gently mixed with 300 mg of KBr powder and compressed into discs at a force of 13 kN for 5 min using a manual tablet presser. FTIR spectra were recorded in the spectral range of 400-4000 cm^{-1}. Figure 4-24 shows

the FTIR spectrum of ZnO_2 nanoparticles prepared in the presence of different surfactants, SDS, CTAB and OGM and in absence of surfactants. The absorption peaks at 3200-3600 cm^{-1} are correlated to the water O-H stretching vibration mode. The bands in the range of 1630-1660 cm^{-1} are due to the OH bending of water. This indicates the presence of small amount of water adsorbed on the nanoparticle surface. Because of the existence of CO_2 molecule in the ambient air, there is absorption peak at around 2360 cm^{-1}. In Fig. 4-24 the spectra show a characteristic ZnO_2 absorption at 435-445 cm^{-1} for the nanoparticles produced in absence and presence of surfactants. There are also other bands at 1040-1070 cm^{-1} present in the spectra which may arise from the O-O bands, which is consistent with that reported in literature [95]. Although, the synthesized nanoparticles were extensively washed, comparison between FTIR transmittance spectra of ZnO_2 nanoparticles prepared in absence of surfactants and presence of surfactants shows that there are some peaks in case of SDS which lead to probability of presence of DS coated on the surface of the prepared nanoparticles. Comparing the FTIR transmittance spectrum of ZnO_2 prepared in SDS (Fig. 4-24) with the FTIR transmittance spectrum of pure SDS (Fig. 4-24), reflects the presence of some peaks related to DS. Two peaks at 2917 and 2848 cm^{-1} are due to the symmetric stretching of CH_2 presented in DS. Transmittance peaks at 1337, 1230 and 1078 cm^{-1} are assigned as CH_3 bending, CH_2 bending and C–C stretching modes of DS, respectively. These five peaks which appear in FTIR spectrum of pure SDS also appearing in ZnO_2 nanoparticles prepared in SDS-containing solution. In case of CTAB and OGM, these peaks disappear.

In general, the surfactants effect can clearly be observed from FTIR spectra. It is worth noting that SDS causes red shift while the CTAB and OGM cause blue shift.
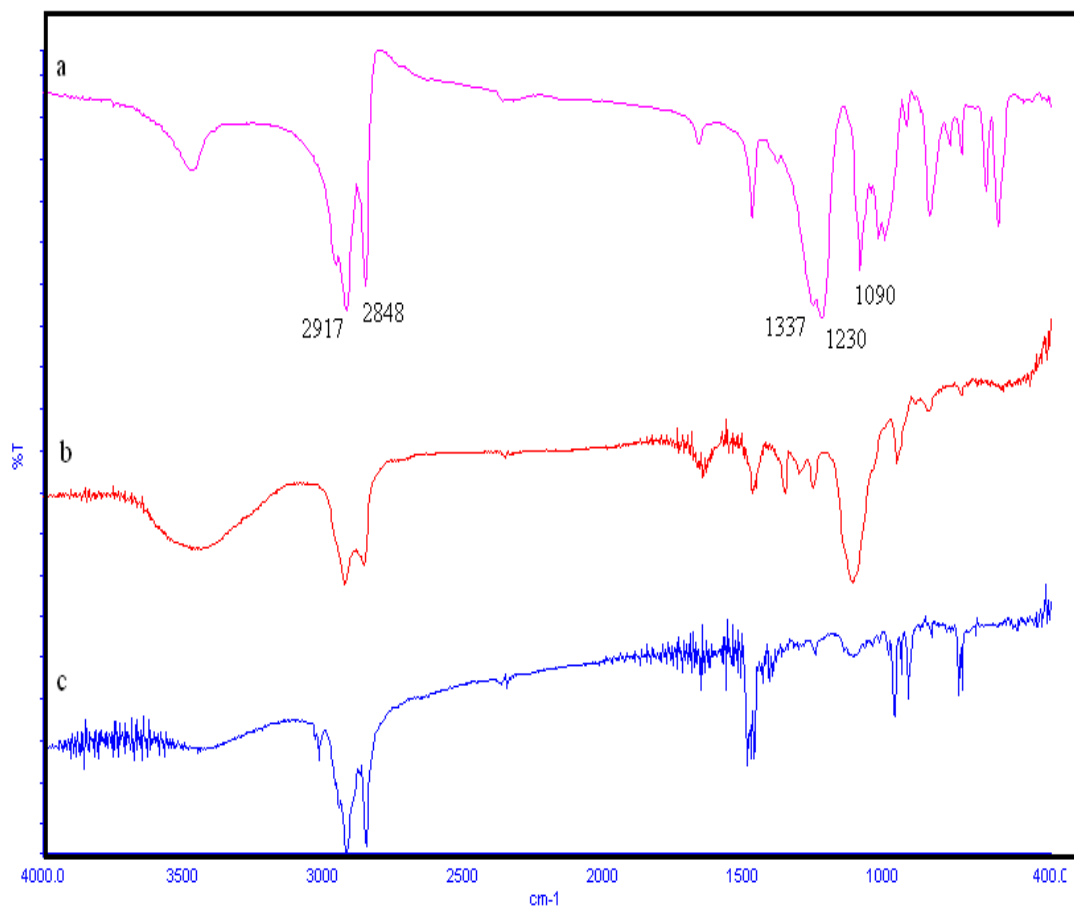
Figure 4-23. FTIR spectra of pure surfactants: a) SDS b) OGM and c) CTAB.

.
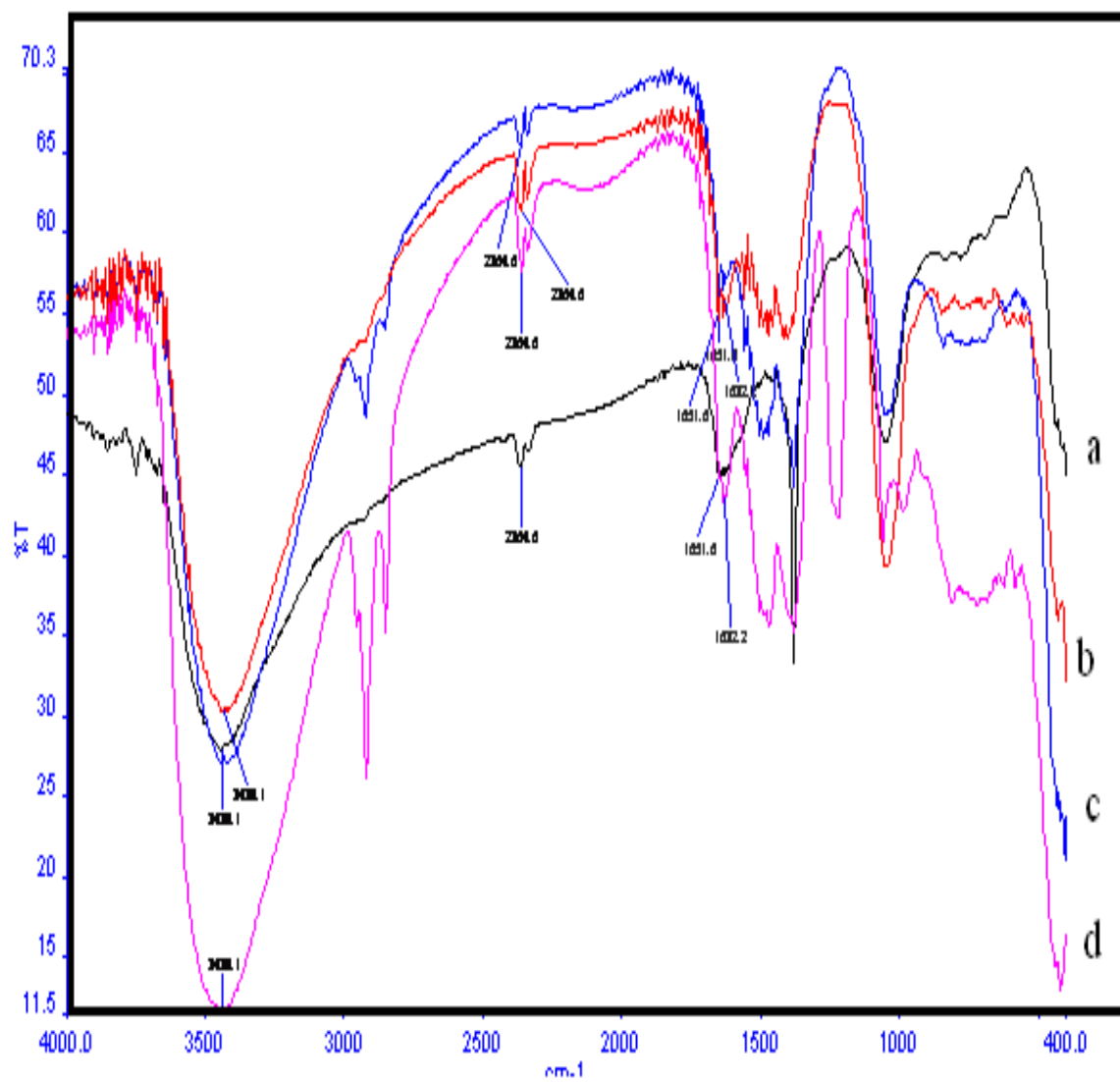
Figure 4-24. FTIR spectra of ZnO$_2$ nanoparticles prepared: a) free of surfactants b) in presence of OGM, c) in presence of CTAB (Blue line); and d) in presence of SDS.
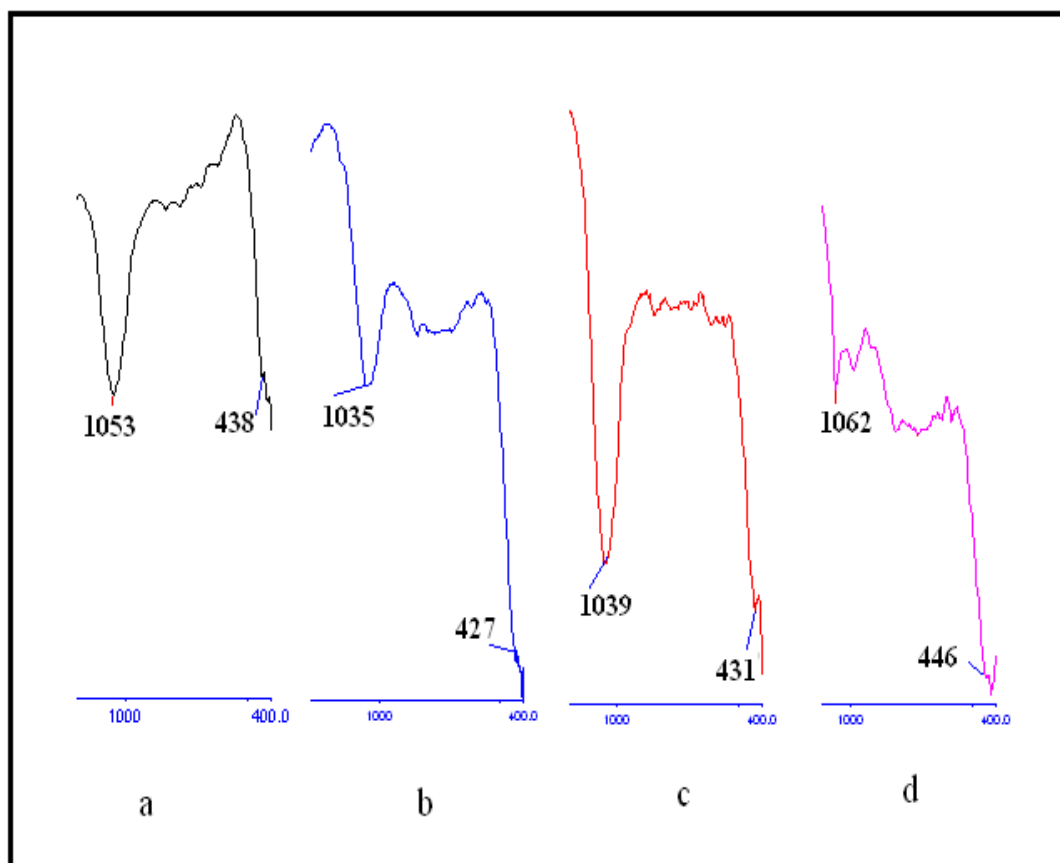
Figure 4-25. Enlarged FTIR spectra in the region 425–450 cm−1 for the tested ZnO₂ nanoparticles samples prepared: a) with additive-free, b) in presence of CTAB, c) in presence of OGM, d) and in presence of SDS.

The optical absorbance of suspended ZnO_2 nanoparticles prepared by PLA in 3 % H_2O_2 was measured in the 200 nm to 600 nm wavelength range. Prior to the measurements of UV-Vis absorption, the hydrogen peroxide solution which has a strong UV absorption was removed completely and an equal amount of powder samples were uniformly and gently dispersed in another solvent. The UV-Vis absorption spectra of the ZnO_2 nanoparticles at room temperature are depicted in Fig. 4-26. The band position of

zinc peroxide prepared in absence of surfactants at around 280 nm corresponds to ZnO_2 nanoparticles. SDS cause shift of the band to almost 320 nm (red shift) which occurs for aggregated nanoparticles. On the other hand opposite shift (blue shift) was caused by the other surfactants (see the values of absorption edge in table 4-5). This blue shift indicates the quantum confinement property of nanoparticles. In the quantum confinement rang, the band gap of the particle increases resulting in the shift of absorption edge to lower wavelength, as the particle size decreases. This shift observed in our work firmly testifies the theory of quantum confinement effect that can be described with the Brus formula [76].
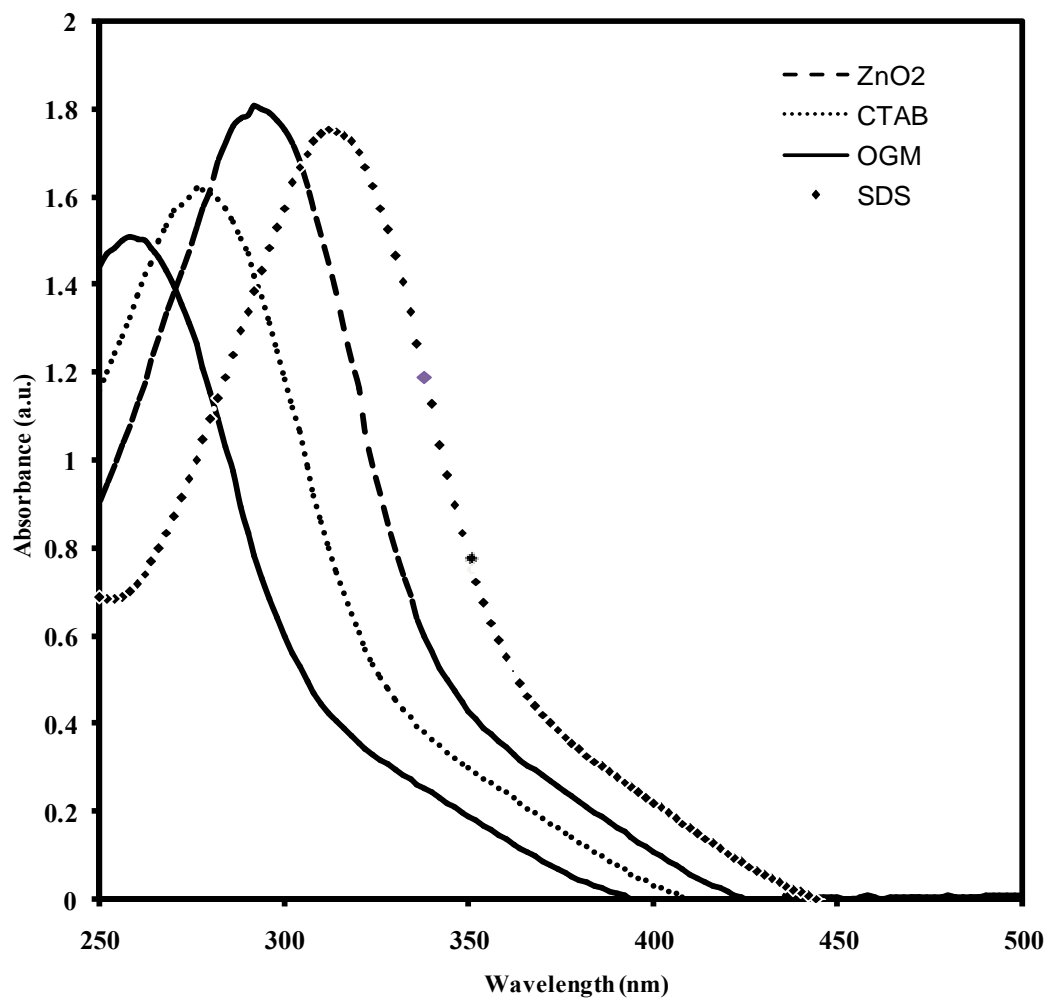
Figure 4-26. UV-Vis absorption spectra of ZnO₂ nanoparticles prepared: with additive-free and in presence of CTAB, OGM and SDS.

4.6. EFFECT OF THE ANNEALING TEMPERATURE ON

ZnO$_2$ NANOPARTICLES

In order to study the effect of annealing temperature on the structure and optical properties of ZnO$_2$ prepared by PLA in 3 % H$_2$O$_2$, synthesized powder was kept in oven at different temperature. Different techniques were used to characterize these samples namely XRD, FTIR, UV-Visible spectrometer and fluorescence spectroscopy.
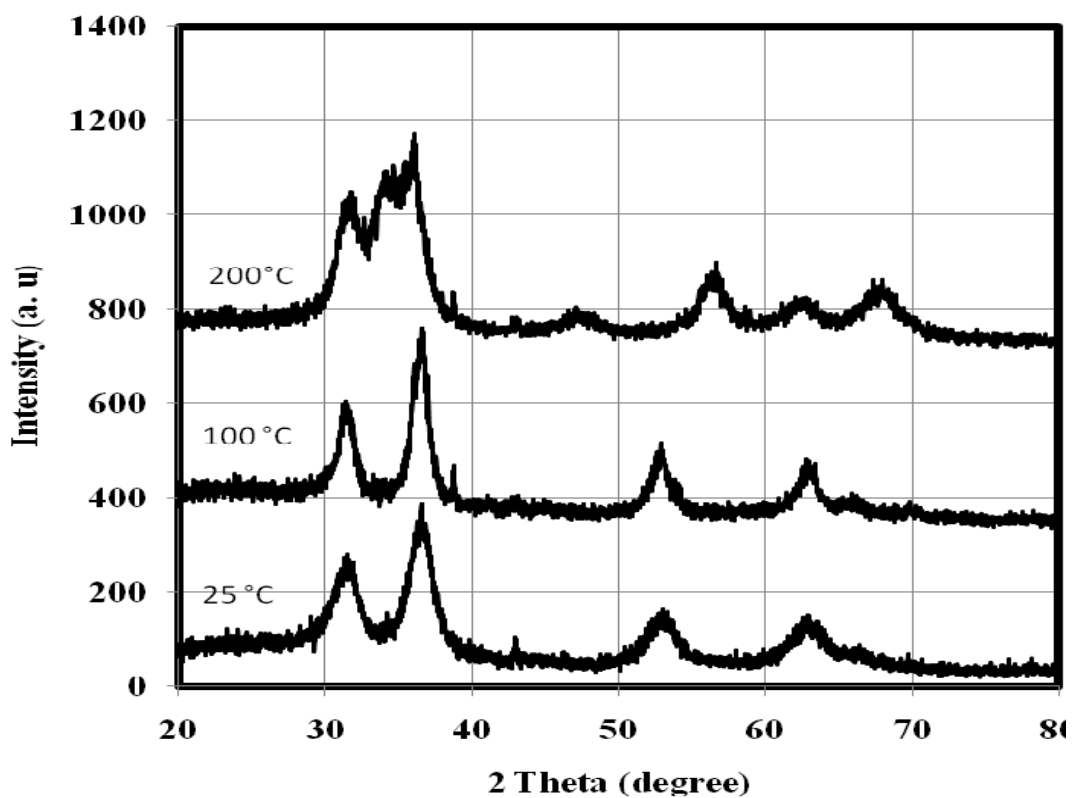
Figure 4-27. XRD spectrum of ZnO$_2$ and ZnO prepared by PLA by post annealing

tepmerature (25, 100 and 200) °C

The XRD spectra as presented in Figure 4-29 clearly show the phase transition at nearly 200 °C from ZnO_2 to ZnO phase. The transition from ZnO_2 to ZnO at 180°C by means of TGA techniques was reported in reference [89].

In order to investigate the effect of post-annealing effect on ZnO in air, the ZnO_2 powder prepared by addition of the 3 % H_2O_2 was annealed at various annealing temperatures from 200 to 600 °C for 8 hours under 1 atmospheric pressure.
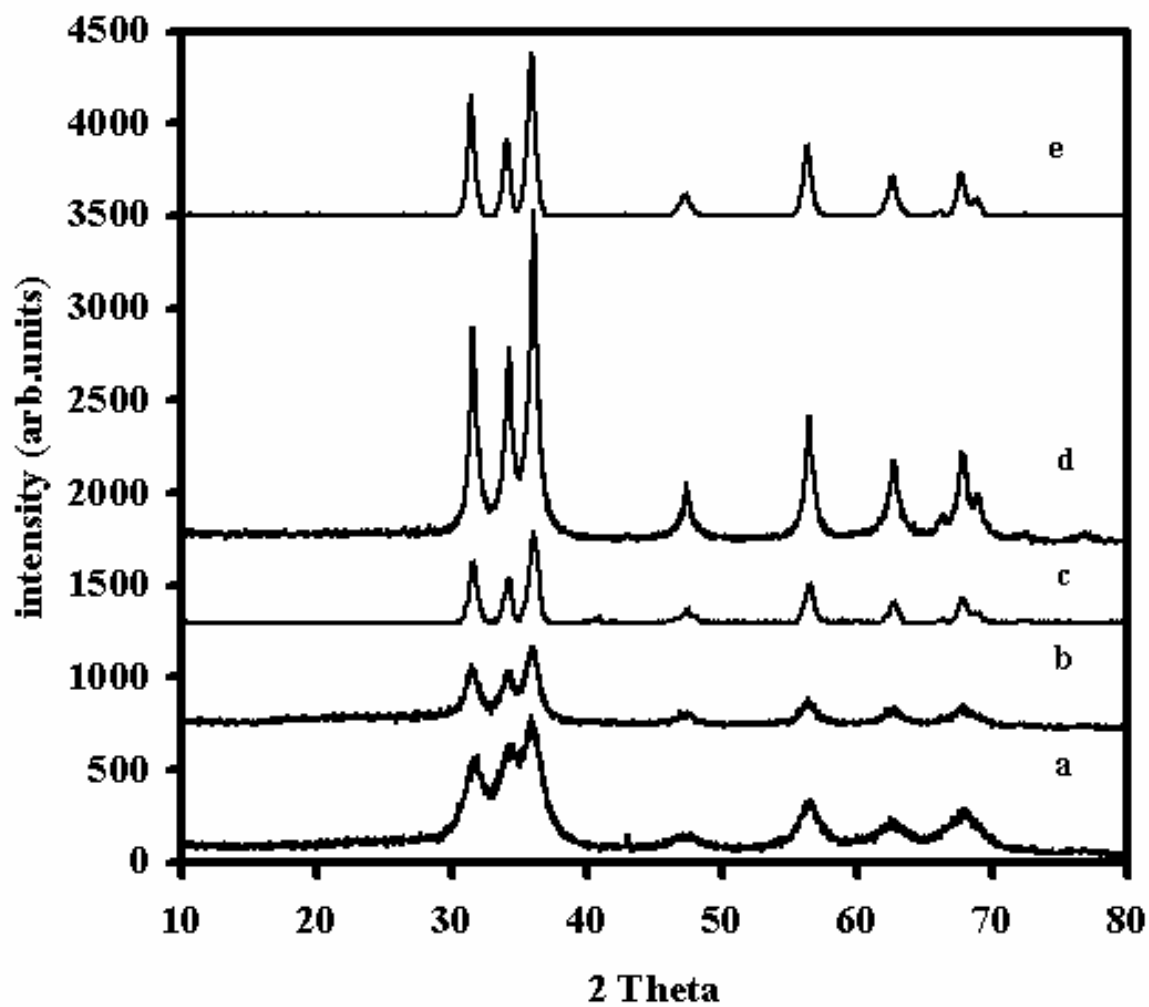
Figure 4-28. XRD patterns of ZnO prepared by annealing temperature of ZnO_2 at a) 200 °C b) 300 °C, c) 400°C, d) 500°C and e) 600 °C.

4.6.1. Effect of annealing temperature on grain size

ZnO starts to emerge by annealing ZnO_2 around 130 °C. It has been reported that ZnO_2 is converted completely into ZnO around 200 °C by following reaction [89]:

$$ZnO_2 \rightarrow ZnO + \frac{1}{2} O_2$$
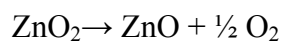
The average grain size 'd' of the nanoparticle of ZnO generated by annealing the ZnO_2 was estimated by using the standard equation known as Scherrer formula. The mean grain size of (002) oriented ZnO at angle 36.4° from Figs 4-28 a , b, c, d and e are 5, 6, 9, 15 and 19 nm respectively and are listed in Table 4.7. The trend in increase in the grain size due to rise in annealing temperature is presented in Fig.4-29. The increase in grain size with annealing temperature could be attributed to agglomeration process which usually happens at higher temperatures and some other thermal effects such as Ostwald ripening where the formation of larger particles are more energetically favored than smaller particles. This stems from the fact that molecules on the surface of a particle are energetically less stable than the ones already well ordered and packed in the interior. Large particles, with their lower surface to volume ratio, result in a lower energy state (and have a lower surface energy). As the system tries to lower its overall energy, molecules on the surface of a small (energetically unfavorable) particle will tend to diffuse and add to the surface of larger particle. Therefore, the numbers of smaller particles continue to shrink while larger particles continue to grow in size [96, 97].

4.6.2. Effect of annealing temperature on lattice parameters

During this study, the effect of annealing temperature on the crystalline structure was also investigated and for this purpose the lattice parameters were estimated at different temperature. By applying previous method, the lattice parameters were calculated from the XRD spectrum (see figure 4-30) recorded at different annealing temperature for ZnO. The estimated parameters at different temperatures are plotted in Figure 4-29 and listed in table 4-6. It is clear form table 4-6 that lattice parameters increase with the rise in annealing temperature. This increase of lattice parameter due to the increase of thermal energy has been reported for different crystalline materials elsewhere [98-99].

Table 4-6. Lattice parameters and grain size at different annealing temperatures

Temperature (°C)	Lattice parameters		Grain size nm	No. of unit cells, n
	a (°A)	c (°A)		
200	3.253	5.233	5	227
300	3.261	5.236	6	390
400	3.269	5.238	9	7367
500	3.274	5.241	15	24772
600	3.282	5.258	19	12191

4.6.3. Effect of annealing temperature on the optical properties

A study of the photo-luminous (PL) property of any material is interesting because it can provide valuable information on the quality and purity of the material. The semiconductor ZnO nanoparticles, with sizes comparable to or below their exciton Bohr radius, have distinctive electronic and optical behaviors due to exciton quantum confinement phenomena. For such reasons, "quantum dots" suitably describe these semiconductor nanoparticles which absorb light at specific wavelength and emit it at longer wavelength. Therefore, recording of PL spectrum is of paramount importance for estimating the size of nanoparticles and their characteristics for various applications. The photoluminescence (PL) spectra of ZnO were recorded in the UV (360-560 nm) region and is depicted in Fig. 4-30. Clearly, the emission peak around 374 shifts to longer wavelength (red shifting) as the annealing temperature increase from 200 to 600 °C. We believe this is a result of defects related to shallow binding excitons formed during high temperature annealing. Our result is contrary to an earlier report earlier [100] that increasing the annealing for 5 hour at 500 ºC shows increase in the intensity of UV peak and decrease in green emission.

It has been reported [101] that stoichiometric pure ZnO thin films usually show strong UV luminescence and no visible spectrum. If there is any visible luminescence in the spectrum, it is due to defects related to deep level emissions, such as Zn interstitials

or oxygen vacancies. We did not observe any visible luminescence in our case which also indicates that ZnO prepared with our method is more pure and stoichiometrically perfect.
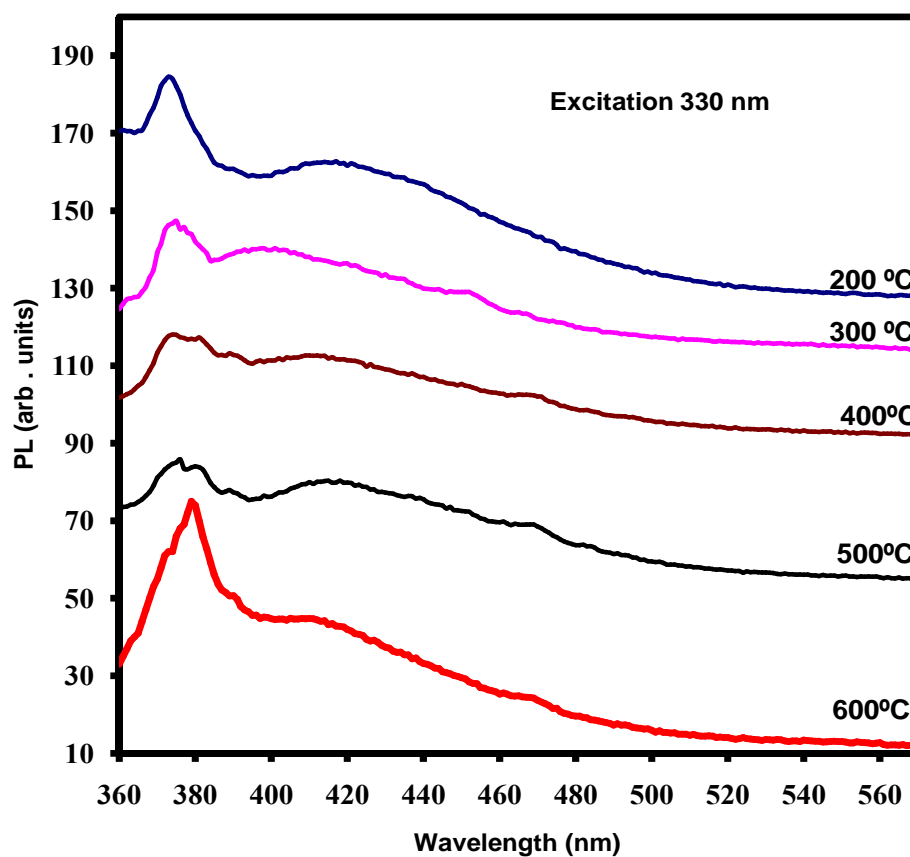
Figure 4-29. Photoluminescence emission spectra for ZnO prepared by post annealing of ZnO₂ at 200 ºC , 300 ºC , 400 ºC ,500 C and 600 ºC.
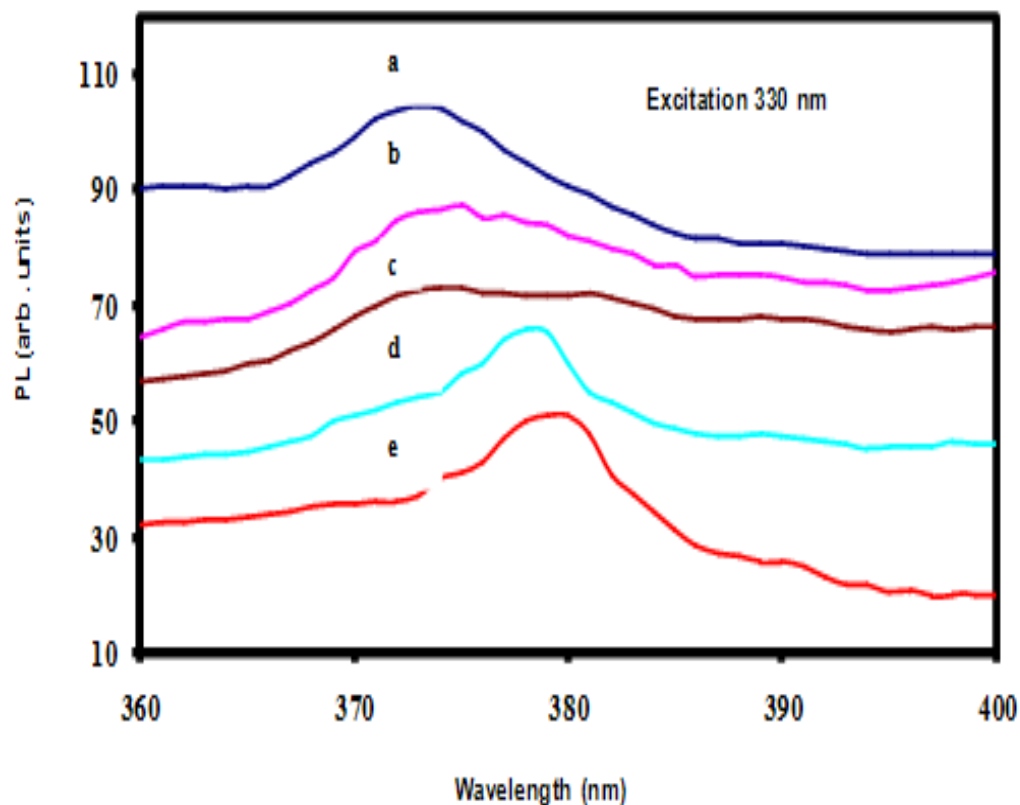
Figure 4-30. Enlarged PL emission spectra (range 360 to 400 nm) for ZnO prepared by post annealing of ZnO₂ at a) 200 ℃ , b) 300 ℃ , c) 400 ℃ , d) 500 C and e) 600 ℃.

Fig. 4-32 depicts comparison of the UV-VIS absorption spectra of ZnO prepared without oxidizing agent and annealed zinc oxide at 600 °C. It is clear that the exciton absorption peak of the fresh sample (348 nm) is shifted to 373 nm with the increase in annealing temperature. In addition to the shifts of the absorption edges, there are

substantial tails on the longer wavelength side of the absorbance spectra as depicted in

Fig. 4-32.
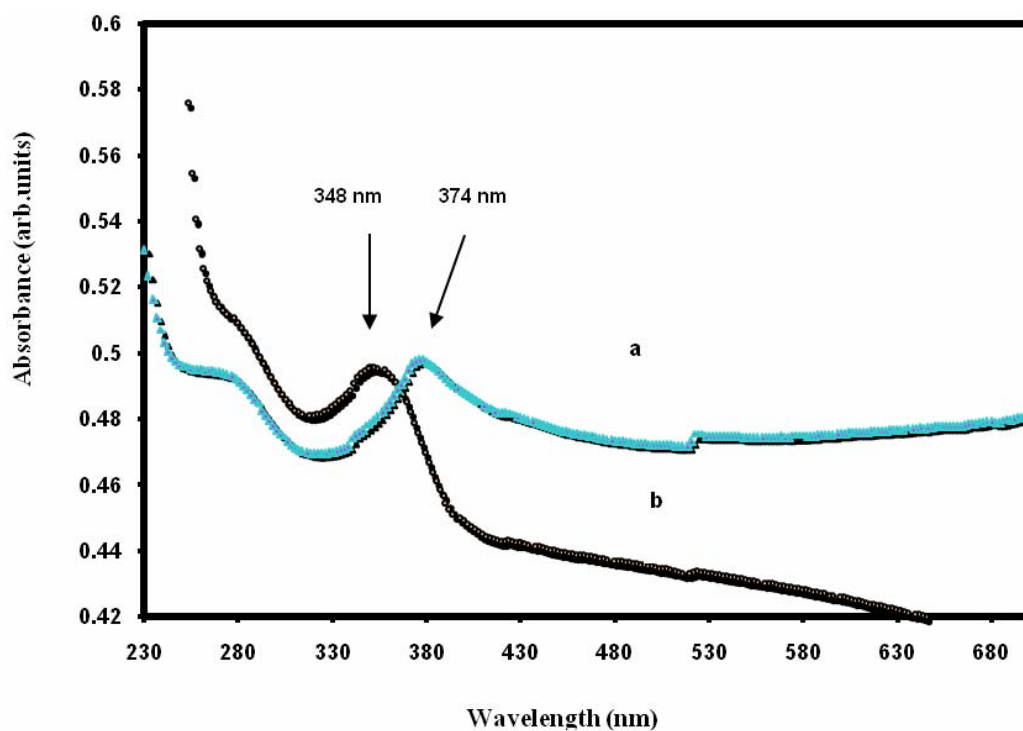
Figure 4-31. Absorption spectra of ZnO nanoparticles prepared by a) laser ablation

of zinc in deionized water b) post annealing of ZnO₂ (at 600 °C).
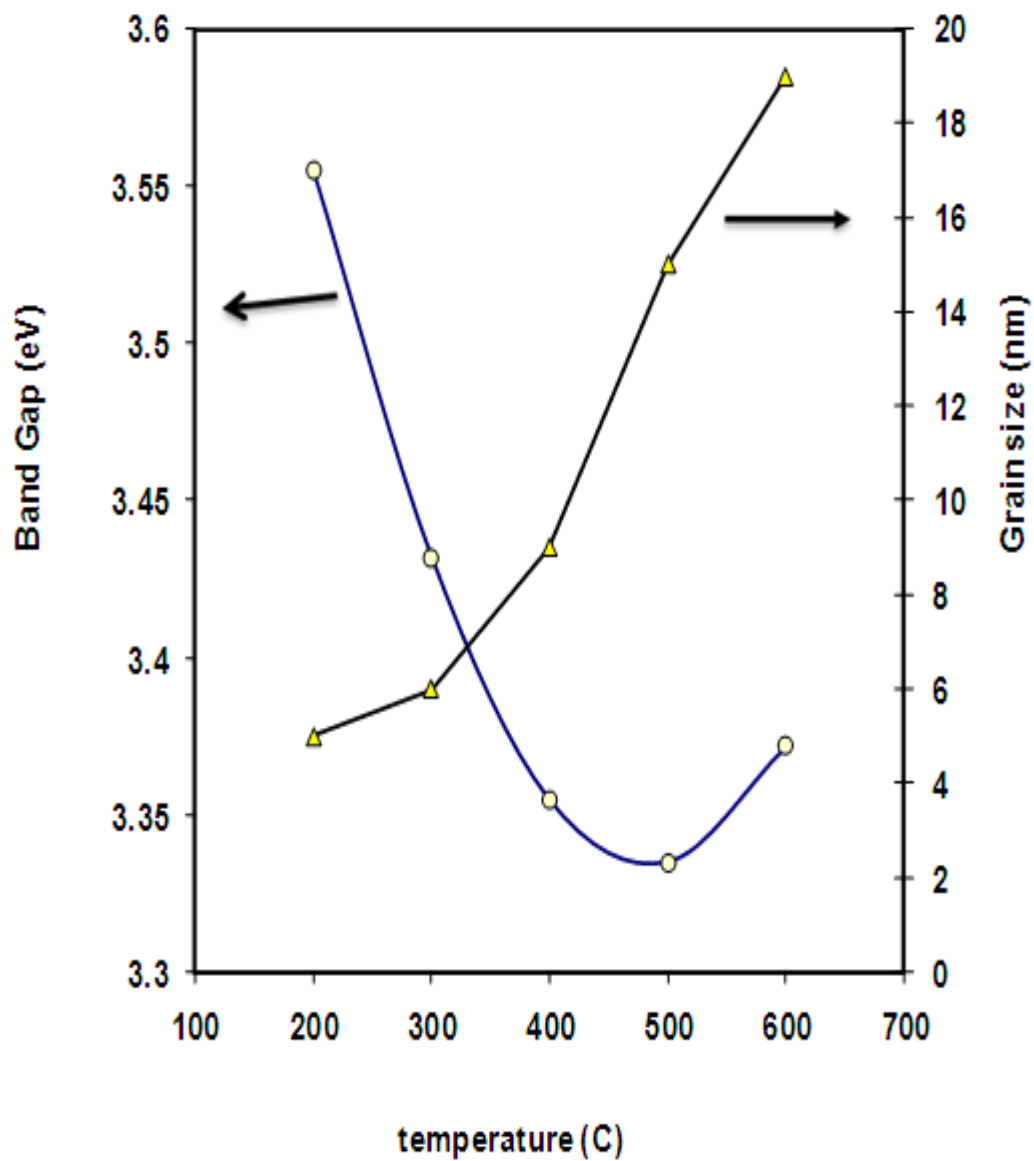
Figure 4-32. Variation of grain size and energy band gap versus the annealing temperature for ZnO produced from ZnO_2 prepared by pulsed laser ablation in 3% H_2O_2 water solution.

Experimentally, the direct band gap of semiconductor can be estimated from the relation between the absorption coefficient and UV photon energy which is given by:

$$\alpha E = A (E - E_g)^{1/2}$$

Where E is the photon energy, E_g is the direct band gap of the semiconductor, A is a constant. Therefore, a plot of $(\alpha E)^2$ versus photon energy E should yield a straight line that cut the photon energy axis at the band gap.
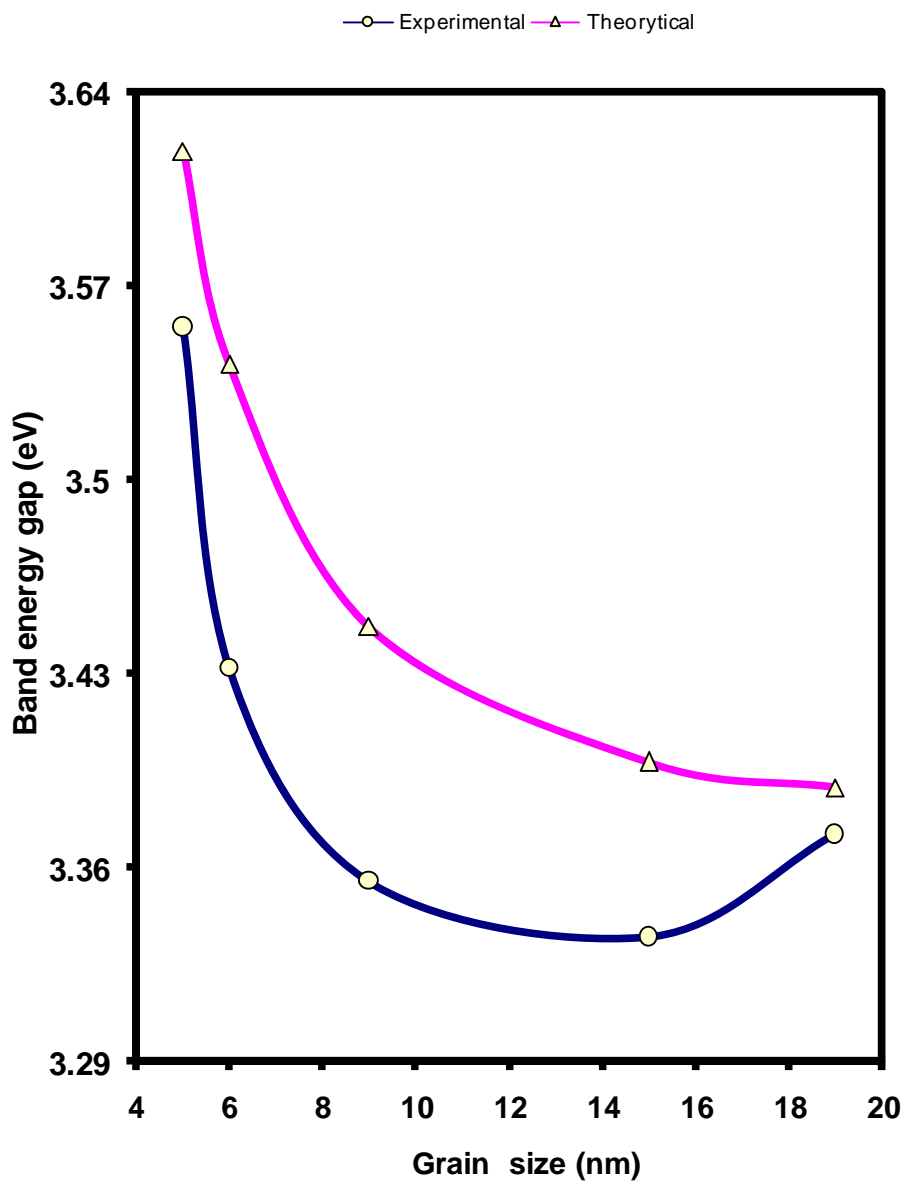
Figure 4-33. Variation of energy band gap versus the grain size of ZnO produced

from ZnO$_2$ prepared by pulsed laser ablation in 3 % H$_2$O$_2$ water solution

Fig 4-34 depicts the dependence of the band gap (E_g) on the grain sizes. The band gap decreases with increasing temperature and with increasing grain size. This change in band gap can be understood due to electronic structure dependence on size of nanocrystals especially in ultra-fine size such as quantum dots. From the experimental data, one can see that the E_g change is more prominent when the grain sizes are less than 10 nm and this could be due to quantum effects. Band gap variation of size-controlled ZnO has been reported in reference [103]

Fourier transform infrared (FTIR) spectra were measured at room temperature with an FTIR spectrometer using the KBr pellet technique. FTIR measurements are essential to confirm the formation of crystalline ZnO nanocrystals and to identify any adsorbed species onto the surface of nanoparticles. Hence, FTIR spectra of the nanoparticles products without and with annealing treatment were performed for a better comprehension of the structure and composition of these materials. The spectrum for bulk ZnO is also included for comparison purposes [104].

Fig. 4-35 depicts a typical FTIR spectrum of the ZnO in various forms. Fig 4.35.a is the FTIR spectrum of bulk ZnO, Fig. 4-35.b is of Nano ZnO produced directly without annealing, Fig 4-35.c and d are of annealed ZnO generated from indirect method at 200 ^{o}C and 600°C An absorption band revealing the vibrational properties of ZnO nanocrystals is observed for each sample in the range of 430-495 cm^{-1}. This band is mainly assigned to the stretching vibrations of Zn−O.

Commercial bulk ZnO powders show absorption of this band at about 442.6 cm^{-1} while in our case it is at 479.3 cm^{-1} for nanoparticle ZnO produced by direct method. When the nano ZnO produced through indirect method was thermally treated (annealing treatment), a shift of the IR absorption peak toward a low wavenumber (red shift) was observed. This band (479.3 cm^{-1}) is shifted to 464.0 and 457.7 cm^{-1} after annealing at 200 and 600 °C, respectively (table 4-7). Figure 4-36 is an enlargement of the FTIR spectra in the 430-495 cm^{-1} region.

Table 4-7. Absorption bands of annealed nanoparticles

Annealing Temperature (°C)	Wavenumber of (υZn−O) (cm^{-1})
0	479.3
200	464.0
600	457.7

Considering XRD measurements which show the ZnO as a major product, the more symmetrical peak at about 457.7 cm^{-1} (annealing @ 600°C) indicates more uniformity of the ordered oxide structure. Such attractive uniformity, along with the high adsorption properties, offer great promise for using these nanoparticles for designing new sensitive

sensors for different gases to be applied for different industrial and environmental applications.

The broad absorption peaks in the range of 3410-3465 cm^{-1} correspond to –OH group, and indicates the existence of water absorbed on the surface of nanocrystals. The presence of this band can clearly be attributed to the adsorption of some atmospheric water during FT-IR measurements. Those at 1500-1650 cm^{-1} and at about 2370 cm^{-1} are the C= O stretching mode arising from the absorption of atmospheric CO_2 on the surface of the nanoparticles [105].
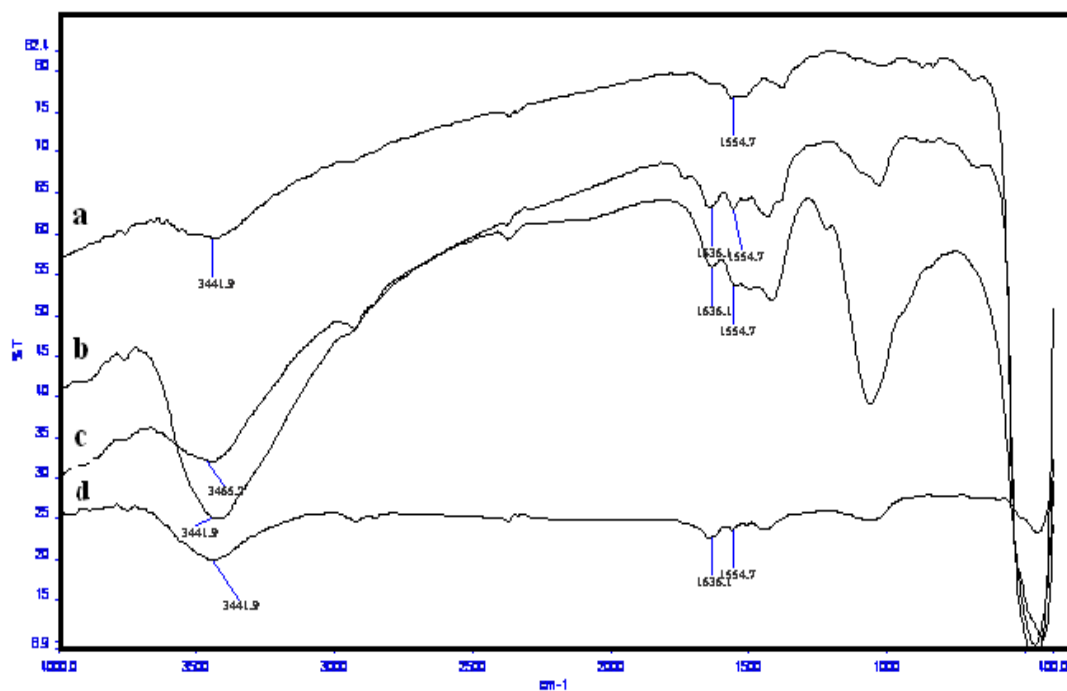
Figure 4-34. Typical FTIR spectra of ZnO: a) bulk, b) nanoparticles product, c)) nanoparticles product annealed at 200°C, d) nanoparticles product annealed at 600°C.
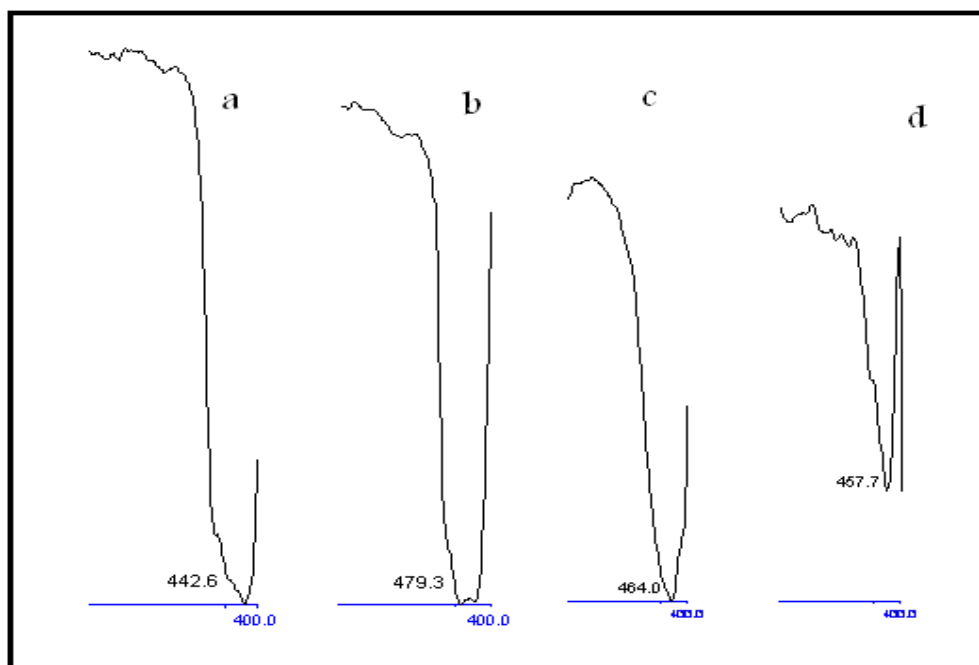
Figure 4-35. Enlarged FTIR spectra in the range of 430-495 cm-1 , stretching vibrations of Zn−O (υZn−O):   a) bulk, b) nanoparticles product, c)) nanoparticles product annealed at 200°C, d) nanoparticles product annealed at 600°C.

4.7. SYNTHESIS AND CHARACTERIZATION OF SnO$_2$ NANOPARTICLES

SnO$_2$ is an n type semiconductor crystal with direct band gap (3.7 eV at 300 K) and high excitonic binding energy (130 eV). It has many applications in the transparent conducting coating of glass, gas sensors, solar cell, and heat mirror [106-108]. SnO$_2$ nanostructure can be fabricated using different methods such as: sputtering [109], sol gel [110], reverse cell [111], thermal evaporation [112] and surfactants mediate [113].

In order to synthesize SnO$_2$ nanoparticles by (PLA) in water, a laser based setup was designed and fabricated locally which is depicted in Fig. 4-37. A high-purity metallic tin foil, 0.5 mm thick, and purity 99.999% (Sigma Aldrich Company) was fixed at the bottom of a glass cell as the target, and was rotated by a home made magnetic stirrer to avoid deep hole ablation. Typical laser pulse energy for PLA process was 180 mill joules per pulse. The laser beam was focused by a lens with a focal length of 250 mm in order to get sufficient laser fluence for the ablation. The typical diameter of the laser spot on a bulk target was ~ 0.08 mm and the typical liquid volume was 7 ml. After laser irradiation time of 40 min, a yellow colloidal solution of SnO$_2$ based nano materials was obtained. The colloidal suspension was using centrifuge. A variety of techniques were applied for the characterization of SnO$_2$ products. X Ray Diffraction (XRD) was employed to determine crystalline phases and average crystalline size. Photoluminescence spectra were studied using a Specroflurometer (Shimadzu RF-5301

PC) equipped with 150-W Xe lamp as the excitation source. FTIR spectrometer: Infrared absorption spectroscopy (IR) spectra were measured at room temperature on a FTIR spectrometer using the KBr Pellet technique. UV-Vis Spectroscopy: UV-Vis spectrometer (JASCO V-570) was used to record the UV-Vis absorption spectra
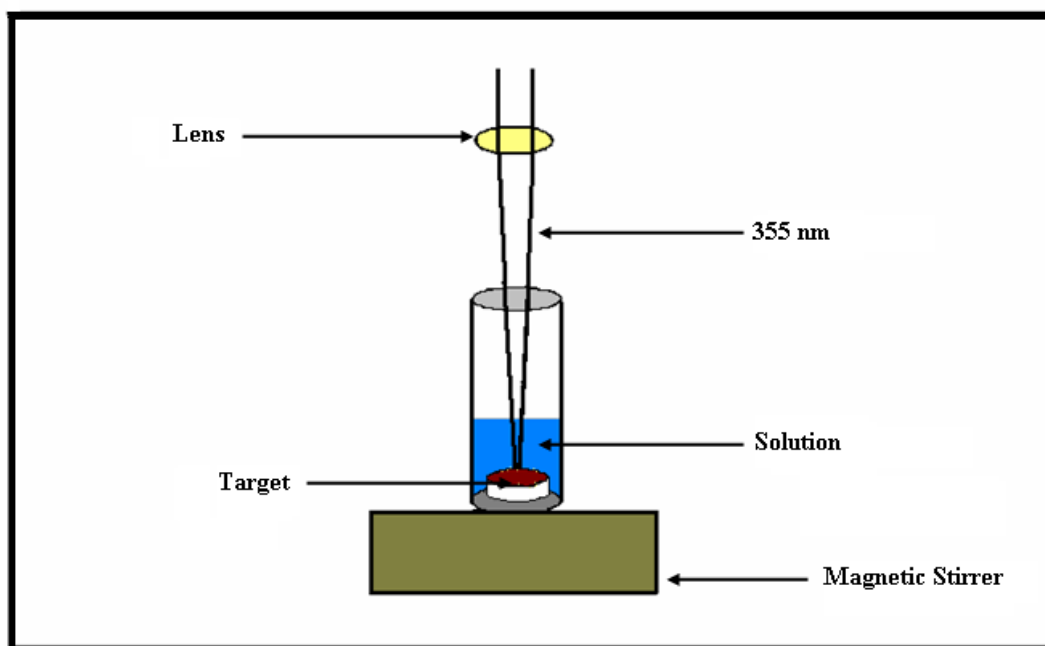
Figure 4-36. Typical set up for pulsed laser ablation in liquid media.

The X ray diffraction study of SnO_2 nanoparticles prepared by PLA in water was carried out on a dry film obtained by drop coating nanoparticles suspension on glass substrate and evaporating the water. Fig. 4-38 shows the XRD spectrum of SnO_2 nanoparticles synthesized using PLA in deionized water. The diffraction spectrum and interplane spacing of the products were in agreement with the standard diffraction pattern of SnO_2, confirming the formation of SnO_2 nanocrystals implying that ablated Sn

species were in the presence of water. The main dominant peaks of SnO_2 were identified

at $2\theta =$ 26.66°, 34.18°, 52.3°, 61.34°, 64.4° and 65.54° which corresponding to (110),

(101), (211), (112), (301) and (302) and the three strong peaks are assigned to the

(110), (101) and (211). The lattice parameters of SnO_2 which represent the tetragonal

rutile were estimated by the equation:

$$Sin\theta = \frac{\lambda}{2}\sqrt{(\frac{h^2 + k^2}{a^2} + \frac{l^2}{c^2})} \tag{1}$$

Where λ is the wavelength of the incident X-ray, (h,k,l) are miller indices, θ is the

diffraction angle and a and c are the lattice parameters. By applying the above equation

the lattice parameter a is 4.741°A and c is 3.187°A. The average sizes "d" of SnO_2

nanoparticles were calculated using the above Scherrer formula at ($2\theta = 26.66°$) is 3 nm.

To confirm the size of SnO_2 nanoparticles, a typical AFM image of such SnO_2

nanoparticles prepared by PLA in deionized water was used and presented in figure 4-

39.
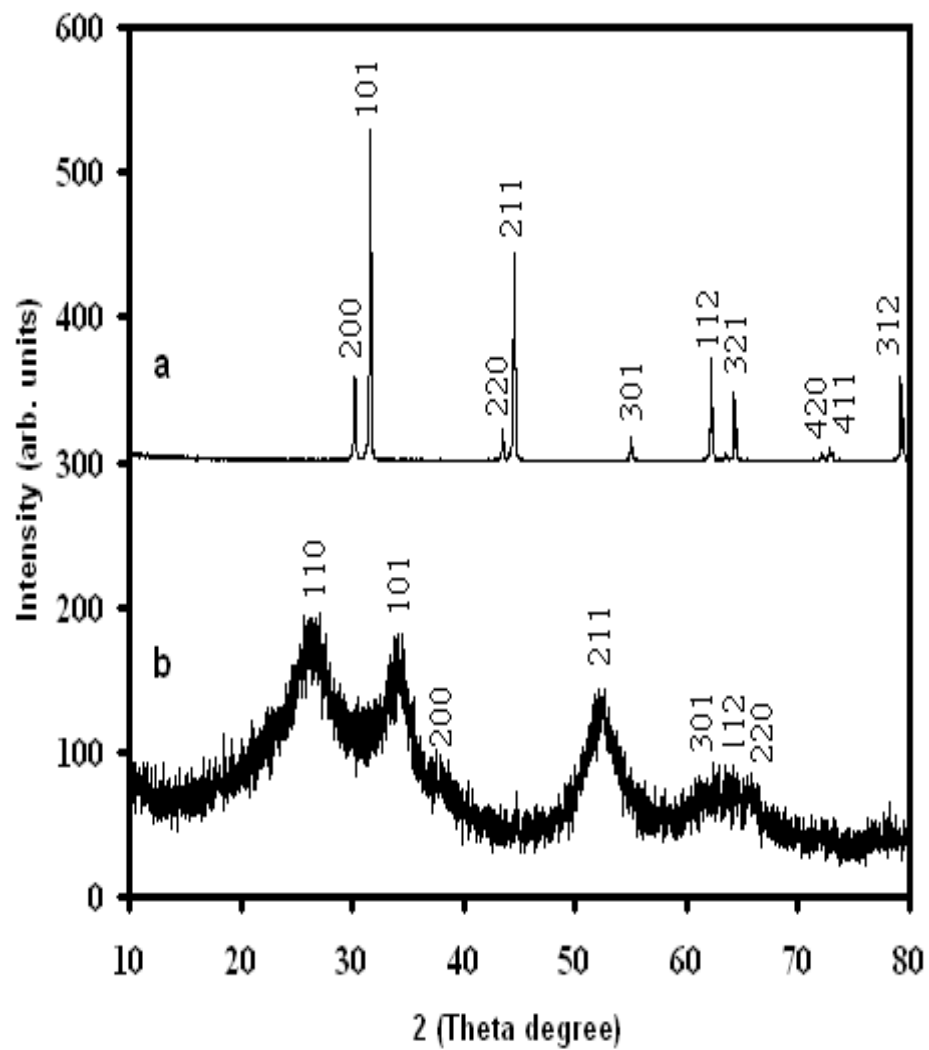
Figure 4-37. XRD spectra of a) tin target and b) tin dioxide nanoparticles obtained by laser ablation in deionized water
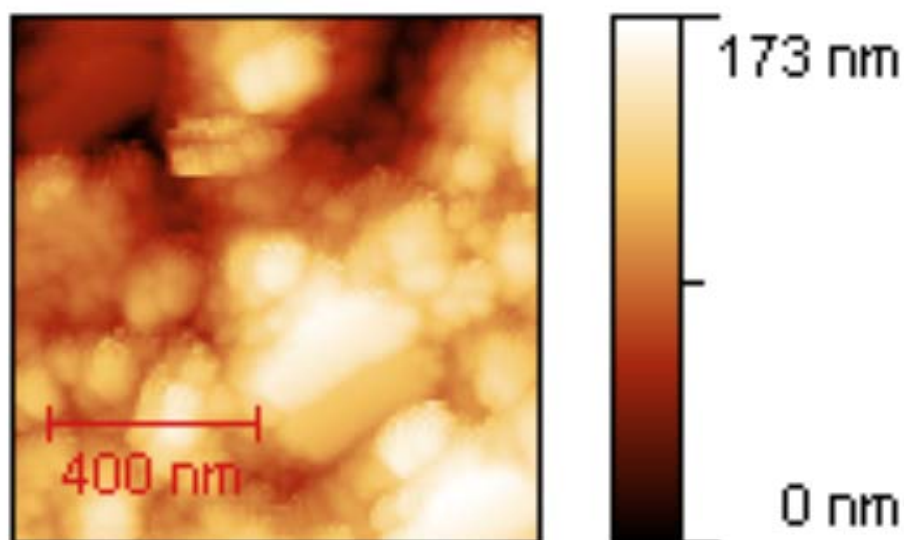
Figure 4-38. A typical AFM image of the SnO$_2$ nanoparticles prepared by PLA.

The optical absorbance of the deionized water solution containing SnO$_2$ nanoparticles was measured in the wavelength between 200 nm to 500 nm at room temperature using a JASCOV–570 spectrophotometer. Fig. 4-40 shows UV-visible spectrum of colloidal solution obtained by pulsed laser ablation of Sn in deionized water. SnO$_2$ exciton absorption peak is located at 240 nm and blue shifted relative to the bulk exciton absorption (220 nm). This blue shift indicates the quantum confinement property of nanoparticles. In the quantum confinement rang, the band gap of the particle increases resulting in the shift of absorption edge to lower wavelength, as the particle size decreases. The direct band gap of semiconductors can be estimated from the relation between the absorption coefficient and UV photon energy which is given by:

$$\alpha \, E = A \, (h\nu - E_g)^{1/2} \tag{4}$$

where E is the photon energy, E_g is the direct band gap of the semiconductor, A is a constant. Therefore, a plot of $(\alpha E)^2$ versus photon energy E should yield a straight line that cuts the photon energy axis at the band gap. From the inset of fig. 4-41, E_g is about 4.404 eV.
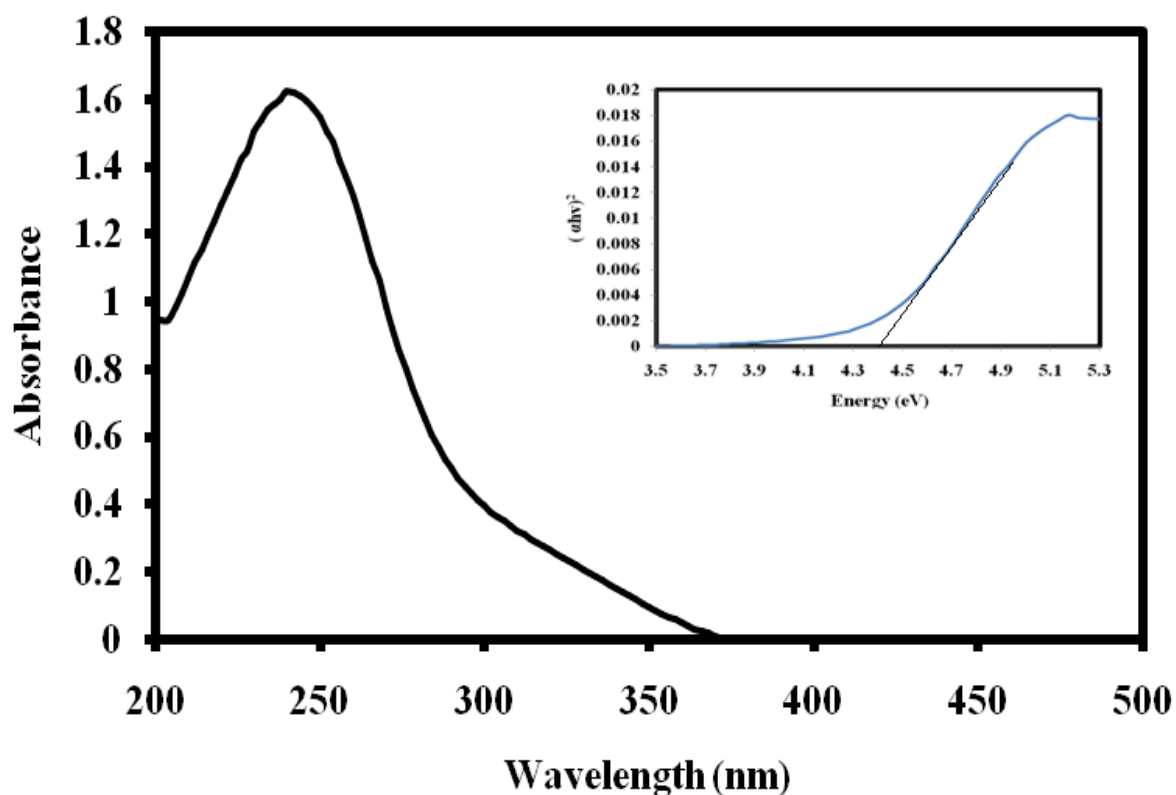
Figure 4-39. Aborption spectrum of tin dioxide nanoparticles prepared by PLA of tin in deionized water and the inset shows E_g.

Infrared absorption spectroscopy (IR) spectra were measured at room temperature on a FTIR spectrometer using the KBr Pellet technique. Samples were lyophilized, gently mixed with 300 mg of KBr powder and compressed into discs at a force of 17 kN

for 7 min using a manual tablet presser. Figures 4-41 and 4-42 depict the FT-IR transmission spectrum of SnO_2 nanoparticles synthesized by pulsed laser ablation technique. The absorption peaks at 3100-3431 and $1635cm^{-1}$ were attributed to the vibration of hydroxyl due to the fact that SnO_2 retained certain adsorbed water. The bands observed in the range of $1070 \ cm^{-1}$ were assigned to the vibration of different types of surface hydroxyl groups [111]. The band at approximately $2399 \ cm^{-1}$ resulted from the adsorption and interaction of atmospheric carbon dioxide with water according to the literature. A band appeared in the range of $400\text{-}700cm^{-1}$ is assigned to Sn–O antisymmetric vibrations [114]. The presence of such a vibration in the synthesized samples confirms the presence of SnO_2 [115].
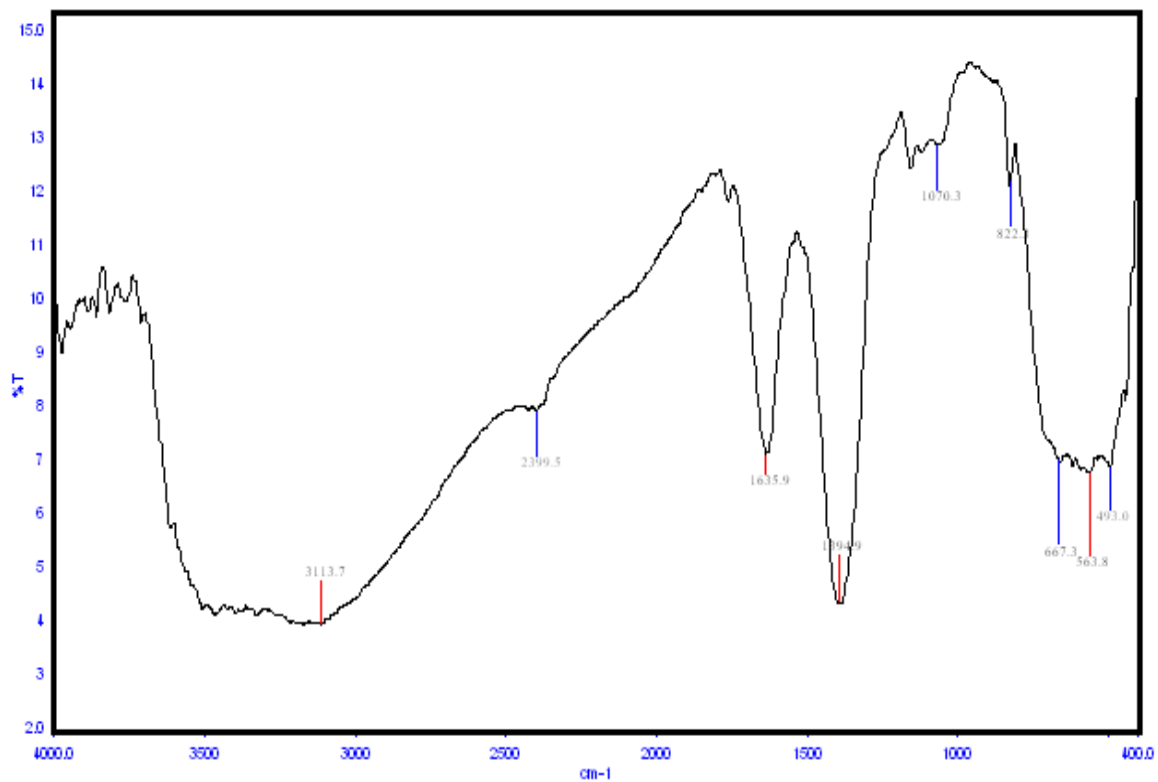
4-40. FTIR spectrum of SnO₂ nanoparticles synthesized by laser ablation.
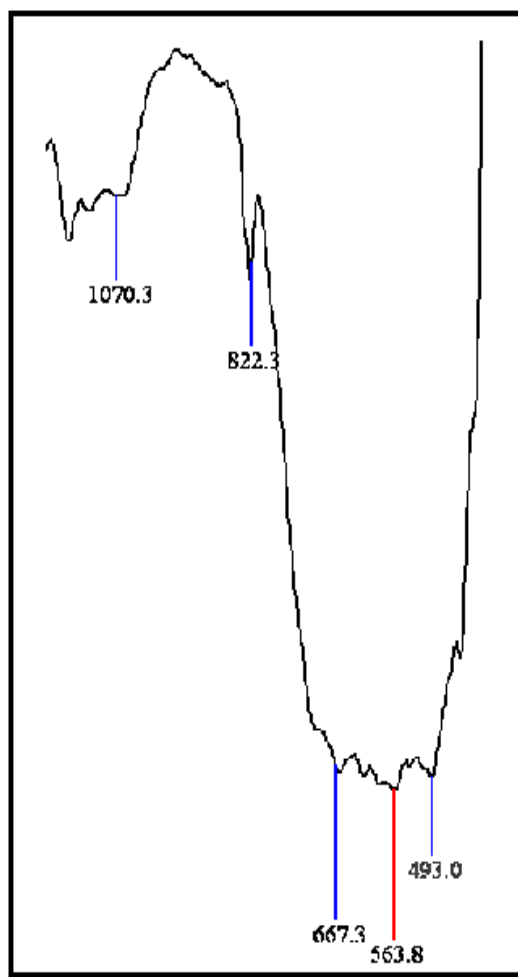
Figure 4-41. Enlarged FTIR spectra in the region 425–450 cm^{-1} for the SnO$_2$ nanoparticles synthesized by laser ablation

The PL emission spectrum for SnO$_2$ nanoparticles were prepared at room temperature by means of PLA in water at an excitation wavelength of 220 nm is shown in Fig. 4-43. The fitting peak shows three peaks centered at 391, 427 and 475 nm corresponding to 3.175, 2.901 and 2.613 eV respectively. These three peaks are smaller than the band gap of SnO$_2$ which is 4.404 eV and so we can not ascribe them to the

direct recombination of electron in the conduction band to a hole in valance band. The PL peaks positions of the synthesized SnO_2 nanoparticles have a blue shift comparing with SnO_2 prepared by other technique which is due to the decrease sizes [116-117]. Gu, F. et al. [118] prepared SnO_2 thin film by spin coating method and they found two emission peaks centered at 400 and 430 nm. Based on their explanation the emission peak at 400 nm is due to electron transition mediated by the defects level in the band gap such as oxygen vacancies. Basically, V_o^0, V_o^+ and Vo^{++} are the possible charge state of oxygen vacancies and due to the photoexcition of SnO_2 the hole mightily trapped at the V_o^+ center to form V_o^{++} center. And the emission peak at around 400 nm mightily appears due to the recombination of a conduction band electron with V_o^{++} center. On the other hand, the peak at 430 nm can be related to the luminescence centers formed by such tin interstitials. It has been reported [119] that the blue luminescence of SnO_2 (475 nm) is due to oxygen-related defects that have been introduced during growth.
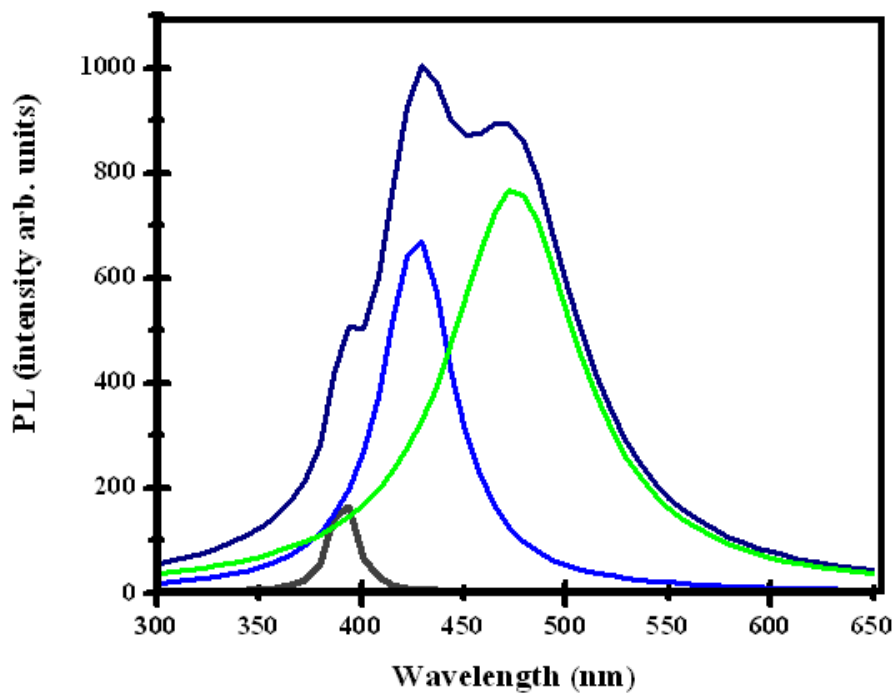
Figure 4-42. Photoluminescence spectrum of tin dioxide nanoparticles prepared by PLA of tin in deionized water and its fitting peaks using origin program.

CHAPTER 5

CONCLUSION

The aim of this study was to fabricate metal oxide and peroxide nanoparticles in liquids using pulsed laser and investigate the effect of different parameters such as surfactants, temperature and laser energy on the production materials.

For the synthesis of nanoparticles, a high-purity metallic plate of zinc and tin is fixed at the bottom of a glass cell as the target, and is rotated using a home made magnetic stirrer to avoid a deep ablation traces or crusts. Typical laser pulse energy for PLA process was between 40-130 milli joules per pulse. The laser beam was focused by a lens with a focal length of 250 mm in order to get sufficient laser fluence for the ablation. The typical diameter of the laser spot on a bulk target was ~ 0.08 mm and the typical liquid volume was 10 ml.

ZnO nanocrystals were synthesized by PLA techniques in water, CTAB and OGM surfactants. The presence of the hexagonal phase of zinc oxide in all samples was confirmed with XRD, and the grain sizes were 38 nm 27 nm and 19 nm in deionized; and H_2O mixed with CTAB and OGM respectively. The photoluminescence (PL) spectra of ZnO nanoparticles prepared by PLA in deionized water showed two peaks: the first and strong peak centered at 375 nm which is due to the recombination of electron from valance band with hole in the conduction band. The second PL peak centering at violet luminescence 420 nm is due to zinc defects. The PL emission in

115

CTAB and OGM showed two peaks: the sharp UV emission at 380 nm and a broad visible peak ranging from 450 nm to 600 nm which is due to surfactants impurities.

For the first time, zinc peroxide ZnO_2 nanoparticles with grain size of 4 nm were synthesized using PLA of solid target in 3 % H_2O_2 and in presence of different surfactants. The effect of surfactants on the optical and structure of ZnO_2 was studied by applying different spectroscopic techniques. The presence of the cubic phase of zinc peroxide in all samples was confirmed using XRD, and the grain sizes were 4.7 nm, 3.7 nm, 3.3 nm and 2.8 nm in pure 3% H_2O_2; and H_2O_2 mixed with SDS, CTAB and OGM respectively. For optical characterization, FTIR transmittance spectra of ZnO_2 nanoparticles prepared with and without surfactants were showed a characteristic ZnO_2 absorption at 435-445 cm^{-1}. FTIR spectrum revealed that the adsorbed surfactants on zinc peroxide disappeared in case of CTAB and OGM while it appears in case of SDS. This could be due to high critical micelles SDS concentration comparing with others which is attributed to the adsorption anionic nature of this surfactant. Both FTIR and UV-Vis spectra show a red shift in presence of SDS and blue shift in presence of CTAB and OGM. The blue shift in the absorption edge indicates the quantum confinement property of nanoparticles. By variation of the annealing temperature from 100 to 600 ^0C for 8 hours, the products were converted completely to ZnO at 200 ^0C. Grain sizes, lattice parameters, band energy gap and PL emission were size dependence.

Nanocrystalline tin dioxide SnO_2 nanoparticles with the average particle size of 3 nm were obtained by using high power PLA in deionized water. SnO_2 were

characterized by XRD, FTIR, UV–visible absorption and PL. The XRD pattern of the nanoparticles prepared is indexed to rutile phase of tin dioxide without any trace of an extra phase. The UV–visible absorption shows a blue shift in the absorption edge which indicates the quantum confinement property of nanoparticles. The band gap of the prepared sample is 4.4 eV which is greater than the bulk tin dioxide. FTIR transmittance spectrum of SnO_2 nanoparticles shows a characteristic Sn-O absorption at 400-700 cm^{-1}. The fitting peaks of PL show three emission peaks centered at 391, 427 and 475 nm.

In general, PLA is a powerful technique to prepare zinc oxide, zinc oxide and zinc peroxide. In future, different materials (metallic, alloys, oxides, peroxides) can also produce using this technique. In addition, laser and liquid parameters can further be investigated.

REFERENCES

1. M.H. Hong, K. Sugioka, Y.F. Lu, K. Midorikawa and T. C. Chong, Laser microfabrication of transparent hard materials and signal diagnostics, Appl. Surf. Sci., 186 (2002), p. 556.

2. E. Gu, H. Howard, A. Conneely, G.M. O'Connor, M.R.H. Knowles, P.R. Edwards, R.W. Martin, I.M. Watson, M.D. Dawson, Microfabrication in free-standing gallium nitride using UV laser micromachining, Appl. Surf. Sci, 252 (2006), p. 4897.

3. A. Kaminska, M. Sawczak, K. Komar and G. Śliwiński, Application of the laser ablation for conservation of historical paper documents, Appl. Surf. Sci., 253 (2007), p. 7860.

4. J.E. Ready, Industrial Applications of Lasers, Acadimic press, New York, 1978.

5. Z. PaÂszti, G. PetoÄ, Z.E. HorvaÂth, A. Karacs, Laser ablation induced formation of nanoparticles and nanocrystal networks, Appl. Surf. Sci., 168 (2000), p. 114.

6. P. Šmejkal, J. Pfleger, B. Vlčková and O. Dammer, Laser ablation of silver in aqueous ambient: effect of laser pulse wavelength and energy on efficiency of the process, J. of Phys.: Conference Series., 59 (2007), p. 185.

7. H. W. Kang, J. Oh and A. J. Welch, Investigations on laser hard tissue ablation under various environments, Phys. Med. Biol., 53 (2008), p. 3381.

8. F. Brech and L. Cross, Optical micro-emission stimulated by a Ruby Maser, Appl. Spectro., 16 (1962), p. 59.

9.   W. L. Linlor, Plasmas produced by laser bursts, Bulletin of the American Phys. Soc., Vol. 7, (1962), p. 440.

10. H. M. Smith and A. F. Turner, deposition thin films using a ruby laser, Appl. Opt, 4 (1965), p. 147.

11. S. B. Ogale, P. P. Patil, D. M. Phase, Y. V. Bhandarkar, S. K. Kulkarni, Smita Kulkarni, S. V. Ghaisas, and S. M. Kanetkar, Synthesis of metastable phases via pulsed-laser-induced reactive quenching at liquid-solid interfaces, Phys. Rev. B, 36 (1987), p. 8237.

12. P. P. Patil, D. M. Phase, S. A. Kulkarni, S. V. Ghaisas, S. K. Kulkarni, S. M. Kanetkar, and S. B. Ogale, Pulsed-laser–induced reactive quenching at liquid-solid interface: Aqueous oxidation of iron, Phys. Rev. Lett., 58 (1987), p. 238.

13.   R. H. J. Hannink and A. J. Hill, Nanostructure control of materials, CRC Press Boca Raton Boston New York Washington, DC (2006).

14. W. W. Gerberich, W. M. Moo, C. R. Perrey, C. B. Carter, M. I. Baskes, R. Mukherjee, A. Gidwani, J. Heberlein, P. H. McMurry and S. L. Girshick, Superhard silicon nanospheres, J. of the Mech. and Phys. of Soli., 51(2003), p. 979.

15. M. J. Pitkethy. Nanoparticles as building blocks, Materialstoday, 6 (2003), p. 36.

16. G. Mie, contributions to the optics of diffuse media, especially colloid metal solutions), Ann. Phys., 25 (1908), p. 377.

17. R. Feynman, "There's plenty of room at the bottom", Miniaturization, edited by H.D.Gilbert, Reinhold, New York, 1961.

18. B. Brinda. Lakshmi, J. Charles. Patrissi, and R. Charles. Martin, Sol-Gel Template Synthesis of Semiconductor Oxide Micro- and Nanostructures, Chem. Mater., 9 (1997), p. 2544.

19. A. A. Ismail, Synthesis and characterization of Y2O3/Fe2O3/TiO2 nanoparticles by sol–gel method, Appli. Catal. B: Enviro., 58 (2005), p.115.

20. J. Zhang and L.Gao , Synthesis of SnO2 Nanoparticles by the Sol-gel Method From Granulated Tin, Chem. Lett. Vol., 32 (2003), p. 458.

21. L.C. Damonte, L.A. Mendoza Ze´lis, B. Marı´ Soucase, M.A. Herna´ndez Fenollosa, Nanoparticles of ZnO obtained by mechanical milling, Powder Technology, 148 (2004), p. 15.

22. A.M. Glushenkov, H.Z. Zhang, Y. Chen, Reactive ball milling to produce nanocrystalline ZnO, Mater. Lett., 62 (2008), p. 4047.

23. C. Cao, Nanostructures and nonmaterials synthesis properties and applications, imperial college press, (2004) USA.

24. W. Gao and Z. Li, ZnO thin films produced by magnetron sputtering, Ceramics International, 30 (2004) p.1155.

25. J. Will, A. Mitterdorfer, C. Kleinlogel, D. Perednis and L. J. Gauckler, Fabrication of thin electrolytes for second-generation solid oxide fuel cells, Solid. Stat. Ionics ,131 (2000) p. 79.

26. P Sen, J Ghosh, A. Alqudami, P Kumar and Vandana   Preparation of of Cu, Ag, Fe and Al nanoparticles by the exploding wire technique, J. of Chem. Sci., 115 (2003), p. 499.

27. N. R. Michael, Ashfold, F. Claeyssens, M. Gareth. Fuge and J. Simon. Henley, Pulsed laser ablation and deposition of thin films, J Chem. Soc. Rev., 23 (2004), p.33.

28. S. Mao, S. Samuel S. Mao, Xianglei, G, Ralph; R. Richard, Initiation of an early-stage plasma during picosecond laser ablation of solids . Appl. Phys. Lett., 77 (2000), p. 2464.

29. J. Mazumder, O. Conde,R. Vilar,W. Steen, Laser processing : surface treatment and film deposition, Kluwer Academic (1996).

30. G.W. Yang, Laser ablation in liquids: Applications in the synthesis of nanocrystals, Progress in Mater. Sci., 52 (2007), p.648.

31. C. Oros, Investigations involving shock waves generation and shock pressure measurement in direct ablation regime and confined ablation regime, Shock Waves, 11 (2002), p. 393.

32. J. Ren, M. Kelly, and L. Hesselink, Laser ablation of silicon in water with nanosecond and femtosecond pulses, Opt. Lett., 30 (2005), p.1740.

33. L. Berthe, R. Fabbro, P. Peyre, L. Tollier, and E. Bartnicki , Shock waves from a water-confined laser-generated plasma, J. Appl. Phys., 82 (1997), p. 1063.

34. A. Kruusing, Underwater and water-assisted laser processing: Part 2—Etching, cutting and rarely used methods, Optics and Lasers in Engineering. 41 (2004), p. 329.

35. S. Zhu, Y. Lu, M. Hong, X. Chen., Laser ablation of solid substrates in water and ambient air, J Appl. Phys., 89 (2001), p. 2400.

36. A.V. Simakin, V.V. Voronov, G.A. Shfeev and R. Brayner, Nanodisks of Au and Ag produced by laser ablation in liquid environment, Chem. Phys. Lett., 384 (2001), p. 182.

37. S.I. Dolgaev, A.V. Simakin, V.V. Voronov, G.A. Shfeev and F. Bozon-Verduraz, Nanoparticles produced by laser ablation of solids in liquid environment, Appl. Surf. Sci., 186 (2002), p. 546.

38. G. Compagnini, A.A. Scalisi and O. Puglisi, production of gold nanoparticles by laser ablation in liquid alknes, J. of Appl. Phy., 94 (2003), p. 7874.

39. C. Liango, Y. Shimizu, M. Masuda. T. Sasaki and N. Koshizaki , preparation of layered zinc hydroxide/ surfactant nanocomposite by pulsed laser ablation in a liquid medium, Chem. Mater., 16 (2004), p. 963.

40. T. Sakka, S. Iwanaga, Y.H.Ogata, A. Matsunawa,T. Takemoto, Laser ablation at solid–liquid interfaces: An approach from optical emission spectra, J. Chem. Phys., 112 (2000), p. 8645.

41. C. Liang, T, Sasaki, Y, Shimizu and N, Koshizaki, pulsed laser ablation of Mg in liquids: surfactant directing nanoparticles assembly for magnesium hydroxide nanostructure, Chem. Phys. Lett., 389 (2004), p. 58.

42. C.H. Liang, Y.Shimizu, T. Sasaki and N.Koshizaki, preparation of ultrafine TiO2 nanocrystals Via pulsed laser ablation of titanium metal in surfactant solution, Appl. Phys. A, 80 (2005), p. 819.

43. T. Tsuji, T. Hamagami, T. Kawamura, J. Yamaki and M. Tsuji, laser ablation of cobalt and cobalt oxide in liquids: influence of solvent on prepared nanoparticles, Appl. Sur. Sci., 243 (2005), p214.

44. S.C. Singh, R. Gopal, Zinc nanoparticles in solution by laser ablation technique, Bull. Mater. Sci., 30 (2007) p. 291.

45. A. V. Kabashin and M. Meunier, Laser ablation-based synthesis of functionalized colloidal nanomaterials in biocompatible solutions, J. of Photochemistry and Photobiology A: Chemistry, 182 (2006), p.330.

46. J. H. Ryu, S.Y. Bang, J.W. Yoon, C. S. Lim and K. B. Shim, Pulsed laser induced synthesis of scheelite-type colloidal nanoparticles in liquid and the size distribution by nanoparticles tracking analysis, Appl. Surf. Sci., 15 (2007), p. 8408.

47. X. T. Phuoc, B. H. Howard, D. V. Martello, Y. Soong, M. K. Chyu, Synthesis of $Mg(OH)_2$, MgO, and Mg nanoparticles using laser ablation of magnesium in water and solvents, Optics and Lasers in Engineering 46 (2008), p. 829.

48. D. Poondi, T. Dobbins, J. Singh, A novel laser-liquid-solid interaction technique for synthesis of silver, nickel and immiscible silver-nickel alloys from liquid precursors, J. of Mater. Sci., 35 (2000), p. 6237.

49. H. Usui, Y. Shimizu, T. Sasaki and N. Koshizaki, photoluminescence of ZnO nanoparticles prepared by laser ablation in different surfactants, J. Phys. Chem. B, 109 (2005), p.120.

50. Y. Ishikawa, Y. Shimizu, T. Sasaki, N. Koshizaki, Preparation of zinc oxide nanorods using pulsed laser ablation in water media at high temperature, J. of Coll. and Inter. Sci., 300 (2006), p. 612.

51. R.K. Thareja, S. Shukla, Synthesis and characterization of zinc oxide nanoparticles by laser ablation of zinc in liquid, Appl. Sur. Sci., 253 (2007), p. 8889.

52. C. He, T. Sasaki, H. Usui, Y. Shimizu, and N. Koshizaki, Fabrication of ZnO nanoparticles by pulsed laser ablation in aqueous media and pH-dependent particle size: An approach to study the mechanism of enhanced green photoluminescence, J. of Photo chemistry and Photobi A: Chem., 191 (2007), p. 66.

53. C. He, T. S. Yoshiki and N. Koshizaki, Synthesis of ZnO nanoparticles using nanosecond pulsed laser ablation in aqueous media and their self-assembly towards spindle-like ZnO aggregates, Appl. Sur. Sci., 87 (2008), p. 2196.

54. S.C. Singh, R. Gopal, Synthesis of colloidal zinc oxide nanoparticles by pulsed laser ablation in aqueous media, Physica E., 40 (2008), p. 724.

55. B. D. Cullity and S. R. Stock, Elements of X-ray diffraction, 3'nd Edition Prentice-Hall, New York (2001).

56. B. E. Warren, X Ray Diffraction, Dover Publications, New York, (1990).

57. R. Kelsall , Ian W. Hamley, M. Geoghegan, Nanoscale Science and Technology, John Wiley & Sons Ltd, Uk (2005).

58. A. D L. Humphris, M. J. Miles, J. K. Hobbs, A mechanical microscope: High-speed atomic force microscopy, Appl. Phys. Lett., 86 (2005), p. 034106.

59. B. David. C. Williams and C. Barry, Transmission Electron Microscopy: A Textbook For Materials Science, Plenum Publishing Corporation, New York (1996).

60. M. D. Graef, Introduction to conventional transmission electron microscopy, Cambridge University presses (2003) UK.

61. Ü. Özgür,_ Y. I. Alivov, C. L, A. Teke, M. A. Reshchikov, S. Doğan_ V. Avrutin, S.-J. Cho, and H. Morkoç, A comprehensive review of ZnO materials and devices, J. Appl. Phys., 98 (2005), p. 041301

62. S.J. Pearton, D.P. Norton, K. Ip, Y.W. Heo and T. Steiner, Recent Progress in processing and properties of ZnO, Prog. Mater. Sci., 50 (2005), p.293.

63. B.J. Jin, S. Im, S.Y. Lee, Violet and UV luminescence emitted from ZnO thin films grown on sapphire by pulsed laser deposition, Thin Solid Films, 366 (2000), p.107.

64. K. Vanheusden, W. L. Warren, C. H. Seager, D. R. Tallant, J. A. Voigt, and B. E. Gnade, Mechanisms behind green photoluminescence in ZnO phosphor powders, J. Appl. Phys., 79 (1996), p. 7983.

65. M.N. Kamalasanan, S. Chandra, Sol–gel synthesis of ZnO thin films, Thin Solid Films, 288 (1996), p.112.

66. L. Spanhel, M.A. Anderson, Semiconductor clusters in the sol–gel process: quantized aggregation, gelation, J. Am. Chem. Soc., 113 (1991), p. 2826.

67. A. Dakhlaoui, M. Jendoubi , L. S. Smiri , A. Kanaev , N. Jouini, Synthesis, characterization and optical properties of ZnO nanoparticles with controlled size and morphology, Journal of Crystal Growth, 311 (2009), p.3989.

68. A.K. Chawla, D. Kaur, R. Chandra, Structural and optical characterization of ZnO prepared by sputtering, Opt. Mater., 29 (2007), p. 995.

69. D. Jezequel, J. Guenot, N. Jouini, N.F. Fievet, Submicrometer zinc oxide. . .polyol medium and morphological characteristics, J. Mater. Res., 10 (1995), p.77.

70. J. Chen, H. Deng, M. Wei, Hydrothermal synthesis and optical properties of ZnO single-crystal hexagonal microtubes, Mater. Sci. and Eng. B, 163 (2009), p. 157.

71. M. Izaki, T. Omi, Transparent zinc oxide films prepared by electrochemical reaction, Appl. Phys. Lett., 68 (1996), p.2439.

72. C. Suryanarayana, M.G. Norton, X-Ray Diffraction a Practical Approach, Plenum Press, New York, 1998.

73. S. K. Marathe, P. M. Koinkar, S. S. Ashtaputre, M. A. More, S. W. Gosavi, D. S. Joag and S. K. Kulkarni, Efficient field emission from chemically grown inexpensive ZnO nanoparticles of different morphologies, Nanotechnology, 17 (2006), p. 1932.

74. P.T. Hsieh, Y.C. Chen1, K.S. Kao, C.M. Wang, Luminescence mechanism of ZnO thin film investigated by XPS measurement, Appl. Phys. A, 90 (2008), p.317.

75. S. Karamat, C. Ke, T.L. Tan, W. Zhou, P. Lee, R.S. Rawat, Investigation of impurity phase formation for $(ZnO)_{1\_x}$ $(TMO)_x$ bulk samples formed by ball milling, Appli. Sur. Sci., 255 (2009), p.4814.

76. L.E. Brus, Electron–electron and electron–hole interactions in small semiconductor crystallites: the size dependence of the lowest excited electronic state, J. Chem. Phys., 80 (1984), p. 4403.

77. S.S. Kurbanov. G.N. Panin, T.W. Kim. T.W. Kang, Strong violet luminescence from ZnO nanocrystals grown by the low-temperature chemical solution deposition, J. of Lumi., 129 (2009), p.1099.

78. C. Liang, Y. Shimizu, M. Masuda, T. Sasaki, and N. Koshizaki, Preparation of layered zinc hydroxide/surfactant nanocomposite by pulsed laser ablation in a liquid medium, Chem. Mater., 16 (2004), p. 963.

79. H. Zeng, W. Cai, J. Hu, G. Duan, P. Liu, Violet photoluminescence from shell layer of Zn/ZnO core shell nanoparticles, Appl. Phys. Lett., 88 (2006), p.171910.

80. Q.P. Wang, D.H. Zhang, Z.Y. Xue, X.T. Hao, Violet luminescence emitted from ZnO films deposited on Si substrate by RF magnetron sputtering, Appl. Surf. Sci., 201 (2002), p.123.

81. U. Hiroyuki, The effect of surfactants on the morphology and optical properties of precipitated wurtzite ZnO, Mater. Lett., 63 (2009) 1489.

82. A. Degen, and M. Kosec, Influence of pH and Ionic impurities on the adsorption of poly(acrylic) dispersant onto a zinc oxide surface, J. Eur. Ceram. Soc., 20 (2000), p. 667.

83. X. Han, R. Liu, W. Chen, Z. Xu, Properties of nanocrystalline zinc oxide thin films prepared by thermal decomposition of electrodeposited zinc peroxide, Thin Solid Films, 516 (2008), p. 4025.

84. C.C. Hsu, N.L. Wu, J. Photocatalytic activity of ZnO/ZnO_2 composite, Photochem.and Photobiol. A: Chem., 172 (2005), p.269.

85. L. Ibarra, M. Alzorriz, Effect of temperature on the crosslink densities of nitrile rubber and carboxylated nitrile rubber with zinc peroxide, J. Appl. Polym. Sci., 86 (2002), p. 335.

86. M.A. Gondal, Q.A. Drmosh, Z.H. Yamani, T.A. Saleh, Synthesis of ZnO_2 nanoparticles by laser ablation in liquid and their annealing transformation into ZnO nanoparticles, Appl. Sur. Sci., 67 (2009) p.298.

87. W. Chen, Y. H. Lu, M. Wang, L. Kroner, H. Paul, H. J. Fecht, J. Bednarcik,| K. Stahl, Z. L. Zhang, U. Wiedwald, U. Kaiser, P. Ziemann, T. Kikegawa, C.

D. Wu, and J. Z. Jiang, Synthesis, Thermal Stability and Properties of ZnO2 Nanoparticles, J. Phys. Chem. C, 1320 (2009), p.113.

88. Y.C. Zhang, X. Wu, X.Y. Hu, R. Guo, Low temperature syntheses of nanocrystalline ZnO by thermal decomposition of a green single- source inorganic precursor in air, J. of cryst. grow., 280 (2005), p.250.

89. C. Cheng. N. Wu, synthesis photocatlytic activity of ZnO / ZnO_2 composite, J. Photochem. And Photobio. A: Chem., 172 (2005), p. 269.

90.   M. Sun, W. Hao, C. Wang, T. Wang, A simple and green approach for preparation of ZnO_2 and ZnO under sunlight irradiation, Chem. Phys. Lett., 443 (2007), p. 342.

91. M. Fukuhara, Lattice expansion of nanoscale compound particles, Phys. Lett. A, 313 (2003), p. 427.

92. H.K. Schmid, Quantitative Analysis of Polymorphic Mixes of Zirconia by X-Ray Diffraction, J. Am. Ceram. Soc., 70 (1987), p.367.

93. W. Qin ,Z. H. Chen, P. Y. Huang and Y. H. Zhuang, Crystal lattice expansion of nanocrystalline materials, J, of Alloys and Compounds, 292(1999), p.230.

94. M.A. Gondal, Q.A. Drmosh, Z.H. Yamani, M. Rashid, Synthesis of nanostructured ZnO and ZnO2 by laser ablation process using third harmonic of Nd:YAG laser, Int. J. Nanoparticles ,2 (2009), p.142.

95. Kwon, Yong Jae; Kyoung Hun Kim; Chang Sung Lim; and Kwang Bo Shim, Characterization of ZnO nanopowders synthesized by the polymerized complex

method via an organochemical route, J. of Ceramic Processing Research, 3 (2002), p.146.

96. A. Imre, D.L. Beke, E. Gontier-Moya, I.A. Szab'o, E. Gillet, Surface Ostwald ripening of Pd nanoparticles on the MgO (1 0 0) surface, Appl. Phys. A, 71 (2000), p.19.

97. F. Fillot, Z. TO¨ kei, G.P. Beyer, Surface diffusion of copper on tantalum substrates by Ostwald ripening, Surf. Sci., 601 (2007), p. 986.

98. P. Singh, A. Kumar, D. Deepak, Kaur, ZnO nanocrystalline powder synthesized by ultrasonic mist-chemical vapour deposition, Opt. Mater., 30 (2008), p.1316.

99. O.N. Senkov, B.C. Chakoumakos, J.J. Jonas, F.H. Froes, Effect of temperature and hydrogen concentration on the lattice parameter of beta titanium, Mater. Res. Bull., 36 (2001), p. 1431.

100. J. Zhou, Y. Wang, F. Zhao, Y. Wang, Y. Zhang, L. Yang, Photoluminescence of ZnO nanoparticles prepared by a novel gel-template combustion process, J. Luminescence, 119 (2006), p. 248.

101. K. Vanheusdena, C.H. Seagera, W.L. Warrena, D.R. Tallanta, J. Carusob, M.J. Hampden-Smithb, T.T. Kodasb, Green photoluminescence efficiency and free carrier density in ZnO phosphor powders prepared by spray pyrolysis, J. Luminescence, 75 (1997), p.11.

102. M. Balkansk, R.F. Wallis, Semiconductor Physics and Applications, Oxford University Press Inc., New York, 2000.

103. K.F. Lin, H. Cheng, H. Hsu, L. Lin, W. Hsieh, Band gap variation of size-controlled ZnO quantum dots synthesized by sol–gel method, Chem. Phys. Lett., 409 (2005), p.208.

104. T. Waitz, M. Tiemann, P.J. Klar, J. Sann, J. Stehr, B.K. Meyer, Crystalline ZnO with an enhanced surface area obtained by nanocasting, Appl. Phys. Lett., 90 (2007), p.123108.

105. D.M. Fernandes, R. Silva, A.A. Winkler Hechenleitner, E. Radovanovic, M.A. Custo dio Melo, E.A. Go´mez Pineda, Synthesis and characterization of ZnO, CuO and a mixed Zn and Cu oxide, Mater. Chem. Phys.,115 (2009), p.110.

106. A. Diéguez, A. Romano-Rodríguez, J. R. Morante, U. Weimar, M. Schweizer-Berberich and W. Göpel, Morphological analysis of nanocrystalline SnO2 for gas sensor applications, Sensors and Actuators B: Chemical, 31 (1996), p. 176.

107. N. Kudo, Y. Shimazaki, H. Ohkita, M. Ohoka, S. Ito, Organic–inorganic hybrid solar cells based on conducting polymer and SnO_2 nanoparticles chemically modified with a fullerene derivative Solar Energy Materials and Solar Cells, 91 (2007), p. 1243.

108. C. Choudhury, H.K. Sehgal , Chemical vapour deposited SnO2:Sb heat mirror coatings for cylindrical solar collectors, Energy Conversion and Management, 29 (1989), p. 265.

109. M. Ruske, G. BraÈuer, J. Pistner, U. PfaÈf¯in, J. Szczyrbowski, Properties of SnO2 ®lms prepared by DC and MF reactive sputtering, Thin Solid Films, 351 (1999) p.146.

110. Y. Ning, W. Jianhua, G. Yuzhong, Z. Xiaolong, SnO$_2$ Nanofibers prepared by sol-gel template method, Appl. Sci. Sic., 69 (2008), p. 0694.

111. J. Ahmed, S. Vaidya, T. Ahmad, P. S. Devi, D. Das, A. K. Ganguli, Tin dioxide nanoparticles: Reverse micellar synthesis and gas sensing properties, Mater. Res. Bull, 43 (2008), p. 264.

112. S.H. Luo, Q. Wan, W.L. Liu, M. Zhang, Z.T. Song, C.L. Lin, Paul K. Chu, Photoluminescence properties of SnO$_2$ nanowhiskers grown by thermal evaporation, Progress in Sol. Stat. Chem., 33 (2005), p.287.

113. J. Pal, P. Chauhan, Structural and optical characterization of tin dioxide nanoparticles prepared by a surfactant mediated method, Mater. Charact. (in press).

114. S. Emiroglu, N. Bârsan, U. Weimar and V. Hoffmann, In situ diffuse reflectance infrared spectroscopy study of CO adsorption on SnO2 , Thin Solid Films, 391 (2001), p. 176.

115. P. Shah, A.V. Ramaswamy, K. Lazar, V. Ramaswamy, Synthesis and characterization of tin oxide-modified mesoporous SBA-15 molecular sieves and catalytic activity in trans-esterification reaction, Appl. Catal. A: General, 273 (2004), p.239.

116. T.W. Kim, D.U. Lee, Y.S. Yoon, J. Appl. Phys., 88 (2000), p. 3759.

117. J.Q. Hu, Y. Bando, D. Golberg,, Self-catalyst growth and optical properties of novel SnO$_2$ fishbone-like nanoribbons, Chem. Phys. Lett., 372 (2003), p. 758.

118. F. Gu, S. F. Wang, M. K. Lu, X. F. Cheng, S. W. Liu, G. J. Zhou, D. Xu, D. R. Yuan, Luminescence of SnO_2 thin films prepared by spin-coating method, J. of Crystal Growth, 262 (2004), p. 182.

119. Y. Hera and J. Wu, Low-temperature growth and blue luminescence of SnO_2 nanoblades, Appl. Phys. Lett., 89 (2006), p. 043115.

VITA

Full Name: Qasem Ahmed Qasem Drmosh.

Place & date of Birth: Ibb- Yemen: 19-4-1978.

Nationality: Yemen.

Present address: King Fahd University of Petroleum & Minerals P.O. Box: 8533, Dhahran 31261, Saudi Arabia.

Permanent address: Taiz city , Ibb, Yemen.

Email: k_dormosh@yahoo.com.

PUBLICATIONS AND CONFERENCES

1- M.A. Gondal. **Q.A. Drmosh**, Z. H. Yamani and M. Rashid, Synthesis of Nanostructure ZnO and ZnO_2 by Laser Ablation Process Using Third Harmonic of Nd:YAG Laser, *International Journal of nano particles 2* (2009) 142–149.

2- M.A, Gondal. **Q.A. Drmosh** and Z. H. Yamani, Synthesis of ZnO_2 nanoparticles by laser ablation in liquid and their annealing transformation into ZnO nanoparticles, *Applied Surface Science* 256 (2009) 298–304.

3- **Q.A. Drmosh**. M.A. Gondal. T.A. Saleh, Spectroscopic characterization approach to study surfactants effect on ZnO2 nanoparticles synthesis by laser ablation process, *Applied Surface Science* (2010).

4- **Q.A. Drmosh**, M.A. Gondal, T.A. Saleh, Synthesis of SnO$_2$ Nanoparticles Using High Power Pulsed Laser Ablation Technique (submit).

5- M.A. Gondal, **Q.A. Drmosh**, Z. H. Yamani, T. A. Saleh, The effect of the post-annealing temperature on the nano-structure and optical properties of ZnO nanoparticles synthesized from ZnO$_2$ prepared by Laser Ablation Method, *International Journal of nano particles* (accepted and in press).

6- M.A. Gondal, **Q.A. Drmosh**, Z.H. Yamani, T.A. Saleh , Laser ablation for ZnO$_2$ nanoparticles Synthesis and their application for cyanide determination (in progress).

7- M.A. Gondal, Z.H. Yamani ,**Q.A. Drmosh** and M. Rashid , Synthesis of Nanostructured ZnO and ZnO$_2$ by Laser Ablation Process Using Third Harmonic of Nd:YAG Laser, *International Conference on Nanotechnology (ICON008), Jeddah, Saudi Arabia* (17-19 June, 2008).

8- M.A. Gondal. **Q.A. Drmosh**, Z.H. Yamani, Study of Surfactants and Post Annealing Temperature On Size of Synthesized Nano Structure ZnO Using High Power Pulsed Laser Ablation Technique, *The International Conference For Nanotechnology Industries The Leading Technology of 21st Century Riyadh, Saudi Arabia*, (5-7 April, 2009).

9- M.A. Gondal. **Q.A. Drmosh**, Z.H. Yamani, Surfactants Effect On The Morphology Of Nanoparticles Synthesized By Novel Laser Ablation Method at 355 nm, *International Conference of Nanotechnology and Advanced Materials (ICNAM), Bahrain, (*4-7 May, 2009).

10- **Q.A. Drmosh,** M.A. Gondal , T.A. Saleh and Z. H. Yamani, synthesis and characterization of ZnO_2 nanoparticles using optical techaniques, *fourth Saudi conference, Tibah University, Saudi Arabia*, (21-24 March, 2010).